Fracture Induced CNT-paper Composites for Wearable Sensors

Jinyuan Zhang

A dissertation
submitted in partial fulfillment of the
requirements for the degree of

Doctor of Philosophy

University of Washington

2019

Reading Committee:
Jae-Hyun Chung, Co-Chair
Dayong Gao, Co-Chair
Jinkyu Yang, Member
Anthony Dichiara, GSR

Program Authorized to Offer Degree:
Mechanical Engineering

University of Washington

Abstract

Fracture Induced CNT-paper Composites for Wearable Sensors

Jinyuan Zhang

Co-Chairs of the Supervisory Committee:
Associate Professor Jae-Hyun Chung
Professor Dayong Gao
Department of Mechanical Engineering

Wearable sensors have been widely applied in the fields of human-machine interface, medical care, and disease diagnosis. Various types of wearable sensors with different materials and fabrication methods have been developed. However, high fabrication cost, low sensitivity and large form factors have hampered their popularity of wearable applications. Paper-based sensors have shown merits of simple fabrication, high sensitivity and light weight. Biomedical, chemical, and physical wearable sensors have been developed by using paper substrate. In this dissertation, a novel manufacturing method of carbon nanotube (CNT)-paper composite is studied with characterization of mechanical and electrical properties. A fracture-induced fabrication method of a CNT-paper composite (CPC) is studied in terms of reorganization of a CNT-cellulose fiber

matrix. By precise control of the applied strain, resistive and capacitive sensors are produced to enable the measurement of heart beats, grabbing force, finger motion, and eye movement.

Using a CPC, a humidity sensor is developed for wearable applications. The enhancement of sensor response due to swelling of CPC coated with polyacrylic acid (PAA) is studied for detection of water vapors in air. The humidity sensor is applied for measurement of surface moisture. The CPC sensor provides a low-cost, highly sensitive, light-weight flexible platform potentially beneficial for sweat monitoring.

An unobtrusive light-weight, low-cost eye tracking sensor is developed by using a capacitive sensor made of a fractured CPC. The eye movement is measured by the capacitance changes induced by the distance and permittivity change between eye ball, muscles and CPC sensors. The fabrication procedures and sensor design are optimized for best sensing performance. Finite element analysis is applied to understand the capacitive sensor made of the fracture induced nanoscale electrodes. The sensitivity and resolutions are characterized in terms of the capacitive geometry.

In summary, the dissertation presents the characteristics of fractured CPC and the applications to multiple wearable sensors. A CPC coated with PAA is investigated for detection of relative humidity and moisture. The low cost, high sensitivity, light weight and easy fabrication will offer a stepping stone to advance current wearable sensing platforms.

Table of Contents

List of Figures

List of Tables

Acknowledgements

Firstly, I would like to express my sincere gratitude to my co-advisors Prof. Jae-Hyun Chung and Prof. Dayong Gao for the continuous support of my PhD study and related research, for their patience, motivation, and immense knowledge. Their guidance helped me in all the time of my PhD program. I could not have imagined having a better advisor and mentor for my PhD study.

Besides my advisors, I would like to thank the rest of my thesis committee: Prof. Jinkyu Yang and Prof. Anthony Dichiara, for their insightful comments and encouragement, but also for the hard question which incented me to widen my research from various perspectives.

I would also like to express sincere appreciation to China Scholarship Council, for supporting my research and living expenses. The research was partially supported by the CoMotion Innovation Fund at University of Washington.

Last but not the least, I would like to thank my family: my parents and my sister for supporting me spiritually throughout my PhD study and my life in general.

Chapter 1. Introduction

This research investigates the mechano-electrical characterization of a carbon nanotube (CNT)-paper composite and application to wearable sensors. In this chapter, the advances of wearable sensors are introduced in various fields. Then, the recent development of paper-based sensors is discussed. Lastly, CNT-paper composite sensors and their applications are described.

1.1 Wearable sensors

The development of wearable sensors has flourished over the past decade in the areas of medical treatment and rehabilitation [2, 3], robotics [4], entertainment [5, 6], etc. Examples of those innovative sensors include strain sensors, pressure sensors, electronic skins, temperature sensors, sweat sensors and heart rate sensors[1] [7] [8] [9]. The nature that those sensors can attach to or being worn by human in daily life ensures more accurate measurement of the required data and more sustainable monitoring. Figure 1.1 shows an example of a wearable sensor that is attached on various locations of a human body [1]. By detecting the strain changes resulted from different human activities, the body response was recognized. In this chapter, the application of the wearable sensors is introduced with emphasis on the fields of healthcare and human-computer interface.

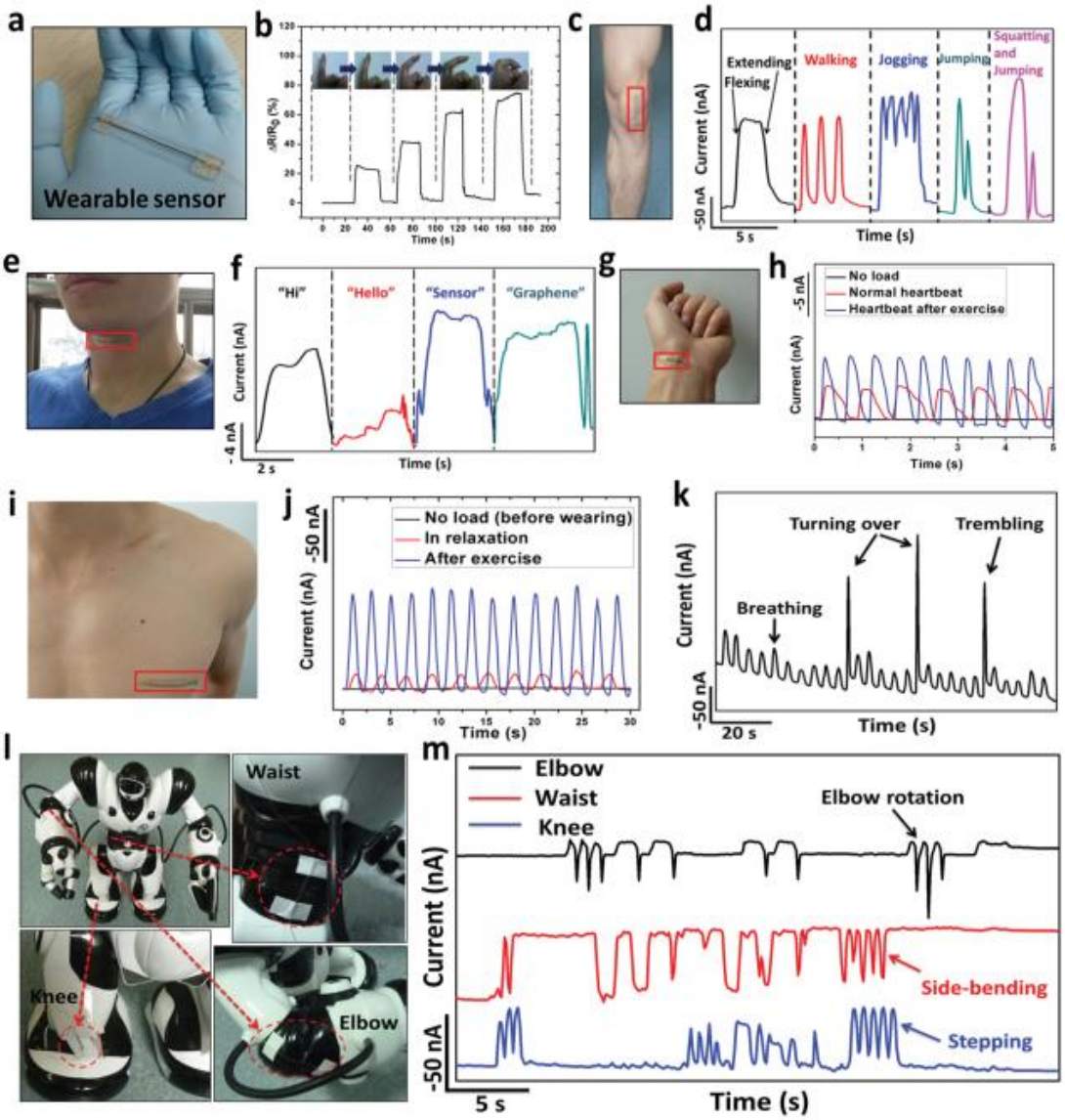

Figure 1.1 Applications of wearable sensors to monitor the body activities of human and robot. (a) Photograph of the wearable sensor. (b) Response signal of wearable sensor in monitoring finger bending. Inset: Photographs of finger-bending to the corresponding positions. (c) Wearable sensor attached to the knee, marked in the red box. (d) Responsive curves of wearable sensor on the knee under motions of flexing/extending, walking, jogging, jumping, and squatting-jumping. (e) Wearable sensor attached to the throat, marked in the red box. (f) Responsive curves when wearer spoke “Hi”, “Hello”, “Sensor”, and “Graphene”. (g) Wearable sensor attached to the wrist, marked in the red box. (h) Responsive curves of wearable sensor on the wrist before wearing (no load), and under normal/exercise conditions. (i) Wearable sensor attached to the chest. (j) Responsive curves of wearable sensor on the chest before wearing, in relaxation, and after exercise. (k) Responsive curves of wearable sensor on the chest. The wearer simulates deep sleep (keeping still) and light sleep (turning over and trembling frequently). (l) The robot wears fiber sensors at movable joints (elbow, waist, and knee). Each sensor is marked in the red box at specific joint position. m) Responsive curves of wearable sensors during the robot's dance “Gangnam Style”: elbow (black line), waist (red line), and knee (blue line) [1].

1.1.1 Wearable sensors in medical field

The key features of wearable sensors are light weight and flexibility such that the sensors could be worn on the body to perform standard medical monitoring. Critical medical information such as body temperature, heart rate, brain activity, muscle can be easily detected by wearable sensors [10, 11]. To continuously monitor critical medical information, wearable sensors offer an easier "all-day" monitoring method. Similar requirement is exerted in the area of sport and training where physiological information, such as sweat level change, needs to be recorded by wearable sensors [12, 13]. Different medical information requires the development of various wearable sensors. The detected data will be stored or transported for further medical analysis. Based on the wearable sensor technology, a big step in medical care is: traditional diagnosis of certain disease and the monitoring of a patient's activity needs to be simplified by a low cost wearable sensor.

One of the most important advantages is the light weight and small form factor of the wearable sensors in comparison to traditional medical instruments. The measurement of blood pressure, for example, that has been measured by sizable inflatable pressure cuff [14] can be replaced by earphone and mobile devices [15]. Such improvement not only makes the measurement easier, but also provides the possibility of treatment at home for self-diagnosis [16]. Similar devices include smart watches that can monitor the heart rates [7], a stretchable temperature sensor that can attach to human body [8], wearable/disposable sweat monitoring sensor that can monitor the glucose level [9], etc.

Daily monitoring for chronic disease diagnosis and prevention is one of the most promising potential application of the wearable sensors in a medical field [17]. Chronic diseases are leading causes of death and disability in both developed and developing

countries [18]. Inactivity is oriented from several chronic diseases [19]. The symptom of certain inactivity such as freezing of gait and falling should be monitored daily to prevent the chronic diseases. Fall detection, together with the gait monitoring by wearable sensors can be utilized for the detection of certain disease [20]. The diagnosis of Parkinson can also be easily conducted at an early stage with the help of the wearable sensors [21]. Based on the data collected by the wearable sensors, a doctor can foresee the potentials of many chronic diseases. Therefore, the timely preventive treatment can be taken to prevent the patient from further severe pains.

1.1.2 Wearable sensors in human-machine interface field

As the computer and other smart devices are playing more important roles in society, the efficient interaction between human and those devices becomes critical. There has been growing interest in development of revolutionary approaches and technologies for bridging the human-computer communication [22]. Many attempts have been made for hand gesture interaction and eye-based interaction. For the popular interaction approaches, different technologies involving wearable sensors are being developed. The eye-based wearable sensor interaction detects the gaze direction by certain electrical signal change, such as electro-oculography (EOG) signals [23]. The light weighted EOG wearable sensor has already been studied for the control of wheel chair for physically disabled people [24]. The audio system with wearable sensors control is developed, which has a potential of being applied on other electronic devices [25]. There is growing interest of the wearable sensors in entertainment field, such as video game controller. The traditional control approaches no longer satisfy the needs of the costumer. Controlling with wearable sensors provides

more actual and exciting experience. The products of Microsoft and Sony have the access to be connected to the wearable sensors.

As robotics field is expanding from the monotonous environment of a production line to complex human environments, robots are required to perform human-like motion and tasks instead of industrial use [4]. At the same time, more and more sophisticated activities should be accomplished by robots. Therefore, a more precise robot control method is required. Effort has been made to develop a new generation of interaction between the robot and human, such as the gesture recognition with glove-based sensor [26]. Similar wearable bio-sleeve is developed for the hand-free gesture control of robots (Figure 1.2) [27]. Although the recognition of most hand gestures is still under development, the promising future in this field is obvious.

Figure 1.2 Wearable bio-sleeve for hand-free gesture control of robots [28].

1.1.3 Challenges

As wearable sensor technologies branches into different sensing mechanism and sensor materials, the common requirement is: small size, flexibility, sensitivity, bio-compatibility and low cost.

One of the challenges for wearable sensors is data accuracy. The device reflected by the wearable sensor can make mistakes in certain cases, which results in imprecise data of a wearer. For example, the pedometer based energy expenditure algorithm was developed to estimate one's daily activity level[29]. But this wearable sensor is not able to detect the intensity of the movement, nor certain movement like climbing the stairs. The walking speed of a wearer can also be the origin of false data. This example shows that the wearable sensors can sometimes be inaccurate to show all the detailed activity. There are many reasons that can cause this kind of inaccurate detection and thus, misleading information. The data processing algorithm, the sensors' low sensitivities, the hysteresis of the sensor, improper position of the sensor that is worn or environmental change can be the potential factors that will affect the detection result of a wearable sensor. To solve this problem, new sensing materials and fabrication methods, as well as the ergonomic design of wearable sensors need to be further improved.

Another issue of wearable sensors is high cost, which is also the key factor that hampers the commercialization of wearable sensors. Because of the small form factor and high sensitivity, sensor fabrication is usually expensive. New sensing materials and scalable fabrication methods of wearable sensors at a low cost is critical to meet the demand of advanced wearable sensors.

1.2 Paper based sensor

1.2.1 Properties of paper

It has been of significant interest in the development of paper sensing platform in the last decade. In comparison to microfabrication technology based on silicon materials, cellulose based paper is flexible, thin and soft. The large surface area and porous structure composed of cellulose fibers are particularly useful for chemical/bio sensors. The biocompatible nature with the compostable characteristics is regarded as significant advantage for wearable sensors. The advantages of this simple cellulosic substrate is summarized in Table 1.1 [30]. Paper material is compared with other materials in Table 1.2 [30].

Table 1.1 Properties of paper [30].

	Property	Impact
Mechanical properties	Flexibility	Formation of complex 3D structures that will not tear when bent
	Thickness	Thickness of tens or hundreds of micrometers results in low (microliter) total volume required for device preparation
	Soft texture	Good contact with the solid objects, collection of traces of analytes by swabbing
Fibrous and porous structure	Absorbency	Storage and delivery of an exact volume of reagents inside the paper matrix [31], which frees the final users from handling chemicals; enrichment of the sample via multiple addition/ drying steps [32]; as the combined area of the channels is defined, there is no need for a constant sample volume
	Air permeability	Free diffusion of gas throughout the material [33] removes problems usually

		associated with microfluidic systems—air bubbles [31]
	Network structure	Filtration of the sample, e.g., contaminated with solids, separation of analytes by means of chromatography [34]
	High surface-to-volume ratio	Increase in the number of enzyme molecules or colorimetric probes that can be immobilized
	Capillary action	Ability to wick fluids dispenses with the use of pumps and permits fluid flow in all directions [33]
Natural origin	Compatible with biological samples, easy to sterilize [33], chemically and biologically inert, shows chirality, which is advantageous in immobilization of antibodies and proteins [31]	Can increase thermal stability of immobilized molecules, including enzymes [35] and gold nanoparticles [36]
	Disposability and biodegradability	Recyclable, rapidly degraded by microorganisms (~50 days) [37], and easily disposed of by incineration, eliminating the problem of contamination with biological material [38]

Table 1.2 Comparison of paper with traditional materials as substrates [30].

Property	Material			
	Glass	Silicon	PDMS	Paper
Surface profile	Very low	Very low	Very low	Moderate
Flexibility	No	No	Yes	Yes
Structure	Solid	Solid	Solid, gas-permeable	Fibrous
Surface-to-volume ration	Low	Low	Low	High
Fluid flow	Forced	Forced	Forced	Capillary action
Sensitivity to moisture	No	No	No	Yes
Biocompatibility	Yes	Yes	Yes	Yes
Disposability	No	No	No	Yes
Biodegradability	No	No	To some extent	Yes
High-throughput fabrication	Yes	Yes	No	Yes

Functionalization	Difficult	Moderate	Difficult	Easy
Spatial resolution	High	Very high	High	Low to moderate
Homogeneity of the material	Yes	Yes	Yes	No
Price	Moderate	High	Moderate	Low
Initial investment	Moderate	High	Moderate	Low

Furthermore, paper price is 200 times less than polyethylene terephthalate and 1000 times lower than glass [39, 40]. The low cost of the paper provides a promising future as a substrate in sensor fabrications. Also, the relatively small investment in paper-based sensing platform makes the application of a paper-based sensor spread widely worldwide, even in developing countries lacking access to scientific laboratory facilities [41]. Paper manufacturing usually does not require tedious pre-treatment and is user friendly [42].

1.2.2 Fabrication of paper based sensors

The fabrication of paper based sensors relies on the following techniques: cutting, printing, drawing, dip-coating, plotting and photolithography [30]. Sophisticated microfabrication methods can be combined with micro- and nanofabrication methods, such as, electron beam evaporation [31], thermal evaporation [25], sputtering [30], laser annealing [32], electroplating [33], and photolithography [43]. The remaining challenges of fabrication methods are related to paper processing. For example, an air-solid phase boundary at the cutting paper surface needs to be handled for paper trimming [44]. When polymers need to be coated on the paper surface, hydrophobic wall created by modification of fibers decreases the yield. Because of the large roughness, poor chemical and mechanical interfacial properties, many of the paper electronics use certain plastic film to achieve molecularly smoother interfaces to fabricate electronic devices such as organic diodes or

transistors [45]. However, the porous and rough condition of the paper material can be an ideal substrate as sensor substrate. The large surface area and porous structure of the paper is advantageous when paper-based nanocomposite, such as CNT-paper nanocomposite is fabricated. Figure 1.3 shows the nanostructure of paper and CNT-coated paper [46]. It is clear that the CNT network forms between the pristine cellulose fiber networks. The conductivity of the composite is determined by the interface of CNTs. Owing to the deformable structures in sensing, the cellulose structure can be very critical in certain detections [46].

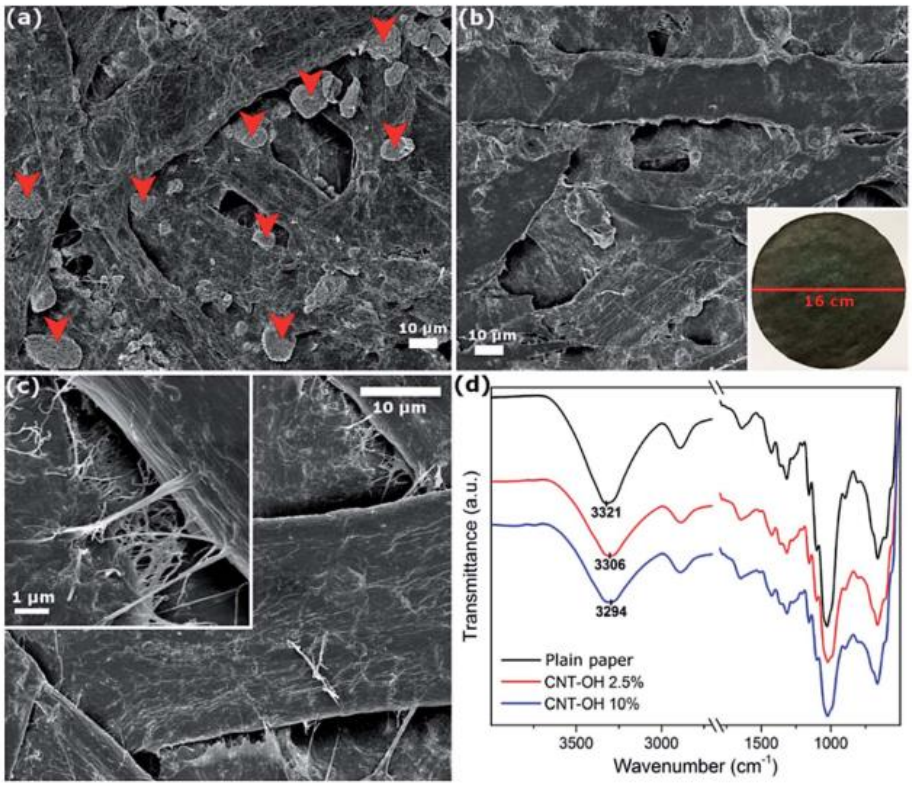

Figure 1.3 Representative SEM images of Kraft softwood papers reinforced with (a) pristine CNTs and (b and c) CNT-OH at 10 wt% loading. The photograph of a typical CNT–cellulose composite paper handsheet is shown in the inset in (b). (d) FTIR spectra of CNT–cellulose composite papers with different CNT contents. For clarity, a featureless region is omitted in the range 2700–1800 cm−1 [46].

Fabrication of CNT-paper composite sensors has been widely studied. Two fabrication methods are used to manufacture a composite sensor: 1. CNT-pulp mixture method 2. direct deposition of aqueous CNT onto the cellulose fiber. Detailed discussion will be given in the section 1.3 Paper based nanocomposite.

Nanostructured composites built on microporous cellulose fibers have potential impact in the fields of energy storage, biosensors, and flexible electronics. The main advantage of such composites is the combination of the multi-functional nanomaterials with low-cost cellulose fibers. The major motivation of the nanostructured composite based on cellulose fibers is the combination of light-weight and inexpensive cellulose fibers with multifunctional nanomaterials. Cellulose fibers extracted from wood pulp are a ubiquitous material to make paper. The large surface area of the cellulose fibers offers various advantages in energy, sensing and electronic applications [47, 48]. In particular, the porous and hydrophilic nature of cellulose fibers facilitates adhesion to various nanomaterials. With these nanomaterials, the surface properties of the cellulose fibers can be easily modified to obtain specific functionality.

Paper based biosensors are developed after the immobilization of molecules such as enzymes, antibodies and nanoparticles on papers [49]. Figure 1.4 shows three examples of immobilization technologies onto the cellulose fibers. The manufactured sensor is also called bioactive paper [50]. The challenge in paper-based biosensors is the immobilization methods. In order to obtain retention of long-term activity, protection of biomolecules immobilized on cellulose fibers is needed. There are mainly four methods for biomolecules immobilization on paper; physical immobilization, covalent and affinity-based attachment, immobilization on carriers and encapsulation [50].

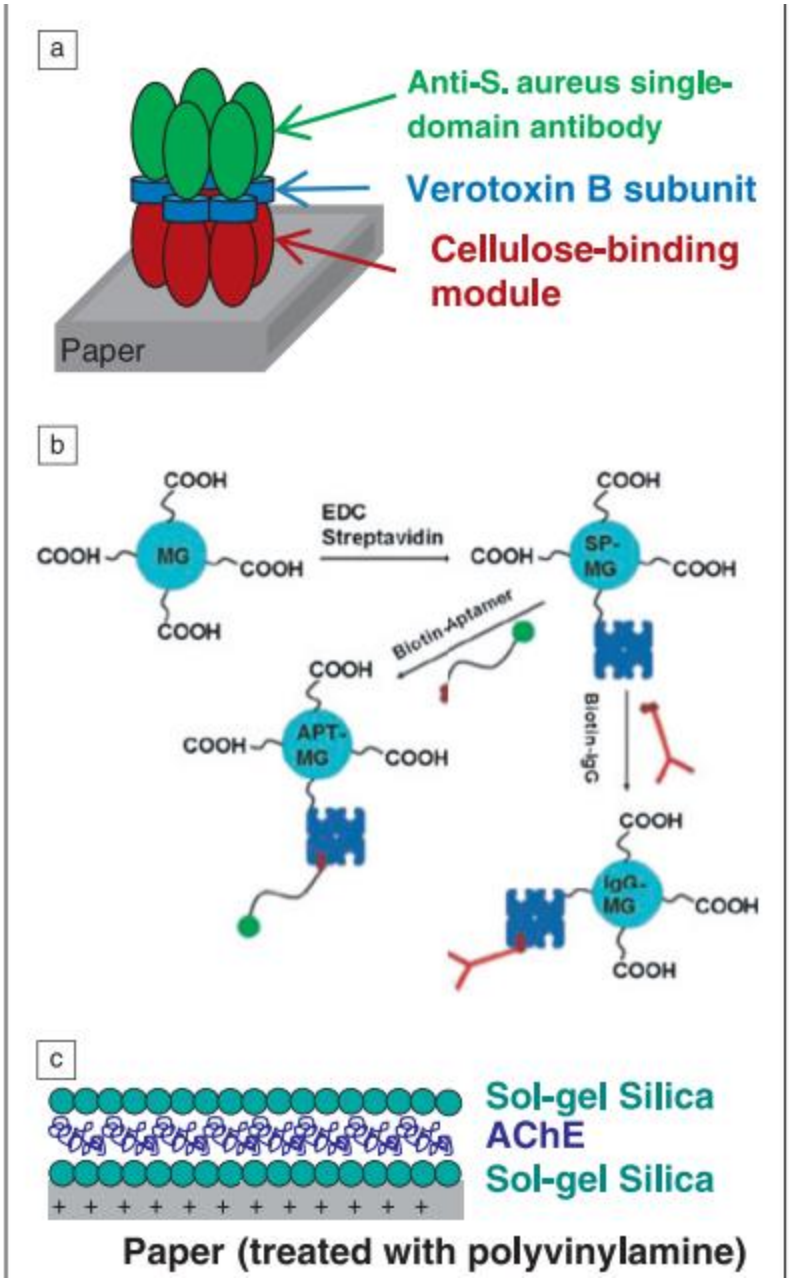

Figure 1.4 (a) Schematic representation of a bispecific pentamer. (b) Schematic representation of DNA aptamers or antibodies coupling on carboxylated microgels. (c) Schematic representation of AChE immobilized onto paper between two sol-gel silica layers [50].

In the paper-based sensor development process, fabrication is not a major challenge, but the sensor design is a hurdle for many applications[51]. The integration of a soft and fragile paper based sensor into a sensing circuit can be a critical issue. This issue becomes even more essential when a paper based physical sensor is fabricated. During the sensing

of an external pressure or strain, the sensor's structure must not be deformed or damaged to exceed an acceptable extent, such that the function of a sensor can't be affected. It is almost inevitable that all the physical paper-based sensors must limit the sensing capability to a relatively small range to avoid the sensor fracture [52, 53]. Addition of the intermediate polymers, such as PDMS, has been attempted to improve the strength of a paper based sensor [54, 55] . Another issue of the paper based sensor is that, the fabrication cost of a paper based sensor is high in comparison to the low cost of paper material. The complicated fabrication procedure is a major hurdle for low-cost paper sensors, which is one of the challenges for commercial applications. A new fabrication method is required in order to lower the manufacturing cost, as well as the total development expenditure.

1.2.3 Paper based sensing

Paper based sensors can be categorized into chemical sensing, biosensing and physical sensing in the contexts of targets or target parameters. Most research has been conducted in bio/chemical sensors because the large surface area offers tremendous opportunities for target and probe bindings. The detection of physical parameters such as strain, pressure, is relatively few because of the fragile and non-elastic nature of a paper based sensor. In addition, a creep effect among cellulose fibers can affect the offset shift, which needs to be resolved for stable physical sensors. In this section, previous development of bio/chemical/physical sensors will be discussed with the current challenges.

Various applications of paper in chemical sensing has been demonstrated. Most sensors are applied to biomedical and environmental studies. Nanomaterials, such as CNTs, metallic nanomaterials, silica nanoparticles are infiltrated into a cellulose fiber matrix for chemical sensors. When gold nanoparticles were embedded into cellulose fibers, mercury

ions could be detected in water [56]. A more straightforward method of fabricating the paper based sensor was to print electrodes on paper substrate [57]. Using the low cost fabrication method, multiple electrodes could be fabricated on single paper substrate for detection of selective chemicals. In comparison to other traditional chemical sensors, paper-based sensors were cheaper, disposable and portable [42].

Paper is an attractive material in biosensing area, because of (1) low fabrication cost, (2) capillary-based transport of liquid without external power sources, and (3) porous biocompatible cellulosic fiber networks for binding target- and probe molecules [50]. Figure 1.5 shows a biosensor using enzyme immobilized in 2-D scaffold of paper. Lateral flow assays and emerging paper microfluidics are a representative paper-based biosensor. For example, a lateral-flow immunoassay sensing platform with graphene oxide paper-based sensor is applied for pathogen detection [58]. A paper-based sensor immobilized with biomolecules is widely used in a bio-sensing field, especially in point-of-care diagnostics and on-site environmental monitoring. A paper-based microfluidic photoelectrochemical sensor was used to detect the pentachlorophenol for public health and environmental monitoring[59]. Compared with traditional biosensors, such a paper-based analytical device (μPAD) did not necessarily require a microfabrication including lithography [60], which significantly lowered the fabrication cost.

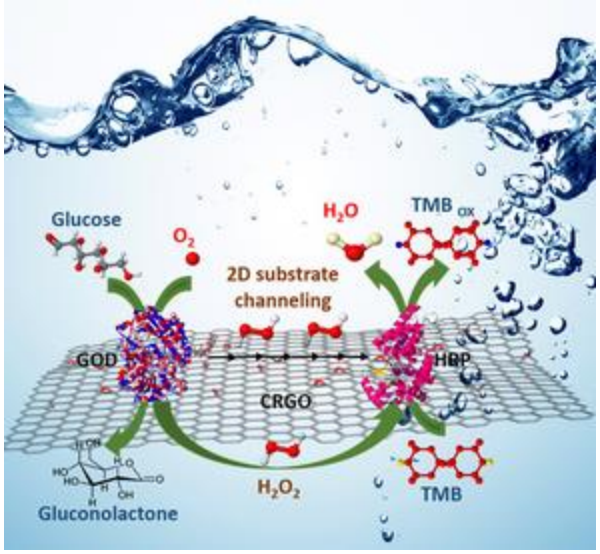

Figure 1.5 Enzyme immobilized paper as biosensor [61].

To fabricate a paper based physical sensor, such as strain sensor and piezo-resistive sensors, paper substrate needs to be improved to maintain the complete sensor structure. Otherwise, the sensing range is very limited. A highly stretchable piezo-resistive paper sensor has been developed using graphene-nanocellulsoe nanopaper. In this case, the pristine cellulose network structure is restructured, with graphene and PDMS, into a more crumple structure with higher density (Figure 1.6) [55]. Such a sensor can afford a strain of 100%. For those paper based sensor whose substrate has not been treated, this value is lower than 1% [62]. Ironically, the sensor that can detect larger strain change tends to have a lower sensitivity, while the sensor working in limited strain has relatively significant sensitivities. The former and latter sensors mentioned above have gauge factors of 3 and 536.6, respectively. The main reason is that, more stretchable structure contains a dense and better contacted junctions between the conductive nanomaterials (graphene in the above case) embedded among the cellulose fibers. The electrical response of the whole composite is caused by the disconnection and reconnection of the conductive nanomaterials.

Under the strain, the proportions of disconnected junctions are smaller in the high stretchability composite, even under high applied strain. In the pristine cellulose network, the attached conductive nanomaterials tend to have intense contact condition change and result in a large change in the conductivity of the sensor.

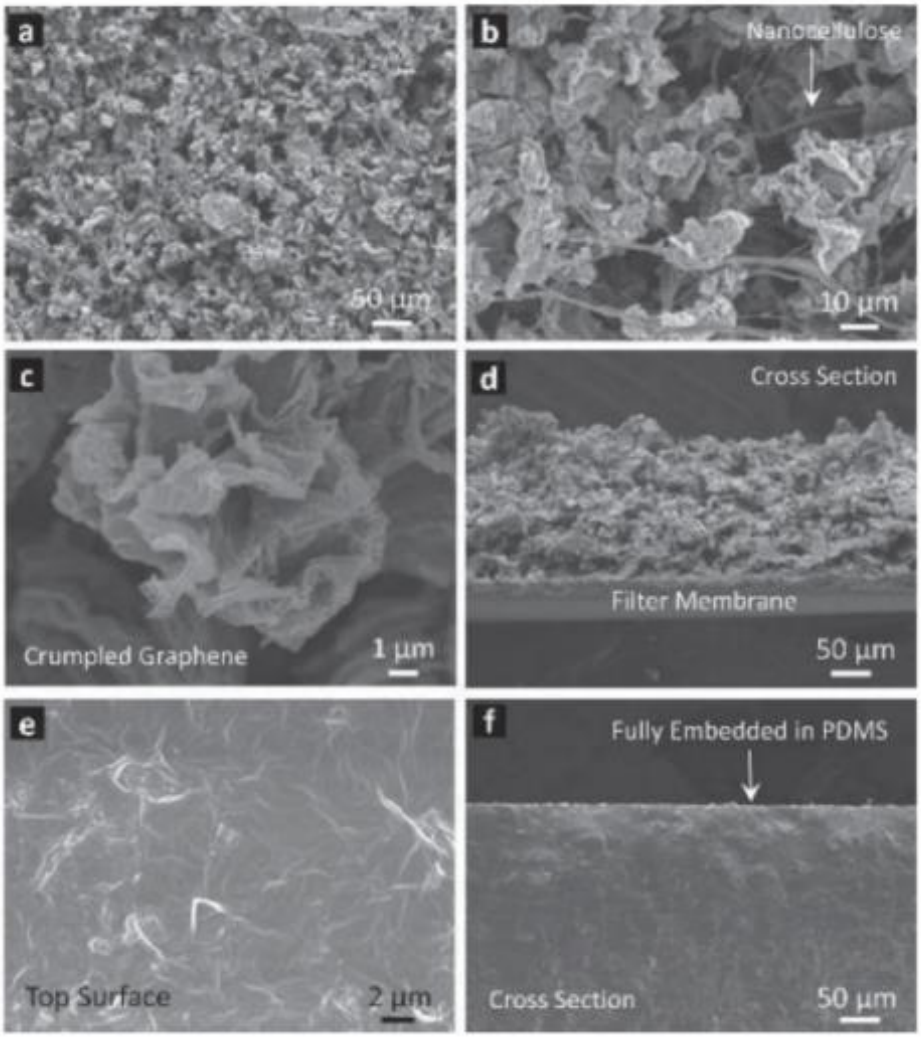

Figure 1.6 Structural characterizations of the flexible and stretchable nanopapers. (a–c) Top view SEM images of flexible nanopaper showing the macroporous structure based on crumpled graphene and nanocellulose. (d) Cross-sectional view showing that the flexible nanopaper is porous throughout the entire thickness. (e, f) Top view and cross-sectional view of the stretchable nanopaper with fully embedded structure [55].

1.3 CNT paper composite

1.3.1 Fabrication and properties of CNT-paper composites

CNT-paper composites are fabricated by coating CNT networks on cellulose fibers. Most research has focused on a method to combine CNTs with cellulose fibers. Using shear loading or ultrasonication, CNTs and resin have been mixed to form a composite [63, 64]. When the resin is highly viscous, however, conventional mixing methods are not effective. In such cases, CNTs could be directly grown [65, 66], oriented by electrophoresis [67], or assembled by chemical reactions [68, 69]. As a substrate for multifunctional composites, a prepared cellulose fiber matrix (e.g. paper) is a good choice to avoid such cumbersome steps. Liquid drops of a CNT suspension can be evaporated on paper templates [70-72]. Interestingly, the CNT composite using a paper-substrate was found to have a higher sensitivity than the mixing approach. The higher sensitivity was resulted from the microporous paper template and the larger surface area of the CNT-cellulose composite [73]. However, a manufacturing method to process CNT-paper composites has not been actively investigated, partially due to lack of knowledge about the interfacial behavior associated with manufacturing process.

1.3.2 Paper based CNT composite

As a key filler material, carbon nanotubes (CNTs) are embedded in cellulose fibers. CNTs are an excellent candidate among nanomaterials for adding various characteristics [63]. For example, adding CNTs to paper significantly enhances its thermal and electrical conductivity [74]. This combined matrix is highly applicable to flexible electronics [75] and energy storage [70, 71, 76]. The large surface area of a CNT-paper matrix can be

advantageous for sensor applications as well [75, 77-79]. An actuator can also be fabricated from a single sheet of CNT-paper composite [80]. CNT-paper matrix significantly enhances the generation of electric currents from an aluminum-air battery by catalyzing the production of hydroxyl ions in the cathodic half-reaction[72]. The microporous cellulose fibers offer ion transport between anode and cathode while the CNTs enhance the electrical conductivity and catalytic activity.

In spite of a great potential for CNT-paper composites, the application to the field of mechano-electric sensors is limited due to the lack of (1) the fundamental understanding of the multifunctional mechanisms and (2) the manufacturing process of the CNT-cellulose fiber matrix. Previous research has focused mainly on developing high-strength [81] and high-conductivity materials [82]. The study on the interface between CNT and cellulose fibers is yet to be conducted for understanding their mechano-electrical sensing mechanism. It is particularly scarce about how the interfacial characteristics can be controlled to tune the mechano-electrical transduction. To date, the interfacial behavior among flexible fibers, CNTs, and polymer has been investigated in the contexts of large strains [83, 84].

In summary, despite the great potential of CNT-paper composites in various fields, the interfacial behavior of CNT-cellulose fibers in conjunction with manufacturing process is yet to be clearly understood. For sensing applications, one of the major challenges is to understand the mechano-electrical behavior of a CNT-paper composite upon external load, which will be a stepping stone to manufacture a sensor array.

1.3.3 CNT-paper composites sensing

The conductivity of CNT is sensitively changed to chemical vapors [85]. Various CNT based chemical sensors have been studied and applied to different sensing systems.

Paper-based sensors combined with CNTs take the advantages of both materials. In other words, the low cost, flexibility, porous structure, light weight and bio-compatibility of the paper is combined with the good electrical conductivity, high sensitivity to chemical vapors and good adhesion to the cellulose surface of CNTs. In addition to its great performance in chemical sensing fields,

CNT-paper nanostructure has more possibilities in physical sensing fields, such as the strain sensing and pressure sensing [52]. Compared with other nanomaterials, CNTs have higher mechanical and electrical properties. Its high surface area provides better performance in both chemical and physical sensing while CNT based composite is fabricated.

The chemical sensing of the CNT paper composite is widely used in gas sensors such as the ammonia sensor and oxygen sensors. With the CNTs evenly distributed in the porous network of cellulose fibers, the CNT's conductivity will be affected when exposed to ammonia and oxygen [86]. Therefore, a certain type of gas sensor can be manufactured [87]. The selectivity of the CNT based gas sensor is presented in Table 1.3 [31].

Due to the porous structure and the large surface area of the cellulose fibers network, water molecules are easily been absorbed by paper and by the CNTs coated on the cellulose fibers. A paper based humidity sensor using CNT-paper composite shows a good linearity and sensitivity [87]. The composite shows a potential application to the daily health monitoring of sweat level. Besides the water vapor sensing, when the CNT-paper sensor is immersed into the water, the composite shows a high sensitivity [46]. Using the composite, liquid leaking can be detected in certain environment.

The physical CNT-paper sensor is able to detect physical inputs, such as strain, force and pressure. The paper based sensor can be attached on curved surface, therefore, can be developed into wearable sensors that can measure the strain change in different positions. Figure 1.7 shows an example of paper based wearable sensor using graphite [52]. The light weight and bio-compatibility of the paper is beneficial to development of various wearable sensors.

Table 1.3 Selectivity of SWCNT to various gas [31].

	NO_2	O_2	H_2O	NH_3	CH_4	CO_2	H_2	N_2	Ar
(10, 0) SWNT									
d (Å)	1.93	2.32	2.69	2.99	3.17	3.20	2.81	3.23	3.32
E_a (meV)	797	509	143	149	190	97	113	164	57
Q (e)	−0.061	−0.128	0.035	0.031	0.027	0.016	0.014	0.008	0.01
Site	T	B	T	T	C	C	C	C	C
(5, 5) SWNT									
d (Å)	2.16	2.46	2.68	2.99	3.33	3.54	3.19	3.23	3.58
E_a (meV)	427	306	128	162	122	109	84	123	82
Q (e)	−0.071	−0.142	0.033	0.033	0.022	0.014	0.016	0.011	0.011
Site	T	B	T	T	C	C	C	C	C
(17, 0) SWNT									
d (Å)	2.07	2.50	2.69	3.00	3.19	3.23	2.55	3.13	3.34
E_a (meV)	687	487	127	133	72	89	49	157	82
Q (e)	−0.089	−0.096	0.033	0.027	0.025	0.015	0.012	0.006	0.01
Site	T	B	T	T	C	C	C	C	C

[a] Tube–molecule distance d is defined as the nearest distance between atoms on the molecule and the nanotube for T site, or the distance between the centre of the gas molecule and the centre of the carbon hexagon (carbon–carbon bond) for the C (B) site. The adsorption energy $E_a(d)$ is defined as the total energy gained by molecule adsorption at equilibrium distance: $E_a(d) = E_{tot}(\text{tube} + \text{molecule}) - E_{tot}(\text{tube}) - E_{tot}(\text{molecule})$. Charge transfer Q denotes the total Mulliken charge number on the molecules, positive Q means charge transfer from molecule to tube.

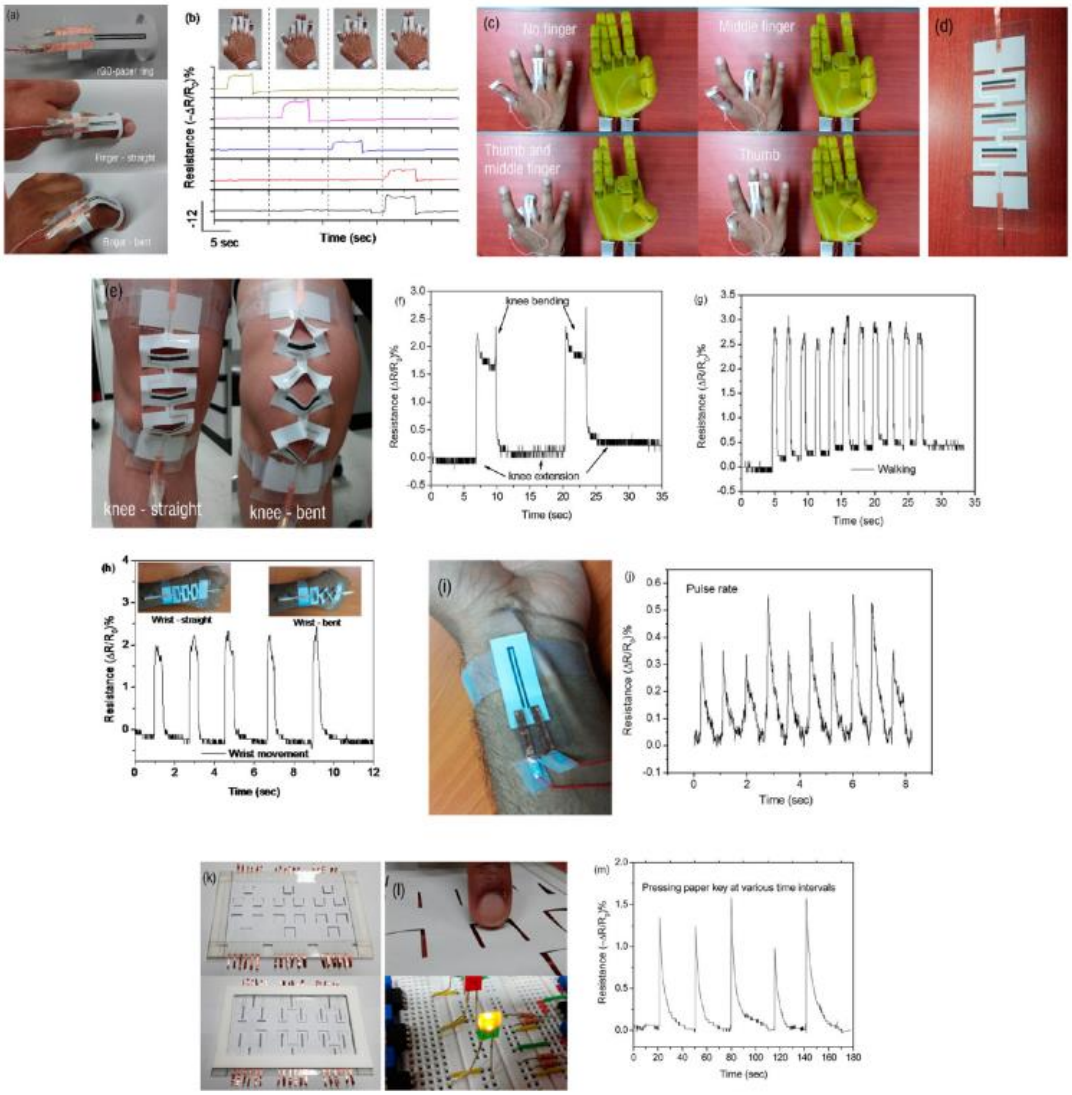

Figure 1.7 Wearable electronics and keyboard applications. (a) Photographs of an rGO-paper ring and its extended and bent positions. (b) Response signals of five independent rGO-paper rings monitoring the positions of various fingers. (Top insets) Photographs of the hand in the four different positions corresponding to the plotted signals. (c) Control of the middle finger and thumb of a 3D-printed robotic hand using rGO-paper rings. (d) Photograph of an rGO-paper kirigami prepared using the multilayer masking process. (e) Photographs of a knee in extended and bent positions while wearing rGO-paper sensors. Changes in the resistance of an rGO-paper sensor on a knee during (f) sitting and (g) walking. (h) Response curve due to the movement of a wrist. (i) rGO-paper sensor attached to the wrist for detection of pulse, and (j) corresponding signal from the rGO-paper sensor. (k) Photographs of the top and bottom sides of a paper keyboard. (l and m) Touching a paper key to light an LED and the corresponding signal from the paper key [52].

In summary, CNT-paper composite is an ideal material for chemical and physical sensing, with advantages of being cheap, disposable, flexible, light weighted and bio-compatible. Its potential applications in wearable sensors, medical care, environmental monitoring and robotics are very promising. However, the CNT-paper composite lacks the necessary selectivity for different gas molecules. The hysteresis and creeping issue needs to be improved. The reliability of the sensor can also be a problem because the chemical sensing can involve certain irreversible reaction between CNTs and chemical molecules. The treatment method of the CNTs on cellulose fibers needs to be further investigated.

1.4 Objectives

The main objective of the dissertation is to study the fabrication mechanism of mechano-electrical sensor of a CNT-paper composite (CPC) and to develop the fabrication process and the application for various wearable sensors. The key challenges to the fabrication of the composite sensor are addressed.

A low cost fabrication method of CPC is proposed, with a controlled fracture for the nanostructure of the nanocomposite as follows. CPC's mechanical and electrical properties are characterized using a tensile test setup and electrical measurement. The novel fracture induced sensitivity of the CPC is characterized in the contexts of the cellulose fibers' behavior and CNTs' junctions. The sensing mechanism related to the nanostructure transformation is discussed. Three different sensor types based on the fractured CPC are presented. The manufacturing process for the wearable sensors are developed. For application, a humidity sensor is characterized and developed. A pressure sensor monitoring foot walking is developed.

Chapter 2. CNT-paper Composite's Mechanical and Electrical Properties

2.1 Background

Nanostructured composites using cellulose fiber templates have been studied for developing light-weight and inexpensive devices. Cellulose fibers extracted from wood pulp offer large surface area facilitating energy, sensing and electronic applications [47, 48]. Since the porous and hydrophilic nature of cellulose fibers enhances adhesion, various nanomaterials have been used to modify the surface properties of cellulose fibers for multifunctionality. Carbon nanotubes (CNTs) are versatile filler materials to create electrical and thermal conductivity [74]. When a CNT-paper composite (CPC) is fabricated, novel applications are being developed, such as flexible electronics [75], energy devices [70-72, 76], and sensors [75, 77-79]. However, the random network of CNTs in a cellulose fiber matrix limits the mechano-electrical sensitivity due to the numerous current paths in the matrix.

We present a fracture-induced mechano-electrical sensitivity of a CPC for wearable sensing applications. With precise control of the applied strain under uni-axial load to a CPC, the tensile directional fibers coated with CNTs are fractured, and the cellulose fibers inclined or orthogonal to the tension are reoriented to form crossbar junctions near a crack. The junctions create highly sensitive resistive and capacitive responses for measuring strain, force, and non-contact displacement. The novel manufacturing process allows the integration of flexible sensors in low-cost tissue paper, which is easily adapted to human body for behavior monitoring.

The study on mechanical and electrical property of the CNT-paper composite is important to understand the sensing mechanism using the composite and further application. Similar CNT-polymer composite's mechanical and electrical properties have been studied [88]. Unlike the previous composite, the proposed composite is composed of soft tissue paper and CNTs. As a novel paper based composite, a rigorous understanding of the mechanical and electrical property is the foundation of further discussion. Also, in previous studies, the fracture of the composites and its effect during the tensile test has not been discussed. In this chapter, the result of the mechanical and electrical test of the CNT-paper composite is presented. The effect of the CNT deposition and the fiber orientation is studied.

2.2 Fabrication process of CNT-paper composite

A 100 μm-thick porous paper (KimWipes®) was used as a template. An aqueous solution of MWCNTs (Nano structured & Amorphous Materials, Inc) was prepared by using 1% sodium dodecyl sulfate (SDS) in deionized water. After 2 hour-sonication, the solution was deposited on a suspended paper using a pipette. When MWCNT solution was introduced to a cellulose fiber matrix, MWCNTs were bound on fibers and spanned between fibers by capillary action. The CPC was cut into pieces (10×30 mm^2). For electrodes, silver epoxy (MG chemical #8330s-21G) was pasted onto both ends of the composite for a 10x10 mm^2 area. The specimen was cured in an oven at 65°C. Silver paste was applied to both ends of the paper strip and cured to fabricate electrodes.

Figure 2.1 shows the fabrication method of a CPC sensor. A 100 μm-thick porous paper (KimWipes®) was used as a template. An aqueous solution of multiwall carbon nanotubes (MWCNTs) (5 mg/mL; Nanostructured & Amorphous Materials, Inc., Houston, TX) suspended in a surfactant (sodium dodecyl sulfate; SDS; 1%) was deposited onto porous paper. When MWCNT solution was introduced to a cellulose fiber matrix, MWCNTs were bound on fibers and spanned between fibers by capillary action. Silver paste was applied to both ends of the paper strip and cured to fabricate electrodes. The composite was stretched to induce a crack due to the fracture of the tensional directional fibers. The fractured composite was attached on a double-sided adhesive tape and sealed by sticky tape to fabricate a prototype sensor.

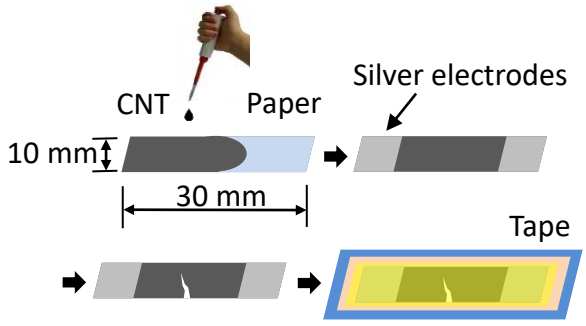

Figure 2.1 Fabrication process of CPC.

2.3 CNT-paper composite's mechanical property

The mechanical property of the CPC is studied by the tensile test. The nanocomposites were tested by using a custom-made uniaxial tensile test bed that was controlled by using LabView interface in Yang's laboratory of Aeronautics & Astronautics. The force and displacement were recorded for stress-strain relationship. Real-time, high-resolution video was used to observe the nanocomposite's behavior as well as its morphologies and failures under mechanical loading. The resolutions of the force and displacement sensors were 3mN and 1μm, respectively.

In this test, two factors were studied; the orientations of the fibers and the CNT deposition conditions. The composites deposited with 0, 3, 10, and 20 times of MWCNTs were prepared to vary electrical paths. The number of depositions was limited to 20 at which the cellulose fiber matrix was fully saturated with MWCNTs. In this study, the tension direction is defined as 0° ('parallel') and the direction orthogonal to tension is 90° ('perpendicular').

The mechanical strength change of a CPC under the uni-axial load according to the deposition numbers (Figure 2.2) were characterized. The paper was composed of randomly oriented cellulose fibers as shown in the histogram of Figure 2.3. The stretching direction was perpendicular to the dominant fiber orientation. The stretching parallel to the orientation of the dominant fibers was presented in Figure 2.4. In the test, the stress-strain relationship was not as consistent as the parallel direction. The perpendicular wrinkles that were generated during the manufacturing of the tissue paper resulted in the unpredictable strain at the ultimate strength for the parallel stretching. (Figure 2.5).

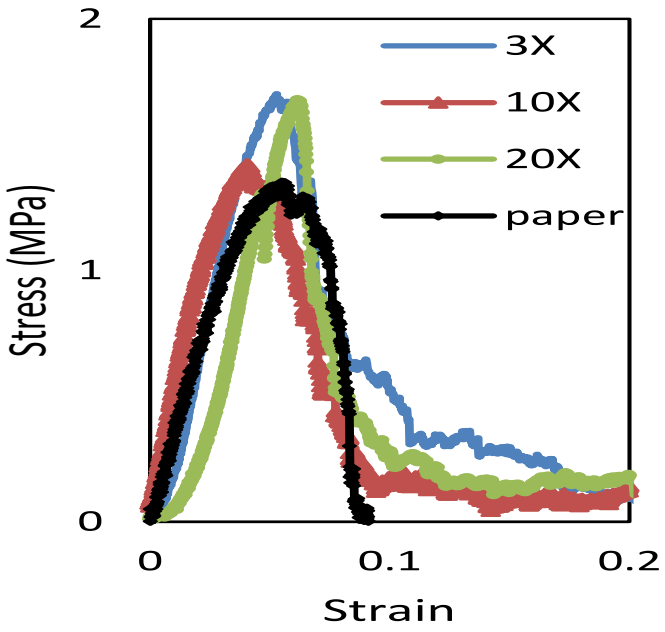

Figure 2.2 Stress-strain characteristics for composites of plain paper (black), 3x (blue), 10x (red) and 20x (green) depositions. Stretching perpendicular to the dominant fiber orientation.

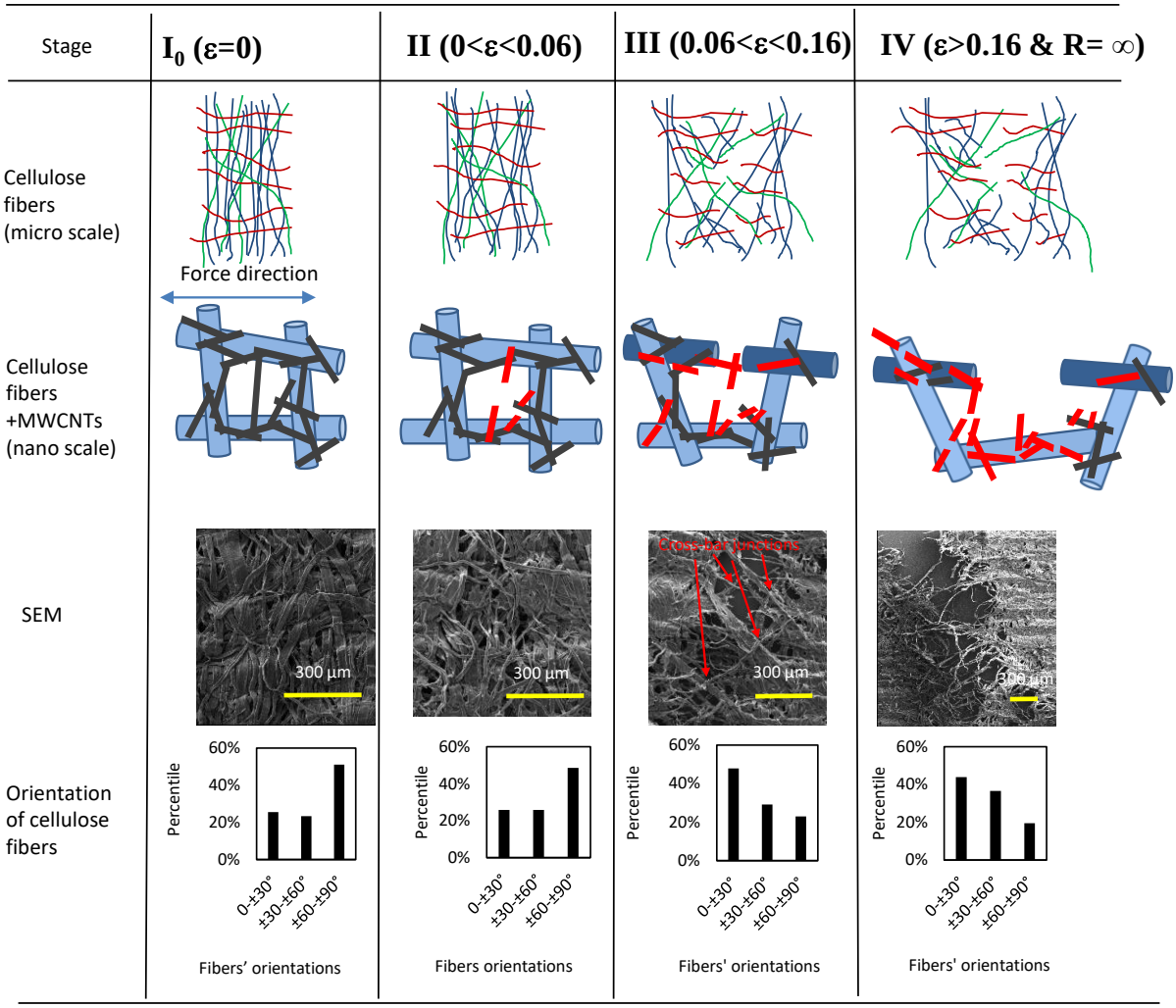

Figure 2.3 Schematics of the micro and nano structure reorientation of the composite, SEM images, and orientation statistics according to the applied strain.

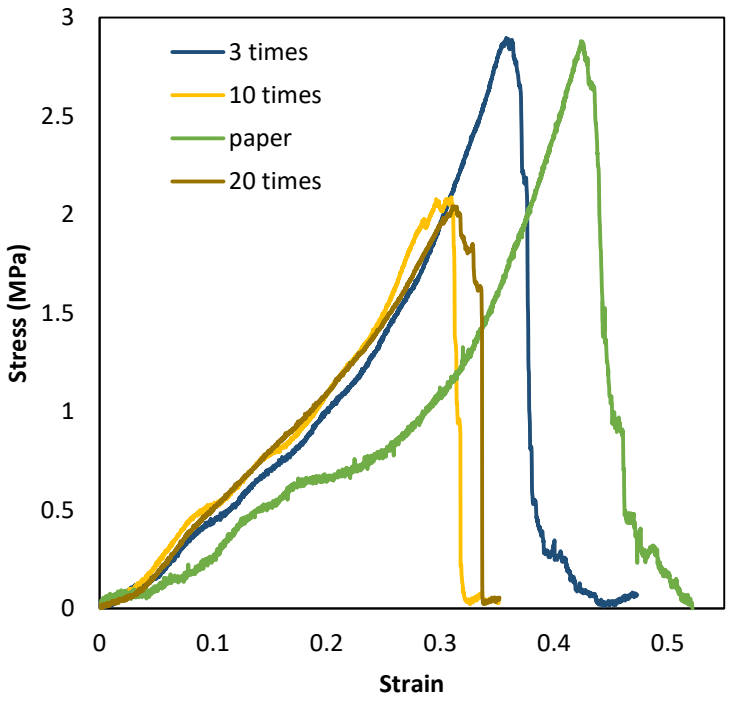

Figure 2.4 Stress-strain relationship for plain paper and CPC deposited with 3, 10 and 20 times. The stretching is parallel to the dominant fiber orientation.

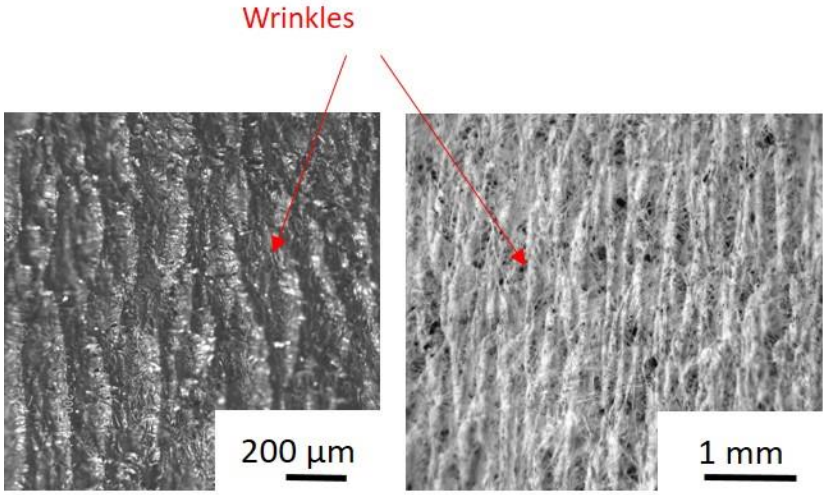

Figure 2.5 Optical microscope images of the wrinkles of the composite (3 times coated paper and plain paper).

In Figure 2.2, regardless of the deposition numbers, the ultimate strength and its strain were in the range of 1.47±0.12 MPa and 0.053±0.0056 mm/mm, respectively. The stiffness became larger with the increase of the deposition numbers (Figure 2.6). Based on the scanning electron microscopy (SEM), cellulose fibers were bridged and coated with the deposited MWCNTs (Figure 2.7), which increased the composite stiffness.

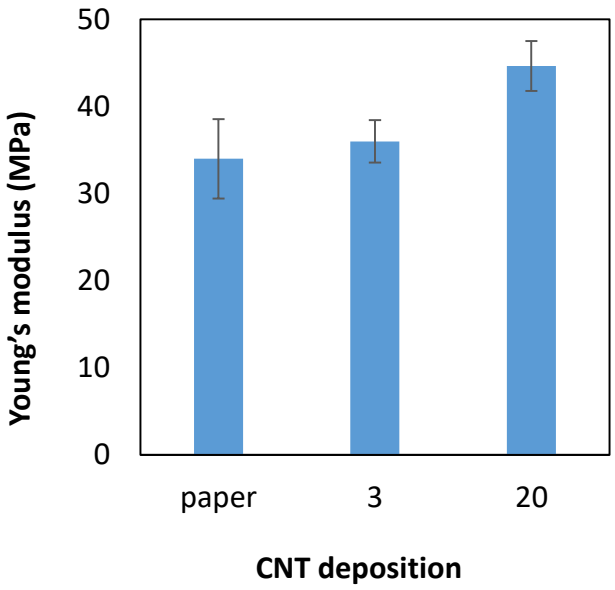

Figure 2.6 Young's modulus for plain paper and CPC deposited with 3 and 20 times.

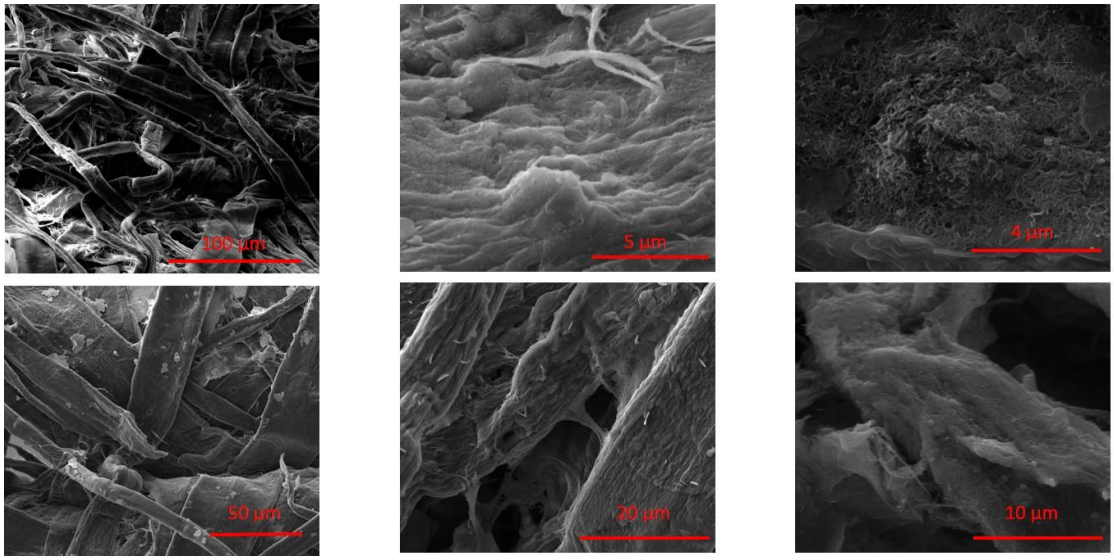

Figure 2.7 SEM images of the cellulose fibers for plain paper and CPC deposited with 3 and 20 times.

2.4 CNT-paper composite's electrical property

The electrical property of the CNT was studied by the tensile test. The resistance change of the CPC was recorded while the specimen was stretched.

The sheet resistance of the CPC decreased as the number of MWCNT depositions increased (Figure 2.8). The composite resistance in the stretching direction was slightly lower than that of the orthogonal direction.

When the electrical resistance was measured under tension, the inflection point of the resistance change was clearly lagged from the strain of 0.06 to 0.08 mm/mm as the deposition number increased from 3 to 20 (Figure 2.9). The inflection point was where the resistance change deviated the initial linear slope by 5%. As the more cellulose fibers were bundled with more depositions of MWCNTs, the significantly increasing point of the resistance was delayed.

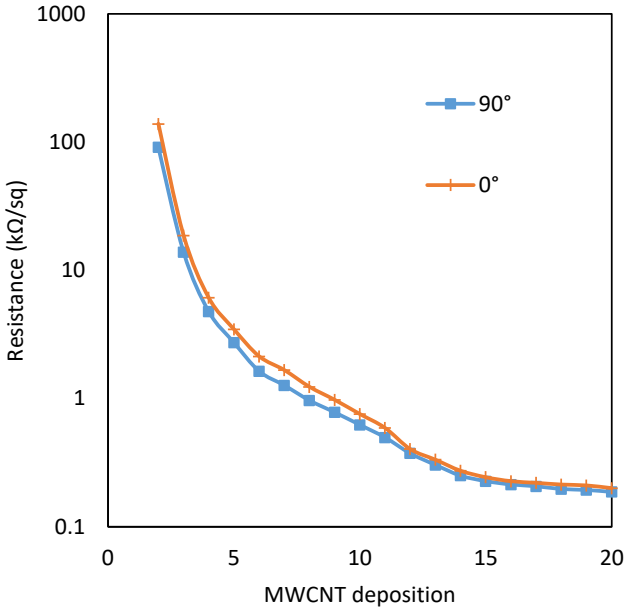

Figure 2.8 Sheet resistance of a composite for a MWCNT deposition number for both 0° and 90°directions.

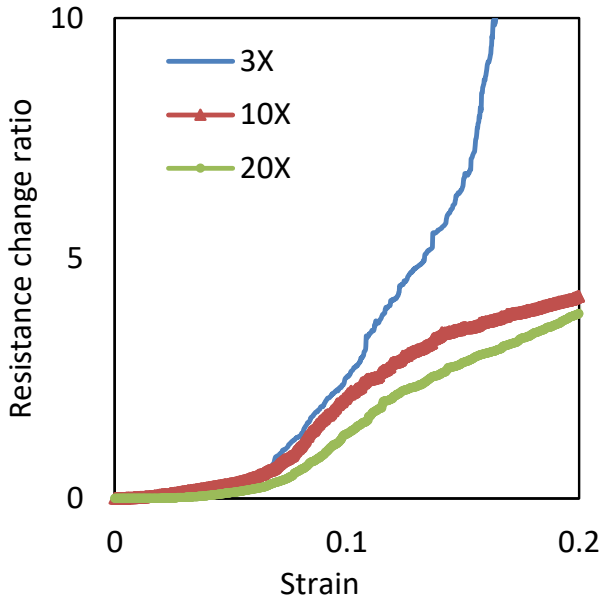

Figure 2.9 Relative resistance change for composites of plain paper (black), 3x (blue), 10x (red) and 20x (green) depositions. Stretching perpendicular to the dominant fiber orientation.

The electrical resistance increased with a power law, which agreed with the percolation theory [89-91]. The effective resistivity of a composite network can be expressed as $\rho_c = \rho_f (f - f^*)^{-t}$, where ρ_f is the resistivity of fiber, f is the conductor volume fraction, f^* is the critical conductor volume fraction, and t is an exponent. Since the fiber network in our composite is degenerated with stretching, the resistance change ratio (R/R_0)can be expressed with strain (ε) as $\frac{\Delta R}{R_0} = a\varepsilon^b$, where R_0 is the initial resistance, ΔR is the resistance change $(R - R_0)$, and a and b are the parameters that are determined by the MWCNTs depositions. The estimated a and b for 3, 10, and 20 depositions were 1.82×10^{42}, 4.49×10^{4}, 1.67×10^{4} and 39.0, 4.0, 4.0, respectively. The more MWCNTs were deposited, a and b were smaller because the bundled MWCNTs lagged the inflection point of the resistance change.

2.5 Discussion

The nanostructure was reorganized as CPC was stretched and fractured. It was resulted from the structural change of the cellulose fibers and the MWCNTs coated on the fibers. The CPC was characterized under four different stages (Figure 2.3) during the stretching.

Figure 2.3 shows the structural change of the cellulose fibers and MWCNTs under tension based on optical and SEM study. A CPC with 3 times of MWCNT depositions was used for this study because more than 10 depositions could hamper reorganization of fibers. The creation of piezo-sensitivity stems from the realignment and fracture of CPC network under tensile loading. The bottom graphs of Figure 2.3 show the percentile histogram of the fiber orientations in stage of I_0, II, III, and IV. According to the SEM observations, the fiber orientations in the area of 1 × 1 mm^2 were divided into three ranges of 0~±30°, ±30~±60°, and ±60~±90°. In the original paper template (stage I_0), 26% of the fibers were in 0~±30°, 23% in ±30~±60°, and 51% in ±60~±90°. Therefore, the dominant orientation in the initial composite was ±60~±90°. Here 0° and 90° imply parallel and perpendicular directions to the loading.

In stage II ($0<\varepsilon\leq0.06$), the parallel fibers were straightened and stiffened by tension. The resistance increase was resulted from the breakage of the MWCNT bridges spanning neighboring cellulose fibers. Although a CPC was stretched in an elastic range, the resistance was not recovered to the original value due to the broken MWCNT bridges (Figure 2.10).

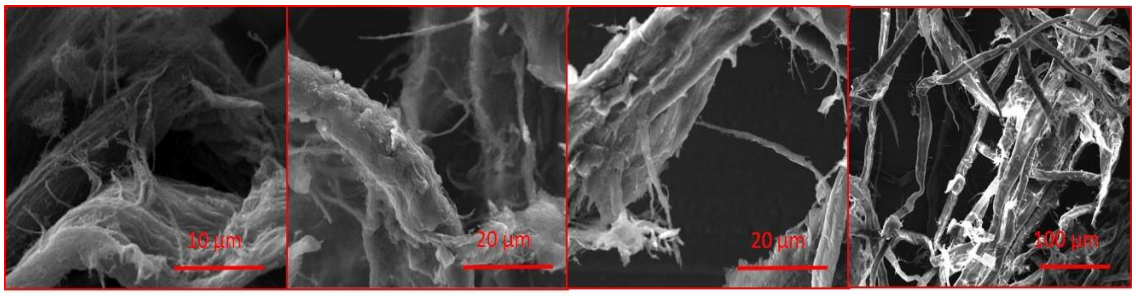

Figure 2.10 SEM images of the nanostructure of CPC coated with 3 times of MWCNTs at different strain stages. MWCNTs span and coat cellulose fibers at stage I0. As the strain increases, the spanning MWCNTs are broken followed by the fracture and separation of cellulose fibers coated with MWCNTs.

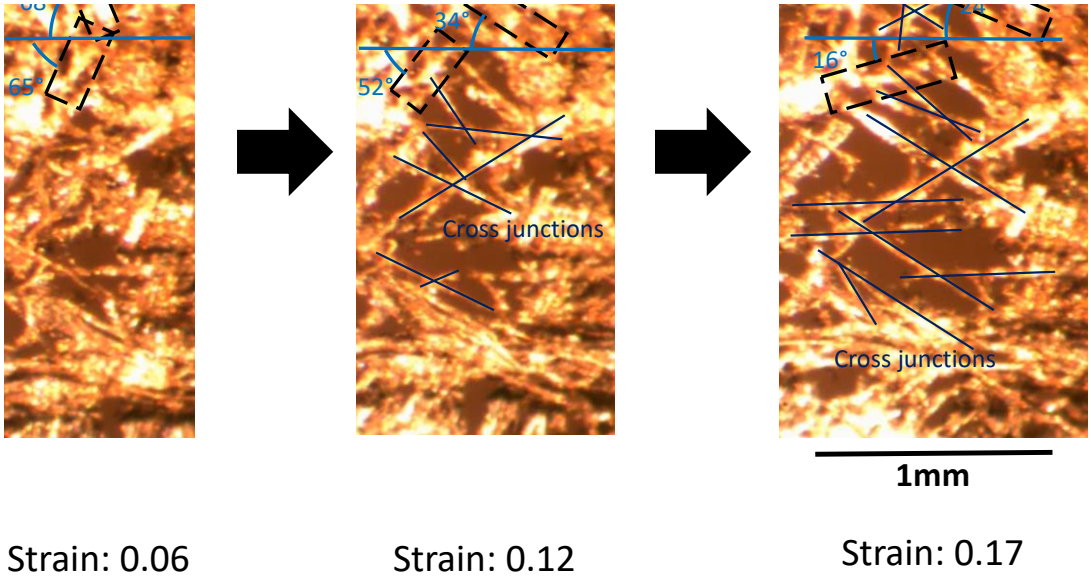

Figure 2.11 Orientation and cross-junction formation of cellulose fibers according to strain.

In the strain of 0.06~0.16 (stage III), most parallel fibers were fractured at ultimate strength. Both inclined and perpendicular fibers were oriented to the tensile direction, which changed the dominant orientation of fibers into ±0~±30° (see the histogram in Figure 2.3, and Figure 2.11). Both spanning and coated MWCNTs on fibers were broken. The reorganized fibers (green and blue fibers in Figure 2.3) formed numerous cross-shaped junctions (Figure 2.12). Electrical resistance was significantly increased as the MWCNT network among the fractured fibers was broken.

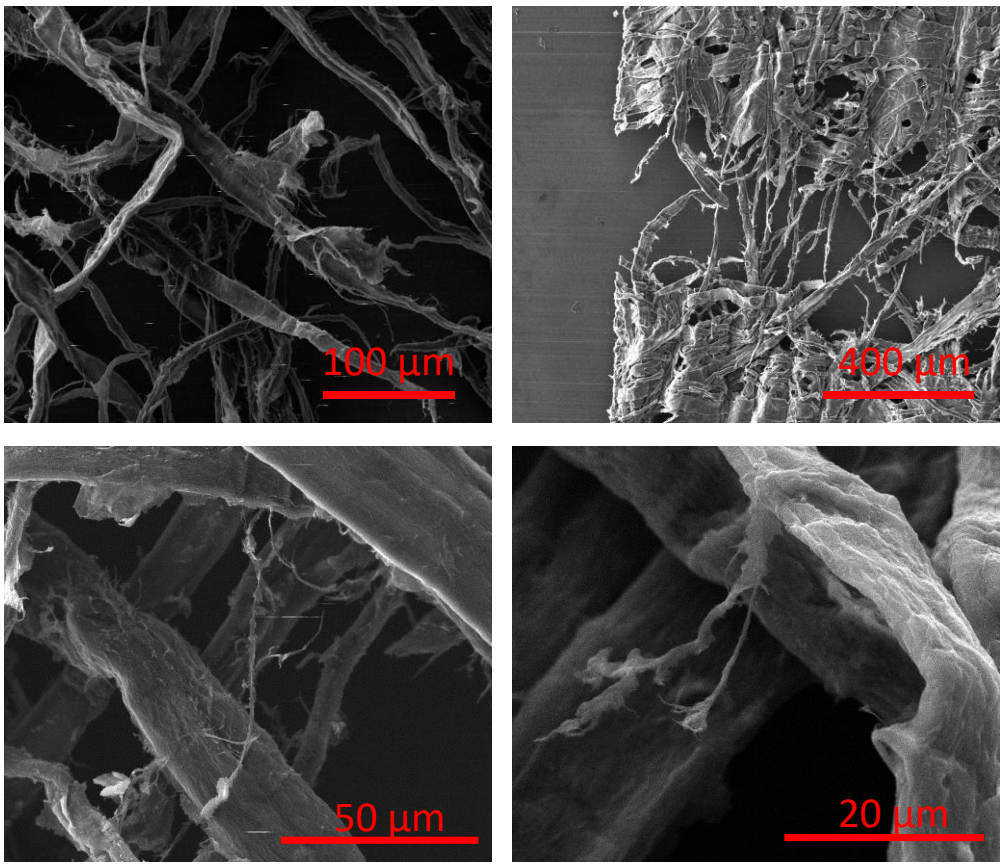

Figure 2.12 SEM images of the cross junction structure of the fractured CPC (pre-strain: 0.12). MWCNTs were coated by 3 times.

At the stage where the strain was greater than 0.16 (stage IV), all the electrical connections were broken by extreme stretching. The composite was electrically terminated along the crack edge, which was clearly observed from the bright and dark contrast in the SEM image (Figure 2.3). The high contrast indicated that electrons could not flow through the crack edge. In the orientation graph, the fraction of the parallel and inclined fibers (0~±30° and ±30~±60°) became 80%, forming crossbar junctions. Since the resistance became infinite, pure capacitance of the MWCNTs could be measured through the dielectric media of air and fibers.

Chapter 3. Fracture-induced Sensitivity of CNT-paper Composite

By the control over the applied strain to the CPC, three types of sensors (a strain sensor, a piezo-resistive sensor and a piezo-capacitive sensor) can be designed in the stages II, III, and IV, respectively. To demonstrate this, a series of prototypes were fabricated in stages II~IV.

3.1 Strain sensor

The CPC pre-strained at the stage II by applying 0, 0.02, 0.04 and 0.06 of strains was prepared and attached to a polydimethylsiloxane (PDMS) cantilever beam for the sensor evaluation (Figur**e** 3.1a). With the bending of the cantilever, the top surface of the beam was stretched, which linearly increased the sensor resistance (Figure 3.1b). As the pre-strain increased from 0 to 0.06, a gauge factor ($\frac{\frac{\Delta R}{R_0}}{\Delta \varepsilon}$) increased from 2 to 13 (Figure 3.1c). The increase of the gauge factor in the elastic region was caused by the breakage of the MWCNT bridges among the intact cellulose fibers. Therefore, a pre-strain could partially remove the electron paths spanning cellulose fibers, which increased the sensitivity.

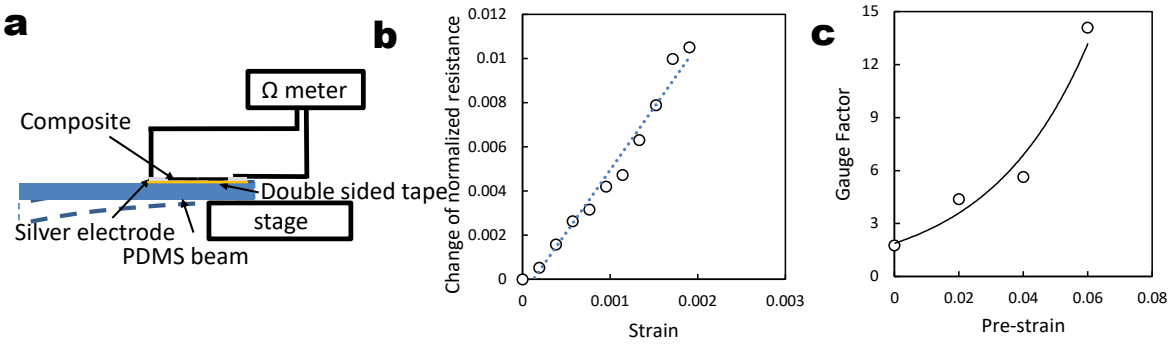

Figure 3.1 Evaluation of the strain sensor in stage II. (a) Schematics of the strain sensor design and calibration. (b) Normalized resistance change according to the applied strain by bending (pre-strain: 0.04 mm/mm; 3×MWCNT depositions). (c) Gauge factor according to the pre-strain that is applied for a CPC.

3.2 Piezo-resistive sensor

In stage III, the reoriented cellulose fibers in the crack generated a sensitivity for out-of-plane directional force. The sensing performance was evaluated by recording the electrical resistance change with respect to the applied force. An elastomeric finger was fabricated using PDMS to mimic a human finger (Figure 3.2a). To calibrate the applied force, a force sensor (LCFD-1KG, Omega Engineering, Norwalk, CT) was attached under the sensor substrate. As the force was applied on the cracked area of the composite, the untangled crossed fibers generated in the fracture were compressed to increase the contact area, which decreased the resistance in proportion to the force (Figure 3.3).

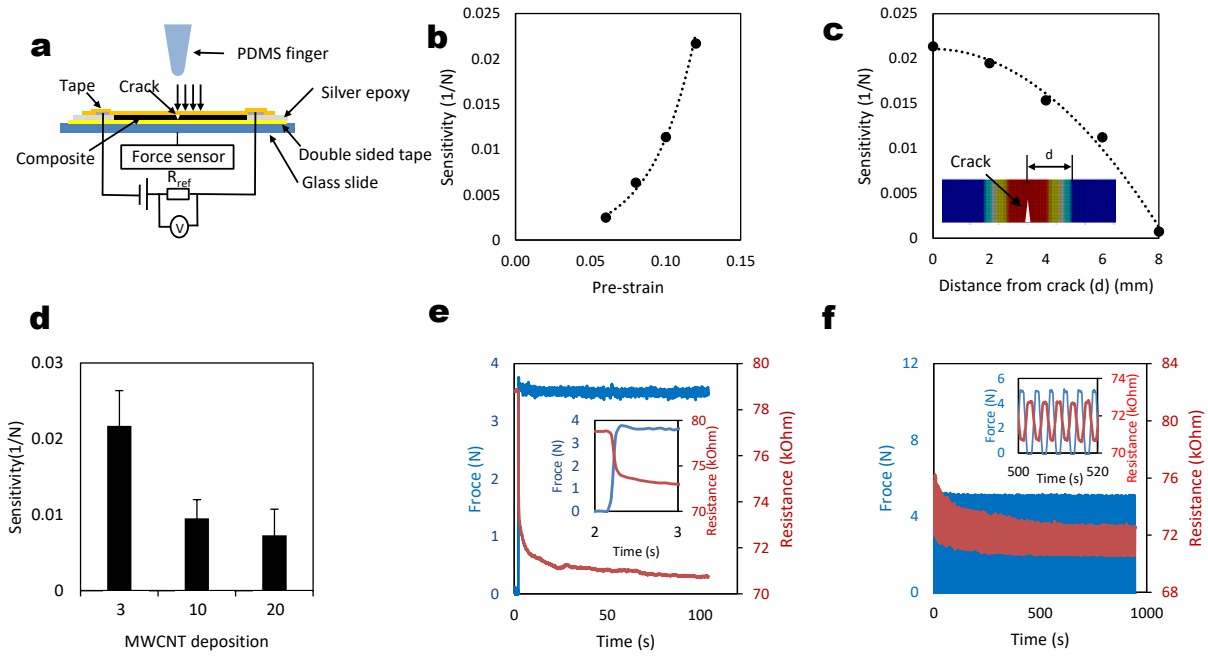

Figure 3.2 Evaluation of a piezo-resistive force sensor in stage III. (a) schematics of piezo-resistive force sensor calibration. Force and voltage are recorded when the cracked area of a sensor is pressed by a PDMS finger. Inset is the picture of the testing setup. (b) Sensitivity variation for various applied pre-strain. (c) Sensitivity variation for different locations on a cracked sensor. (d) Sensitivity variation for 3×, 10×, and 20×MWCNT depositions. (e) resistance response to a step force input of 3.5 N. Inset: closeup of the response time. (f) resistance variation for cyclic loading (0.3Hz). Inset: closeup of the electrical response for 500~520 seconds.

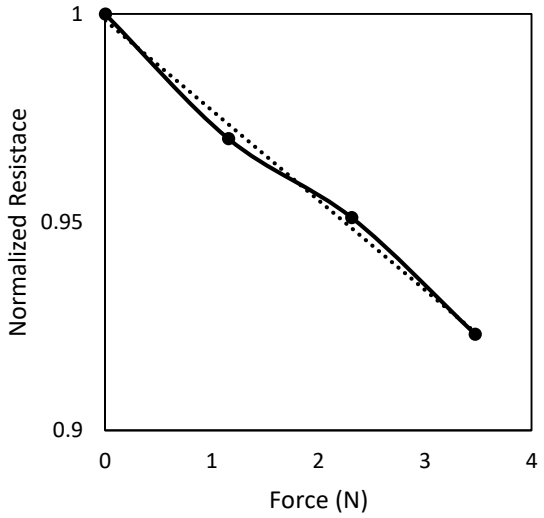

Figure 3.3 Normalized resistance change for a compressive force.

The piezo-resistive sensitivity was increased by larger pre-strain (Figure 3.2b). As the pre-strain increased from 0.06 to 0.13, the sensitivity rapidly increased from 0.002 to 0.023 N^{-1}. Without the pre-strain, the piezo-sensitivity was close to 0 because the cellulose fibers were firmly bonded with numerous MWCNT network. To validate if the sensitivity was created by a crack, the forcing point was moved away from a crack, step by step. The sensitivity was continuously reduced from 0.022 to 0.001 N^{-1} as the distance increased (Figure 3.2c). When the distance from the crack was greater than 8 mm, the composite was not sensitive to an out-of-plane force. To test the reproducibility and the MWCNT deposition effect, the composites deposited with 3, 10 and 20 times were stretched by pre-strain of 0.12 mm/mm. The sensitivity was reduced as the deposition numbers increased because more bundled fibers by MWCNTs limited the structural change under tension (Figure 3.2d). With more depositions, fewer junctions were created to lag the increase of the resistance, thus the sensitivity.

When a step force input was applied to a composite with a 0.12-prestrain, the response time was less than 50 ms, which was significantly smaller than other polymer sensors (Figure 3.2e). However, the resistance offset was continuously reduced for 100 seconds. Under the force, the cellulose fibers continuously slipped and creeped, which caused the continuous decrease of the resistance. When a cyclic loading (frequency: 0.3Hz) was applied between 0 to 5.5 N, the resistance changed periodically, and the resistance offset reached a steady state after 300 s (Figure 3.2f). The response of the sensor pressed by a human finger was relatively reliable for 500 cycles (Figure 3.4).

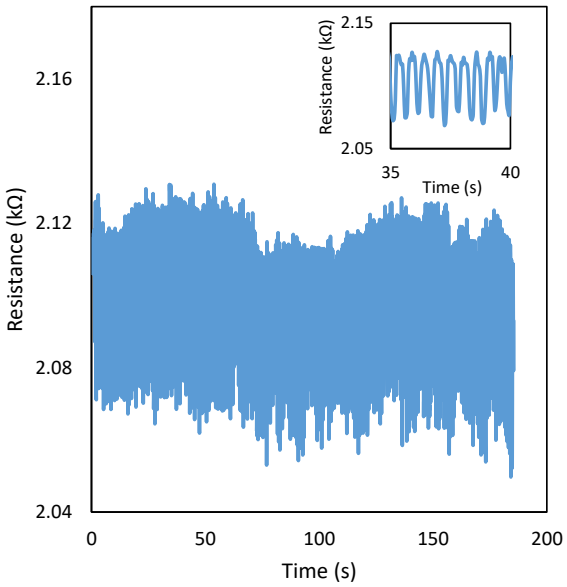

Figure 3.4 Resistance change for a cyclic finger force on the sensor. Inset: close up of the resistance change for 35~40 seconds.

3.3 Capacitive sensor

In stage IV, a capacitive sensor could be created. Since the final fracture of the composite was not predictable, the applied pre-strain was stopped when the resistance became larger than 500 MΩ. Similar to the piezo-resistive sensor, junctions were created by the crossed structure of cellulose fibers. Due to the large surface areas of cellulose fibers and MWCNTs, intrinsic capacitance without parasitic capacitance was so large as 0.5±0.04 pF (N=6). The capacitance sensor could detect conductive objects by contact and non-contact modes, and non-conductive objects by a contact mode using the setup in Figure 3.5. Note that the composites deposited with 10 and 20 times MWCNTs could not be used to create a capacitive sensor because the bundled fibers by MWCNTs made the CPC electrically conductive till the complete fracture.

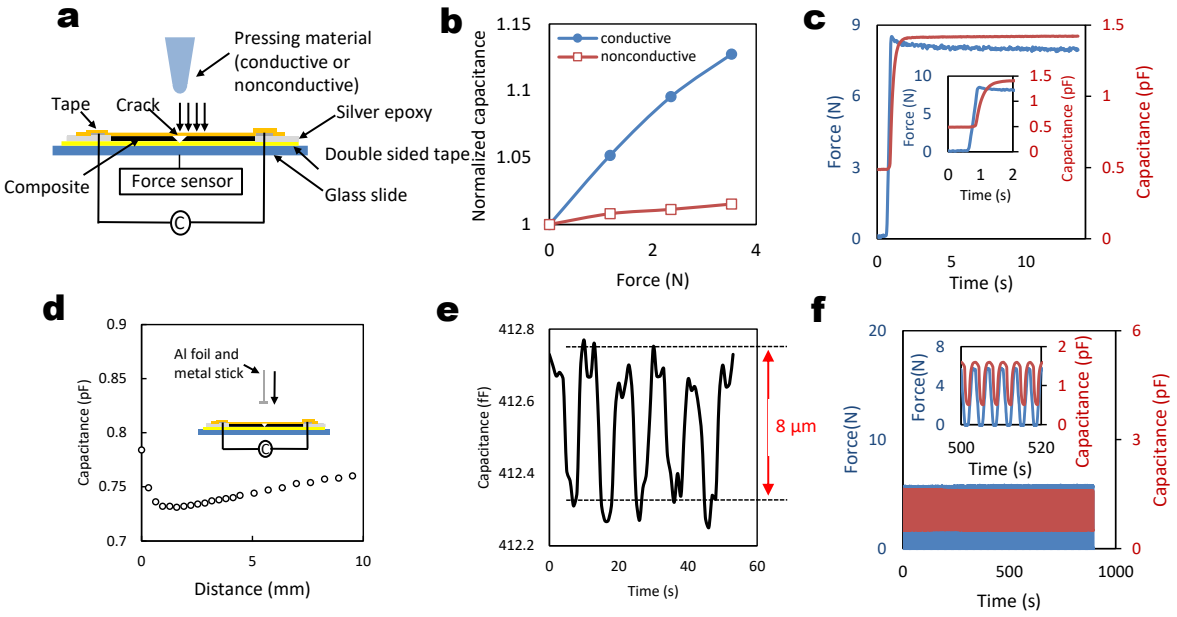

Figure 3.5 Evaluation of a capacitive sensor in stage IV. (a) Schematics of Piezo-capacitive force sensor calibration. Force and capacitance are recorded when the cracked surface of the sensor is pressed. (b) Normalized capacitance change for both conductive and non-conductive object for CPC of 3×MWCNT depositions. (c) Capacitance response to a step force input of 8 N. Inset: closeup of the response time. (d) Capacitance change of non-contact displacement as a function of the distance between the sensor and a conductive object. (e) Capacitive response of a non-contact displacement sensor to cyclic displacement by a piezo-actuator (8 µm). (f) Capacitive change of a conductive PDMS finger for a cyclic force. Inset: closeup of the capacitive change between 500~520 seconds.

When a conductive finger (PDMS finger coated with aluminum) was forced on a crack, the capacitance increased with a sensitivity of 0.036 N^{-1} (Figure 3.5b). The sensitivity for the same test using a non-conductive finger was reduced to 0.004 N^{-1}. When a step input was applied, the time constant was less than 50 ms (Figure 3.5c). When a conductive object was withdrawn from the crack surface of the capacitive sensor, the capacitance was first rapidly reduced by the decrease of parallel capacitance (sensitivity: -0.068 mm^{-1}), and subsequently, increased by the reduction of charge dissipation (sensitivity: 0.0048 mm^{-1}) (Figure 3.5d). For the capacitance increase, the characteristic length between the sensor and the conductor became greater than that of the capacitance sensor, which increased the capacitance by decreasing the current dissipation to the conductor. At the -

0.068 mm^{-1} sensitivity region, the 8 μm-displacement of a piezo-actuator could be measured (Figure 3.5e). Considering the noise level, the detection limit was 1 μm. Note that the capacitance change could not be measured when a conductive object was approached to a non-cracked area. In a cyclic compressive loading of 0~5.7 N at 0.3 Hz, the sensor response was stably measured using a conductive elastomeric finger (Figure 3.5f). The capacitance changed between 0.5 and 1.5 pF, which was larger than the intrinsic capacitance due to the parasitic capacitance by the wire harness. In the setup, the parasitic capacitance was 0.2 pF.

3.4 Applications

Using resistive and capacitive sensors, human behaviors could be monitored. Both sensors could be used to measure heartbeats on wrist (Figure 3.6a and 3.6b). In the measurement, a CPC sensor on a both-side sticky tape was attached on the wrist. When a piezo-resistive sensor was attached on a finger of a glove, cyclic gripping motion could be detected (Figure 3.6c). When a sensor was attached on a finger joint, the resistance change could be measured for the angle change between 0 and 135 degrees (Figure 3.6d). A non-contact capacitive sensor was installed on an eyeglass to detect the eyeball movement (Figure 3.6e). The up/down and the open/close movement of an eye could be detected because the distance from the sensor to the eye surface was changed.

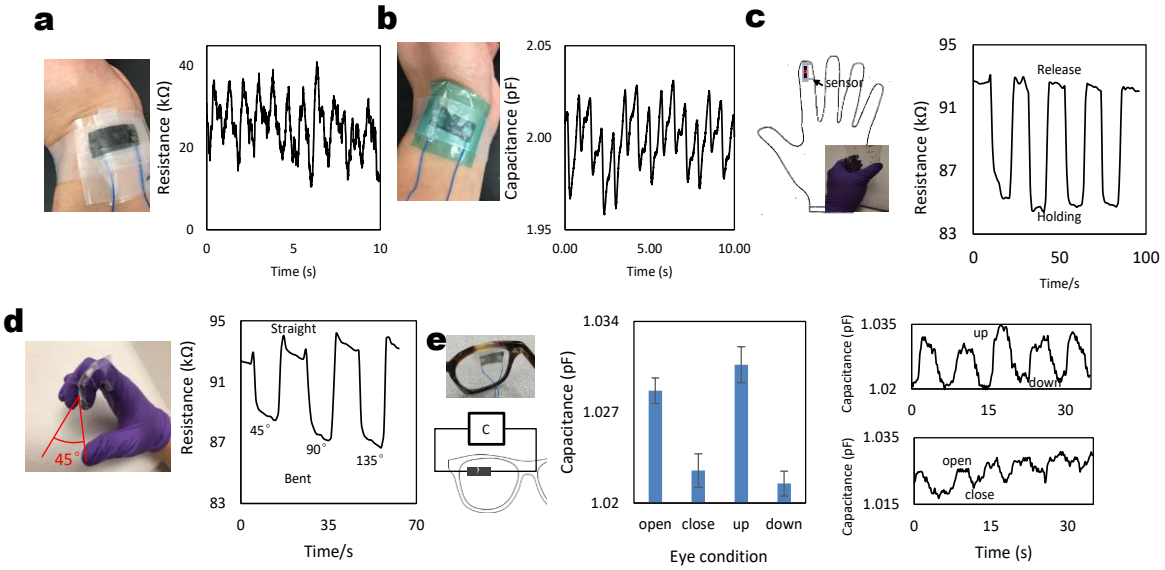

Figure 3.6 Human behaviour monitoring (a) Resistive heart beat sensor on wrist. (b) Capacitive heartbeat sensor on wrist. (c) Haptic force sensor attached on a glove. (d) Monitoring of bending of a finger using a sensor attached on a glove. (e) Non-contact capacitive sensor for eyeball and eyelid movement. Capacitive response for open/close eye lid and up/down eyeball movement.

3.5 Discussion

As illustrated in Figure 3.7, the proposed sensor can be designed and fabricated to exploit different sensing mechanisms by the magnitude of applied pre-strain (i.e., in-plane strain sensor, out-of-plane piezo-resistive sensor, and capacitive sensor in stage II, III and IV, respectively). The stress-strain relationship shows three different stages in terms of the mechanical and electrical behavior. The electrical resistance at the initial stage (I_0) increases linearly at the elastic region (stage II in Figure 3.7) by uni-directional strain. With the application of larger strain, a crack is initiated and propagated along the orthogonal direction to the tension, which significantly reduces the mechanical stiffness of composite (stage III in Figure 3.7). The electrical resistance increases drastically because of the fracture of MWCNT-coated cellulose fibers. Near the crack, the untangled cellulose fibers form crossbar junctions where the coated MWCNTs exhibit out-of-plane piezo-resistivity. With larger strain, the increased stress near the crack tip terminates the composite electrically (Resistance>500MΩ) (stage IV in Figure 3.7), although the composite is still connected by untangled fibers. The stress concentration of cellulose fibers along the crack edge increases the local strain and the deposited MWCNTs along the edge are disconnected. The numerous junctions create an out-of-plane piezo-capacitive sensor.

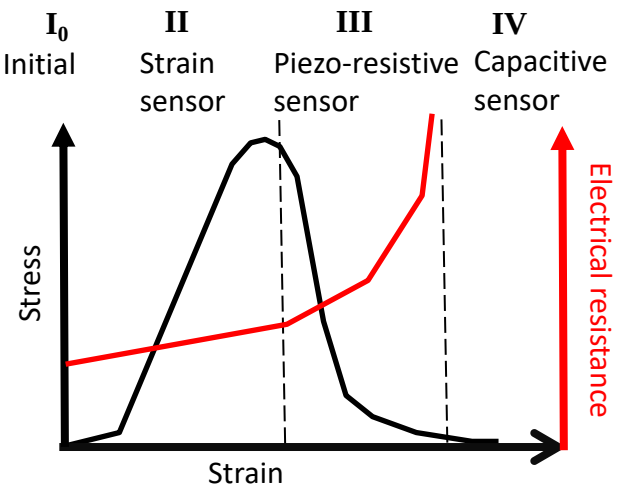

Figure 3.7 Conceptual illustration of the sensitivity generation according to mechanical and electrical properties.

Chapter 4. Polyacrylic Acid CNT-paper Composites for Humidity and Moisture Sensing

Various carbon nanotube-paper composites (CPC) have been studied to measure relative humidity. This chapter presents a tissue paper-based CPC coated with polyacrylic acid (PAA) for sensing humidity and surface moisture . When a CPC is exposed to humidity, the electrical resistance changes due to the electrostatic interaction with water molecules and the swelling of cellulose fibers and PAA. The enhancement of sensor response due to swelling of CPC coated with PAA, acid, and Nafion is studied in terms of resistance change. The hysteresis of a CPC sensor response in a cyclic humidity change is characterized for both the CPC region and the interfacial region between carbon nanotubes and a silver electrode. Based on the empirical relationship, the humidity sensor is applied for measurement of surface moisture in a simulated sweat model. The CPC surface moisture sensor provides a low-cost, highly sensitive, light-weight flexible platform potentially beneficial for sweat monitoring.

4.1 Background

Relative humidity (RH) sensors are widely used in industrial and agricultural applications, process control, biomedical uses, environment monitoring, and food storage[92-94]. Various attempts have been made to enhance the sensitivity and dynamic range of film-shaped humidity sensors[95-97]. Carbon nanotube (CNT) based sensors showed potential in improving accuracy and measurement ranges due to their large surface area[98], chemically inert surface, and hollow nanostructure[99, 100]. A multi-walled carbon nanotubes (MWCNT) humidity

sensor has shown good linearity at low humidity levels (RH<80%), but its peak resistance values were at RH~80% owing to the compensating doping effect. Acid-treatment of MWCNTs created defective sites and more nucleation sites for electron transfer resulting in the improved sensitivity[101]. Through acid treatment, more water molecules could be adsorbed onto the sensing element overcoming the compensating doping effect.

Field-effect transistors (FET) have been fabricated using single-walled carbon nanotubes (SWCNTs)[102, 103]. Bindings of water molecules onto the SWCNT surface altered electrical resistance, enabling the use of FETs for humidity measurements. MWCNTs deposited between interdigitated Au electrodes have been used for capacitive humidity sensing[104]. The changes in dielectric constant increased the capacitance as humidity increased. In their operation, resistive sensors are more convenient than capacitive sensors requiring more complex electronics with the risk of environmental interference[105].

CNT composite sensors a promise to deliver a combination of relatively simple fabrication procedure and achieve good sensitivity to RH. Either MWCNTs or SWCNTs has added to various substrates, such as kappa-carrageenan (KC)[106], nanoparticles[107], polyimide (PI)[108], and cellulose[109, 110]. Among the composites, CNT-cellulose sensors present a low-cost alternative[111] with high sensitivity and low weight. As a ubiquitous disposable material with porous structure[112, 113], a cellulose fiber network is well-suited for use as a humidity sensor; it offered a large surface area to combine with CNTs. Hydrophilic cellulose properties allow the use of CNT water solution to form an interactive CNT-cellulose

matrix. A CNT paper composite (CPC) treated with functional molecules allow the development of low-cost, highly sensitive and flexible humidity sensors using a relatively simple manufacturing process.

With respect to the humidity sensing, the higher sensitivity of a CPC mainly resulted from the swelling effect of both cellulose fibers and coated polymers[46, 114, 115]. In water sensing, the carrier concentration change of MWCNT induced by water molecules result in relatively small resistance change; the dominant sensing mechanism is related to the disconnection of CNT junctions by the swelling of the cellulose fibers[46]. In comparison to MWCNTs, the conductivity of cellulose fibers is negligible, even when the fibers are saturated with water[109]. As cellulose-based water sensor is immersed in water, hygroexpansion of cellulose fibers leads to disruption of conductive MWCNT networks[114]; previous studies report resistance change ratio as high as 5,500 %[116].

The swelling effect, however, is negligible for humidity sensing applications for low concertation of water molecules in the air, except for the condensation scenario. If CPC is exposed to humidity or moisture and not immersed in water, resistance changes are negligible. Previous research attempted to combine MWCNTs with cotton fibers to make a humidity sensor[110]. The swelling of the MWCNT-cotton composites increased sensitivity for RH>75%. However, the resistance change due to humidity was still much lower than that in the water immersion[117]. For MWCNTs drawn on paper, the sensing region was created by the formation of MWCNTs-cellulose fiber matrix[118]. According to our observation, the paper substrate enhanced the adsorption of water, but the swelling

effect was not noticeable in humidity sensing. Relatively fewer water molecules in a humid environment limited the change of cellulose dimensions. Compared to water immersion sensing, the disconnection of CNT junctions was significantly reduced in humidity sensing. Surface treatment of CNTs to enhance termination of CNT junctions in humidity sensing may improve the sensitivity.

In this chapter, a CPC is treated with PAA to improve the sensitivity to RH based on the swelling properties of PAA. The sensitivity of a PAA-coated CPC is compared to those of the CPCs coated with acid and Nafion. The sensitivity, hysteresis, and repeatability are characterized for a PAA-coated CPC. RH and temperature changes are measured on a simulated skin model. The high sensitivity, dynamic range, and flexibility of a PAA-CPC sensor will facilitate the development of wearable humidity and sweat sensors.

4.2 Fabrication process

MWCNTs with a 10 nm-diameter were purchased from Nanostructured & Amorphous Materials, Inc., (U.S.). Single-ply tissue paper was used as a substrate (Kimwipes, U.S.). CPC coating materials - Nafion and PAA were purchased from Sigma-Aldrich. Standard pH 4 buffer (Omega Engineering, Inc, U.S.) was used as acid treatment. Since cellulose fibers could be dissolved in high acidic solution, pH 4 solution was used. Silver paste purchased from MG Chemicals was used for electrical connection. All chemicals were used as received without any further treatment unless otherwise specified.

An aqueous solution of MWCNTs (5 mg/mL) was prepared by mixing MWCNTs in deionized water mixed with 1% sodium dodecyl sulfate (SDS). The mixture was sonicated for 20 minutes to disperse MWCNTs. The MWCNT solution was deposited onto porous paper by a pipetting (Figure 4.1). The creping action that took place during tissue manufacturing caused the flat sheet of paper to buckle up and develop ridges and wrinkles, typically recognized as creped paper. The direction parallel to the wrinkles was defined henceforth as parallel direction. The sensor dimension was 10×3 mm^2 in a parallel direction based on the water adsorption test (Figure 4.2). The MWCNT solution was evenly distributed on the tissue paper by capillary action within the cellulose fibers. MWCNTs bound to cellulose fibers during drying. After the MWCNT deposition, the CPC was dried in an oven at 60 °C for 3 minutes to evaporate the free water from the substrate. The MWCNT deposition was repeated 10 times. In our previous study, this MWCNT deposition procedure yielded resistance values below 1 kΩ/sq[119]. To form electrodes for

electrical connections, a silver paste was applied to both ends of the paper strip and cured at 70 °C on a hot plate. CPC sensor fabrication procedure is illustrated in Figure 4.1b.

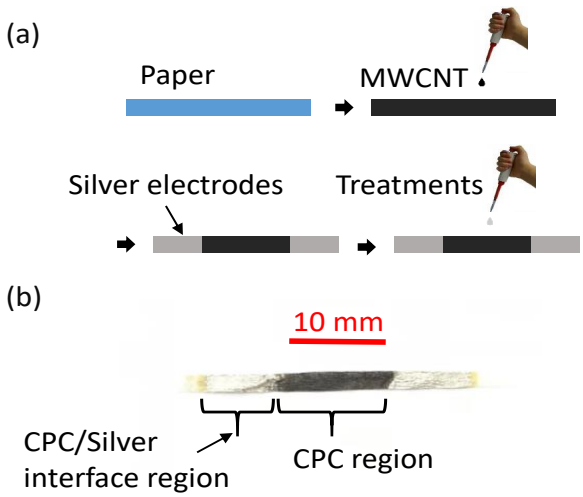

Figure 4.1 (a) Fabrication procedure of a CPC humidity sensor. (b) Photograph of a fabricated humidity sensor. Silver epoxy is used as electrodes at both ends.

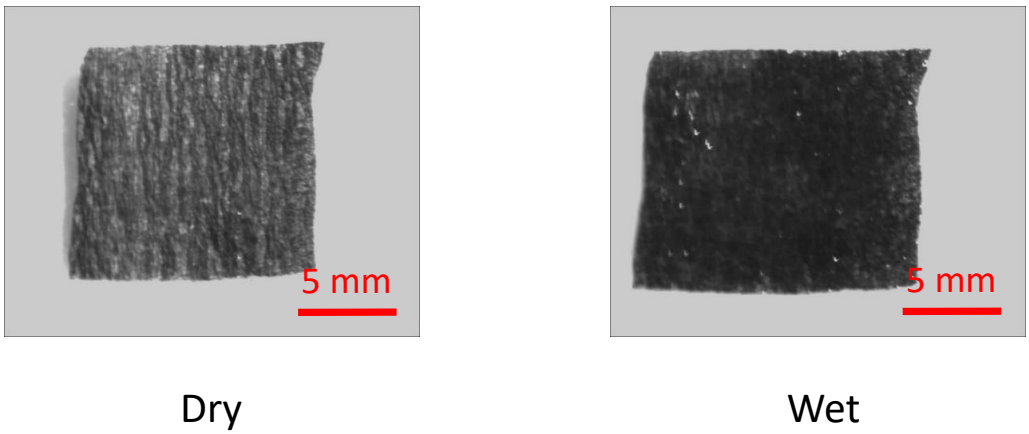

Figure 4.2 Microscope images of hygroexpansion of PAA-coated CPC specimen before and after immersion in water. The average dimensions changed from 11.9×11.4 mm2 to 14.1×12.0 mm2. The resistance changed from 986 Ω to 1766 Ω.

Three different CPC treatments were used and tested separately, (i) Nafion, (ii) PAA, and (iii) acid (pH4). Nafion was used as a nanoporous membrane to enhance proton transfer and to improve the conductivity. Nafion was diluted to 1% by deionized water. The 10 μL of 1% Nafion solution was deposited on a CPC followed by curing at 100 °C on the hot plate for 30 minutes. PAA was used to enhance the swelling effect. When PAA is exposed to water, it forms a gel-like structure with expanded volume. PAA powder was dissolved in DI water by 1% in mass and sonicated for 1 hour to create uniform dispersion. The 1% PAA solution was deposited onto a CPC followed by curing at 130 °C on a hot plate for 1 hour. The acid (pH 4) solution was deposited onto a CPC, which was cured at 100°C on a hot plate for 1 hour.

Fourier-transform infrared (FTIR) spectra of pristine paper, CPC and CPC treated with PAA were obtained using a Shimadzu FTIR spectrophotometer to characterize the binding properties of PAA, CNT, and cellulose fibers. The CPC morphology was examined by scanning electron microscopy (SEM).

The CPC morphology was studied by scanning electron microscopy (SEM). MWCNTs were bound on fibers and spanned fibers by capillary action within the porous cellulose fiber matrix (Figure 4.3a~c). The presence of PAA was confirmed by FTIR spectroscopy (Figure 4.3d) by the appearance of two characteristic peaks at around 1612 and 2915 cm^{-1}, which could be attributed to the asymmetric stretching of carboxylate groups and the C-H vibrations of acrylic acid, respectively. Furthermore, the FTIR spectra of the pristine paper exhibited a strong –OH stretching vibration band at ~3333 cm^{-1}, which gradually shifted to the lower

wavenumbers after the successive addition of MWCNT (~3325 cm^{-1}) and PAA (~3290 cm^{-1}), indicating the presence of hydrogen bonding between the hydroxyl groups in cellulose fibers and the oxygen moieties in MWCNT and PAA. These strong interfacial interactions combined with the porous structure of the cellulose fiber network with a large surface area contributed to the uniform distribution and high density of deposited MWCNTs and polymer.

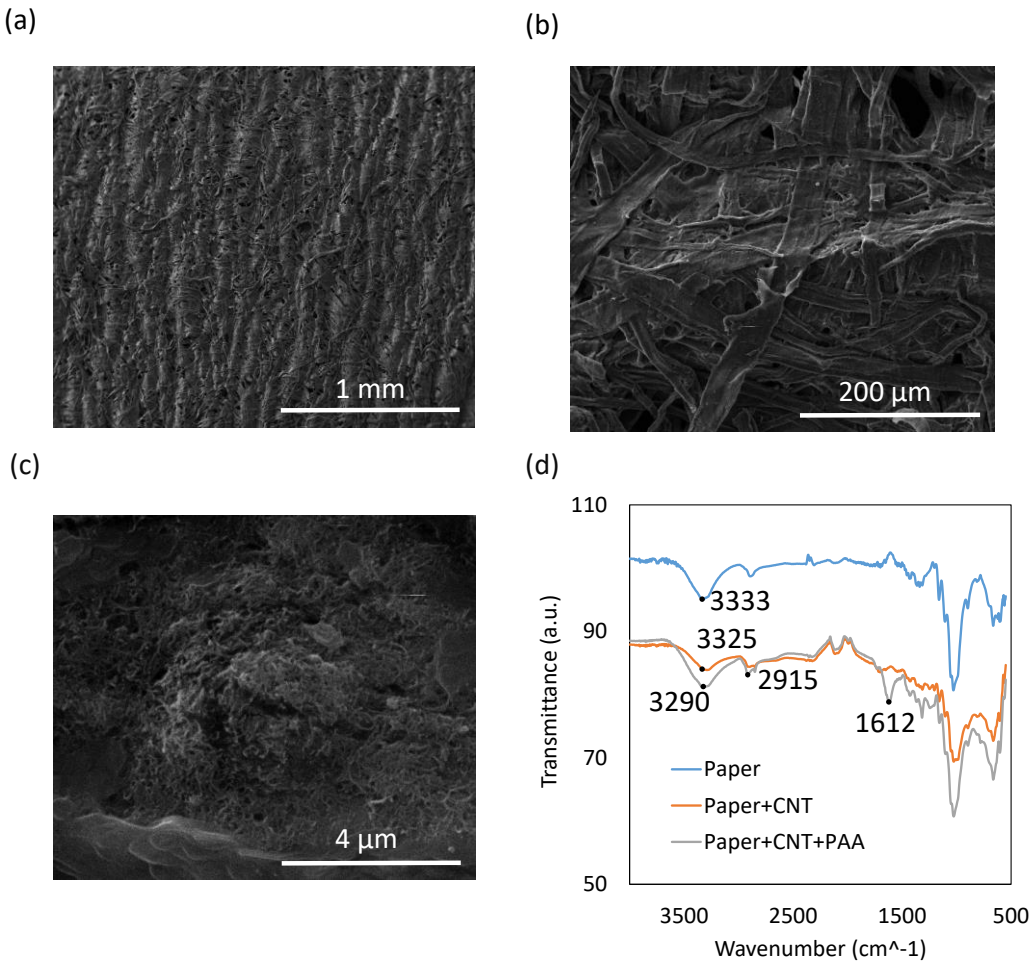

Figure 4.3 (a-c) SEM images of CPCs. (d) FTIR spectra of pristine paper, CPC, and CPC treated with PAA.

4.3 Humidity sensing

The sensitivity to humidity was characterized using a humidity chamber (0.3 m^3)[120, 121]. The experimental setup is shown in Figure 4.4. The sensitivity of the sensor is defined by the following equation:

$$S = \frac{(\frac{\Delta R}{R_0})}{\Delta(\%RH)} \tag{4.1}$$

where $(\%RH)$ is relative humidity, $(\frac{\Delta R}{R_0}) = \frac{R_{i+1}-R_i}{R_0}$, $\Delta(\%RH) = \%RH_{i+1} - \%RH_i$, where R_0 is the initial resistance of the sensor, R_i and R_{i+1} are the resistances at different acquisition times, i.e., samples i and i+1 (i: integers), $\%RH_i$ and $\%RH_{i+1}$ are the relative humidity measurements i and i+1. The controlled RH conditions were created in the environmental test chamber by the close-loop control system using a hygrometer, humidifier, and zero-air purging system. A reference sensor (Aosong electronic company, AM2301, China) was used to measure the temperature and humidity in the chamber. The resistance change of a CPC humidity sensor was acquired using an Arduino board (UNO REV3, China).

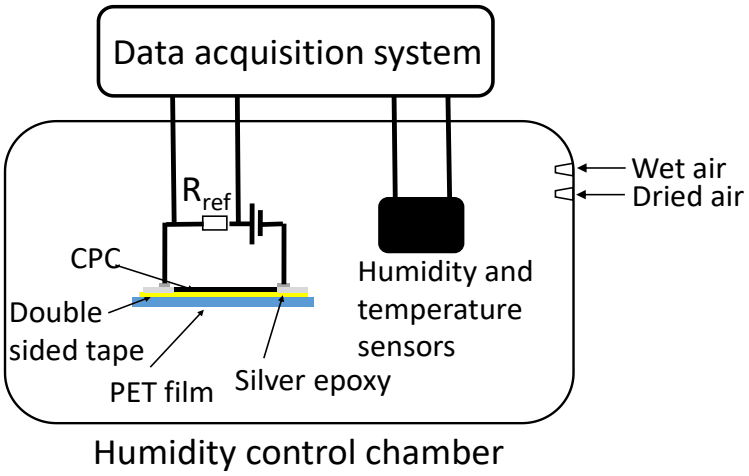

Figure 4.4 Experimental setup of a humidity test.

The hysteresis of the CPC humidity sensor was characterized by cycling RH level between 30 and 95%. The thermal effect on the removal of hysteresis was examined by heating the CPC humidity sensor on a hot plate to 110 °C after the exposure to 95% humidity. The resistance change was measured every 5 minutes until the resistance was recovered to an original value.

To study the contribution of the signal change in the CPC sensing region and CPC-silver interface (refer to Figure 4.1b), each region of a CPC sensor was isolated using Scotch tape. Cyclic humidity tests were performed for both sensors in the humidity chamber.

To calibrate the humidity sensor and obtain the empirical correlation for the sensor response, four PAA-CPC humidity sensors were fabricated. The sensors were placed in the environmental chamber where RH levels were cycled four times between 30 and 95%.

The sensitivity of pristine CPC without coating and CPC coated with Nafion, acid, and PAA were characterized in an environmental chamber for the range RH=30~95%. For RH from 10~30%, the resistance change of the specimen is shown in the supplementary information (Figure 4.5). The temperature was maintained at 25 °C unless otherwise specified. The response profiles in Figure 4.6a showed that the normalized resistance first increased monotonically with relative humidity and then increased exponentially beyond a certain humidity value. This transition in sensitivity and sensing mechanism occurred at RH level of 90, 77, 82, and 51% for untreated, Nafion, acid, and PAA treated sensors, respectively. The sensing mechanism transition threshold was defined when the linear trend observed at

RH=30% deviated by 10%, as the RH increased. When the relative humidity is greater than the critical RH, the sensor response increased rapidly, indicating a change in the sensing mechanism. Below the critical RH levels, the resistance change was dominated by the compensation of the carriers by water molecules within MWCNT[109]. The concentration of holes in CNTs was reduced by the adsorbed water molecules due to electrostatic interactions between water molecules and MWCNTs. However, the MWCNTs having a low specific surface show a limited electrostatic effect and thus exhibited a relatively low sensitivity to the humidity. In comparison to the MWCNT-paper sensors, an SWCNT sensor showed greater sensitivity for RH<75%. However, the trend was reversed for RH>75%[109].

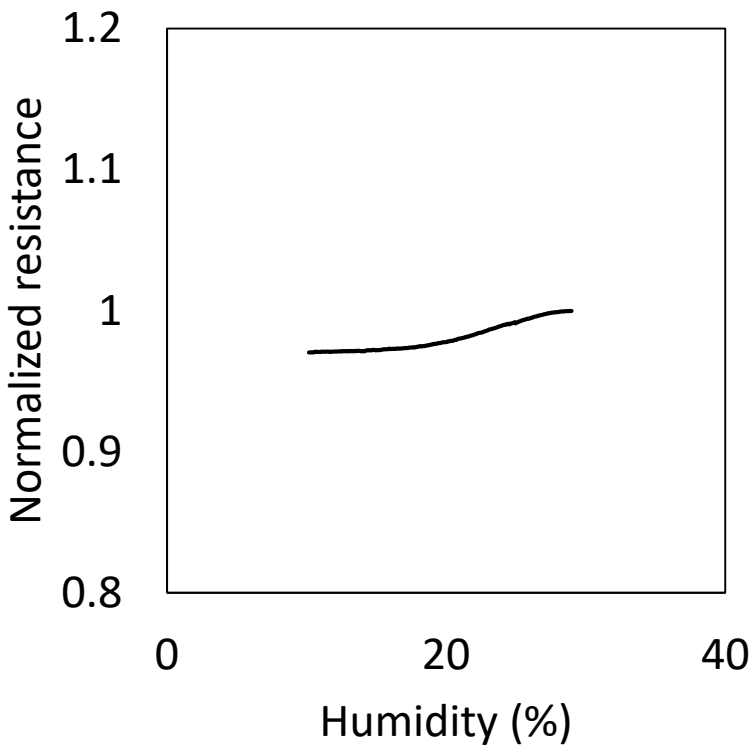

Figure 4.5 Humidity test results for PAA treated CPC for RH 10~30%. The sensor is placed on a hot plate at 40°C to lower RH.

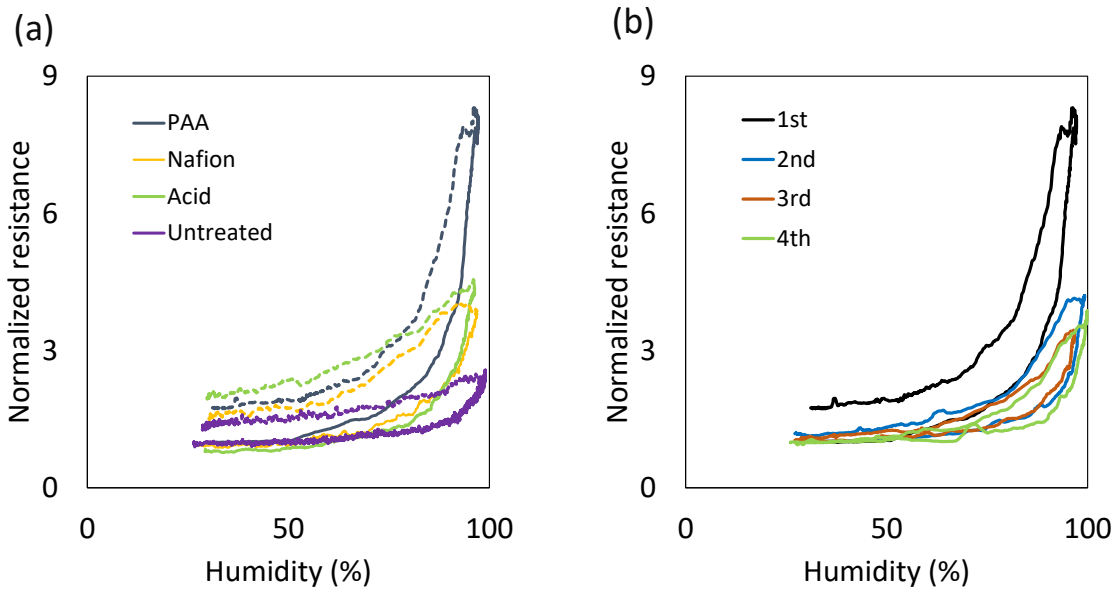

Figure 4.6 (a) Humidity test results for untreated CPC and CPC treated with Nafion, acid, and PAA. The normalized resistance change is described by solid and dotted lines for increasing and decreasing humidity. (b) Resistance change with a cyclic humidity test for a PAA-coated CPC.

At the levels above the critical humidity values, the CPC response is dominated by the reduction in the number of electrical MWCNT junctions caused by cellulose swelling. This observation is consistent with previously reported water sensing mechanism where cellulose substrate have been used[116]. Compared to other CPC detectors[109, 118], we observed a greater CPC response because the loose fiber network in creped tissue provides a greater volume for water absorption than a planar sheet paper where the cellulose fibers were bonded closely together. The increased water penetration within the CPC network promoted cellulose hygroexpansion reducing the number of electrical connections between MWCNTs, hence decreasing conductivity of the matrix.

Among the treated CPCs, the highest sensitivity was observed when PAA-coating was used. In comparison to an untreated CPC, the normalized resistance of a PAA-coated CPC increased by a factor of 3.3. Acid and Nafion coated CPCs also

showed enhanced sensitivities compared to untreated CPC by a factor of 2 and 2.2, respectively. The highest sensitivity improvement observed for the PAA-CPC could be attributed to the multistage swelling effect, with both PAA and cellulose fibers swelling upon contact with water molecules. The combined hygroexpansion of PAA and cellulose fibers provided a synergistic effect, which greatly increased sensitivity.

When a 10 μL-water drop was supplied to a CPC, the resistance increase was correlated to the CPC expansion observed by optical microscopy (Figure 4.2). This result was consistent with the previously reported swelling behaviour of PAA in water [122]. The CPC sensitivity increased to a lesser extent after treatment with acid and Nafion. The sensitivity enhancement of acid-treated CPC was caused by increased defects of cellulose fibers and MWCNTs. Nafion also swelled when exposed to a humid environment for Nafion-CPC[123]. However, the swelling was less than that of the PAA-treated CPC. Hysteresis in sensor response was observed for all CPC samples during cyclic humidity tests. PAA-coated CPC showed the greatest increase in resistance after the first humidity cycle, which was 1.7 times greater than the initial resistance. After the exposure to multiple humidity cycles, the CPC sensor response became reproducible though with a lower sensitivity compared to the first cycle (Figure 4.6b). The sensor response stabilized after three cycles, and the hysteresis behavior reduced significantly exhibiting reliable performance. The results for a cyclic humidity test and the comparison to the commercial sensor (AM2301, Aosong) are shown in Figure 4.7. This phenomenon could be attributed to the fact that paper expands to a lesser degree

during successive moisture uptakes than after the initial drying procedure due to the irreversible pore closures in cellulose fibers and a decrease of water holding ability at the material surface. In addition, the hysteresis effect during the first humidity cycle could be removed simply by heating the samples to 110 °C for 10 minutes on a hot plate. With such treatment, the resistance of PAA-coated CPC was completely recovered to the original value after the first exposure to high humidity (Figure 4.8).

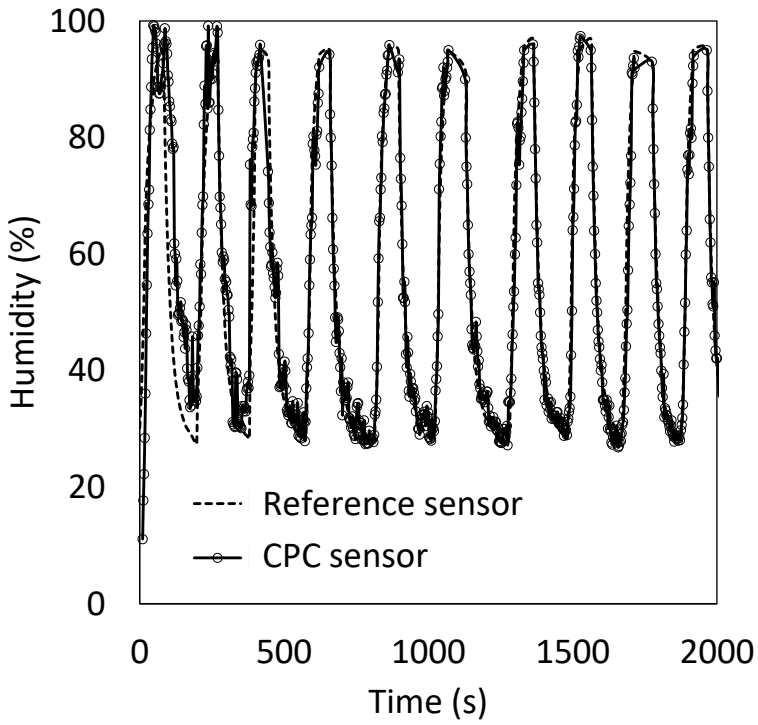

Figure 4.7 Humidity test for 10 cycles of RH between 30 and 95%. Comparison of the RH data measured from the commercial humidity sensor and the RH measured from a PAA-treated CPC humidity sensor. The resistance change of the CPC sensor was converted into the humidity using the empirical equation.

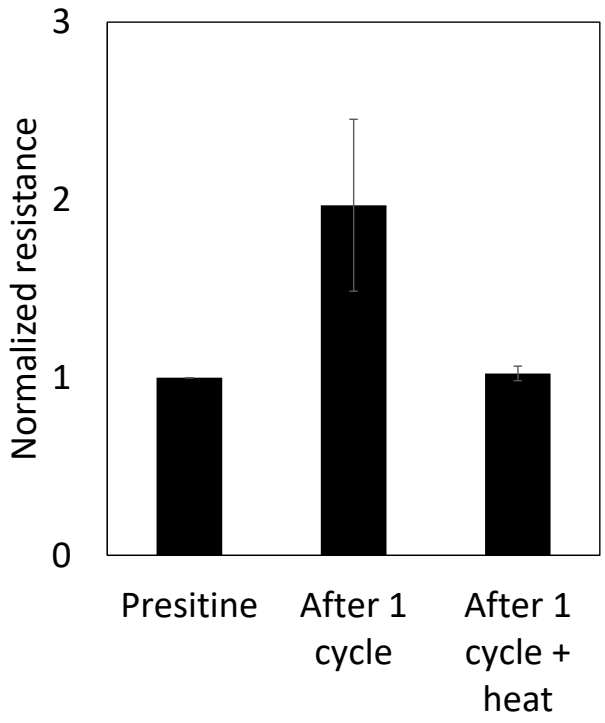

Figure 4.8 Normalized resistance change with applied heat (N=3).

The hysteresis is mainly attributed to the CPC-silver interface rather than the CPC sensing region. The total resistance of a CPC sensor is determined by the serial resistances for both CPC-silver interface and CPC regions (refer to Figure 4.1b). To evaluate the contribution of the contact resistance at the CPC-silver interface, humidity tests were performed over four cycles with each region independently isolated from the humidity exposure.

Figure 4.9 shows the isolated humidity measurement data for the CPC region and the CPC-silver interface. When a CPC region was exposed to the cyclic humidity, the hysteresis was observed only during the first cycle (Figure 4.9a). When the electrode region was exposed to cyclic humidity, the hysteresis was observed during each cycle (Figure 4.9b). The CPC-silver interface showed low

sensitivity at relative humidity below 80%, suggesting that the humidity-induced modulation of the Schottky barrier was not the dominant sensing mechanism in a CPC sensor. For *RH* >80%, the contact resistance at the electrode interface was significantly affected by the swelling effect in the CPC. Because of the high density of the CNT network on cellulose fiber, the conductivity change induced by the CPC region was more pronounced than that of the Schottky barrier effect at the CPC-silver interface.

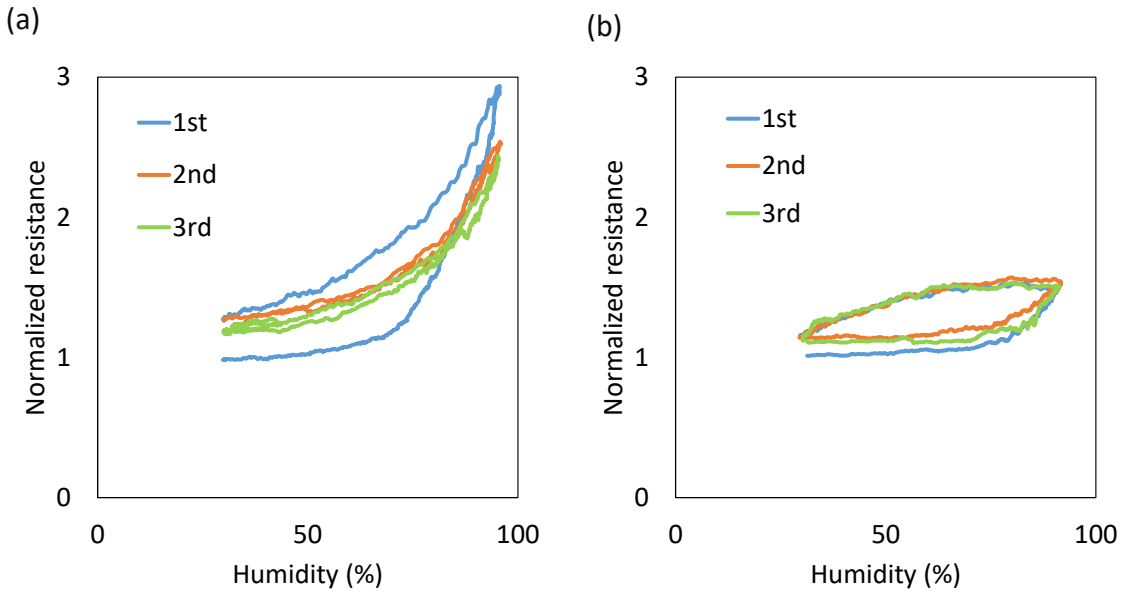

Figure 4.9 Cyclic humidity test results with isolated CPC and CPC-silver regions (a) Normalized resistance change of a CPC region. (b) Normalized resistance change of a CPC-silver region.

Figure 4.10a shows the calibration results for four RH sensors exposed to the humid environment after the running-in-period for the first three cycles. An empirical correlation was obtained by curve fitting the profiles for the increasing RH levels. When the CPC-silver interface was sealed, the normalized resistance change was reduced by 28%, and the hysteresis decreased by 21%. This indicates that

sealing the CPC-silver interface could reduce the hysteresis but at the cost of the sensitivity. To achieve higher sensitivity, both CPC-silver and CPC regions should be exposed to humidity. The calibration for both CPC-silver interface and CPC region is presented in the supplementary information (Figure 4.11).

Using four PAA-CPC samples, an empirical correlation was obtained from the cyclic humidity tests:

$$RH = 0.361x^5 - 6.8147x^4 + 49.797x^3 - 176.65x^2 + 308.22x - 124.07 \quad (4.2)$$

where x is the normalized resistance.

Figure 4.10b shows the comparison between the RH data measured from the reference humidity sensor and the RH based on the resistance of a CPC humidity sensor using the empirical equation (4.2). The response time of the sensor lagged by 8.0 +/-1.6 seconds in comparison to a commercial sensor as shown in Figure 4.12. The results for the CPC-silver and individual CPC regions are presented (Figure 4.13). The CPC region was in a good agreement with the reference sensor after the first humidity cycle, while the CPC-silver region exhibited a delay in comparison to the reference sensor. The combined PAA-CPC sensor response was consistent with the reference sensor. For measurement obtained after the initial running-in-period, the signal became repeatable and within 3% of the reference data, which agrees with the results presented in Figure 4.6b.

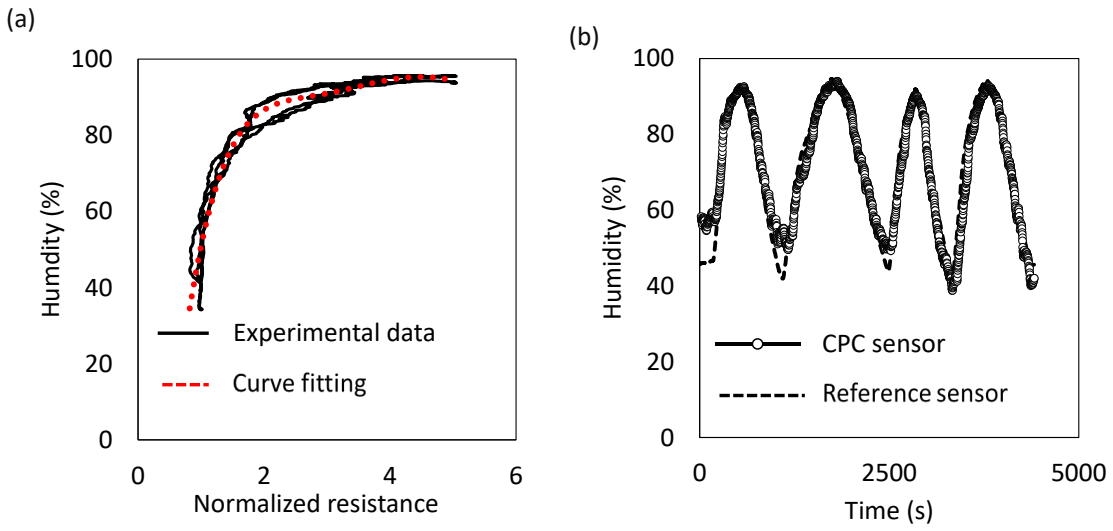

Figure 4.10 (a) Calibration curve and a fitted curve (dotted) of a CPC humidity sensor. (b) Humidity change measured by a CPC humidity sensor in comparison to a commercial humidity sensor (AM2301, Aosong).

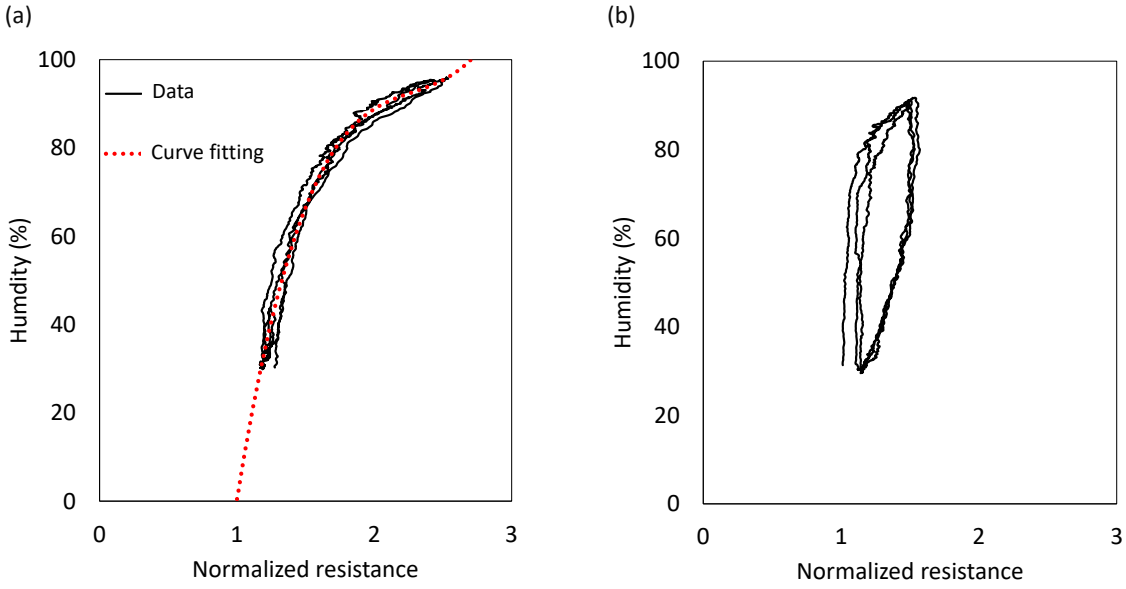

Figure 4.11 (a) Humidity test and curve fitting result of a CPC humidity sensor where only a CPC part is exposed to humidity. (b) Humidity test for a CPC humidity sensor where only the interface between the silver electrodes and CNTs is exposed to humidity.

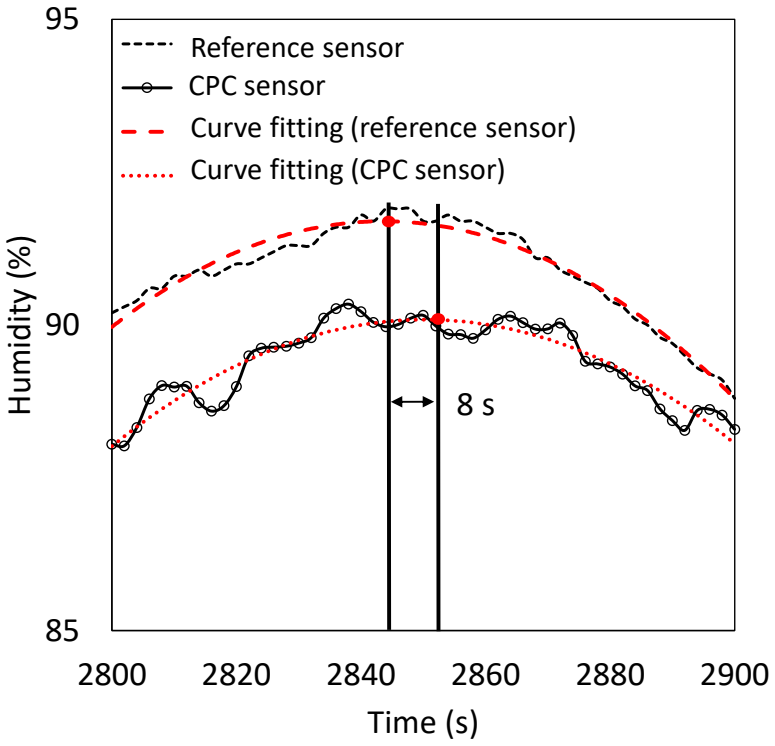

Figure 4.12 Response time of the sensor to humidity changes. The response time of the CPC sensor is compared to the commercial sensor during the humidity variation; the sensor response is ~8.0+/-1.6 seconds based on responses of 6 RH cycles after stablization.

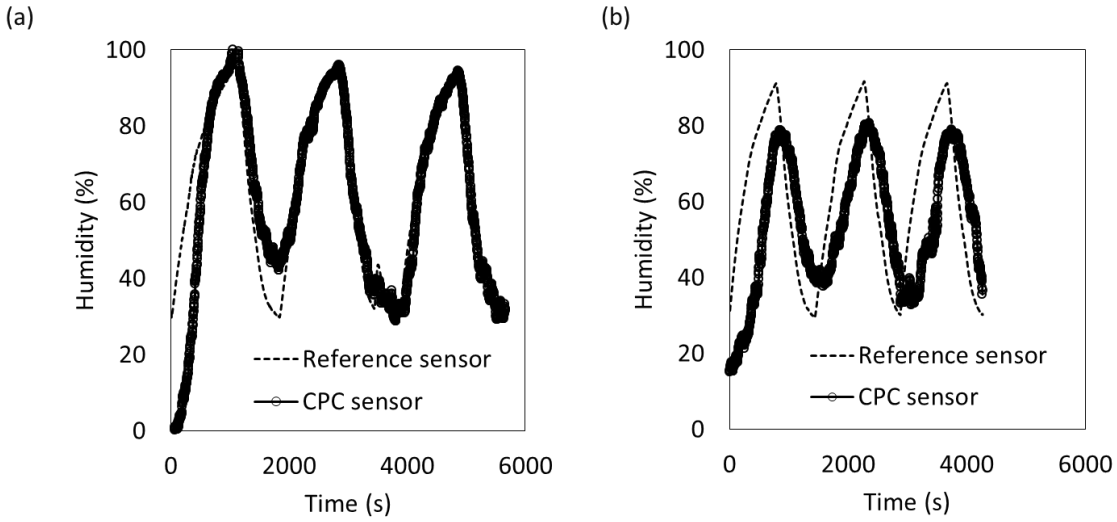

Figure 4.13 Comparison of the commercial humidity sensor with a PAA-coated CPC sensor. (a) Humidity measurement of a CPC region in comparison to a reference sensor (b) Humidity measurement of a CPC/silver interface region in comparison to a reference sensor.

4.4 Sweat sensing

To test a CPC sensor for surface moisture/sweat monitoring, a simulated setup was fabricated consisting of wet tissue paper and a hot plate (Figure 4.14). Water drops were supplied on the paper as a moisture source on a hot plate. For temperature calibration, a CPC reference temperature sensor was added to the PAA-CPC sensor. Both sensors were located above a dry region on a hot plate at 50 °C. The CPC reference temperature sensor was sealed with Scotch tape to avoid resistance change due to moisture. A commercial reference sensor measuring both humidity and temperature was placed next to both CPC sensors for calibration. In the calibration, water drops of 50, 100, and 200 µL were sequentially dispensed on the tissue paper on the hot plate. The dispensing locations of water drops were kept consistent between the CPC sweat sensors and the reference sensor. The RH measurements of the CPC sensor were compared to that of a commercial sensor during the water drop evaporation (Figure 4.15).

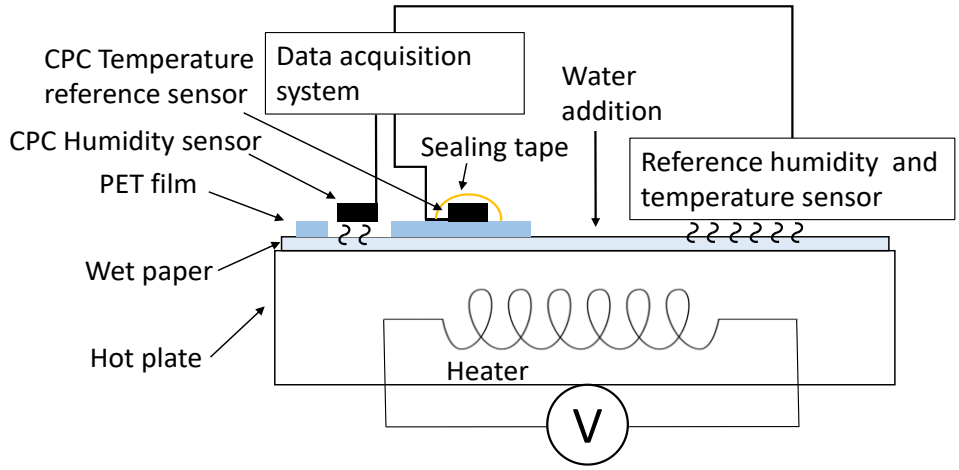

Figure 4.14 Experimental setup for a simulated moisture/sweat sensor.

A CPC sensor could be used to estimate the water evaporation rate for use in sweat sensing application. When a CPC sensor was exposed to different water volumes of 50, 100 and 200 μL, the humidity level changed, which was also monitored by using a commercial reference sensor (Figure 4.15). The data from the CPC sensor were corrected for temperature variations, measured by a second CPC sensor shielded from interaction with moisture using sealing tape. A temperature calibration curve is given in Figure 4.16. The data from the commercial RH sensor (AM2301, Aosong), also compensated for temperature variation, were used as a reference. As the water volume increased from 50 to 200 μL, the CPC sensor was able to quantitatively track the surface moisture levels. The experimental data are in good agreement with the reference RH sensor. The discrepancies in the peak width are likely to be attributed to slight variations in the water evaporation conditions based on the sensor placement. The sensor output as a function of water droplet size was also tested by depositing small water volumes of 0.5~20 μL (Figure 4.17). With respect to the volume of liquid water deposition, the resolution of the sensor measurements was ~ 0.5 μL.

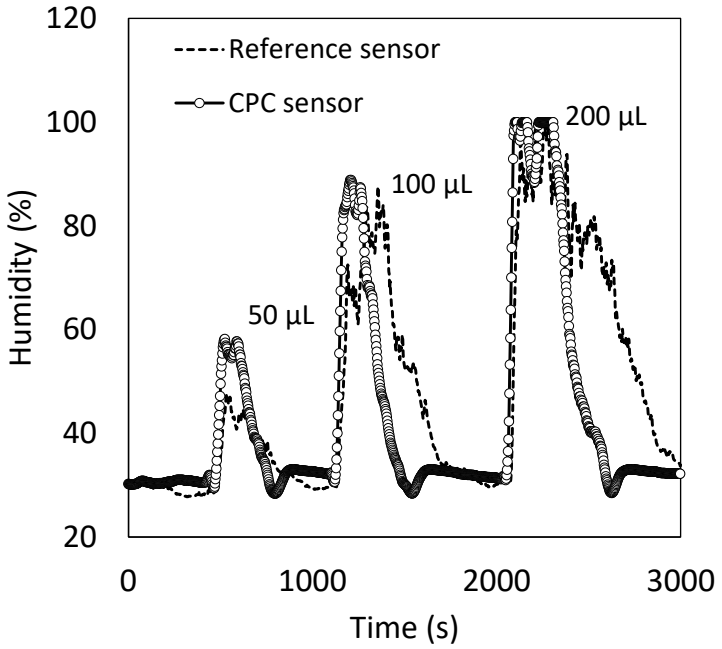

Figure 4.15 Humidity measurement for a simulated sweat using a CPC humidity sensor in comparison to a commercial sensor; reference humidity sensor and CPC sweat sensor with different applied water amount.

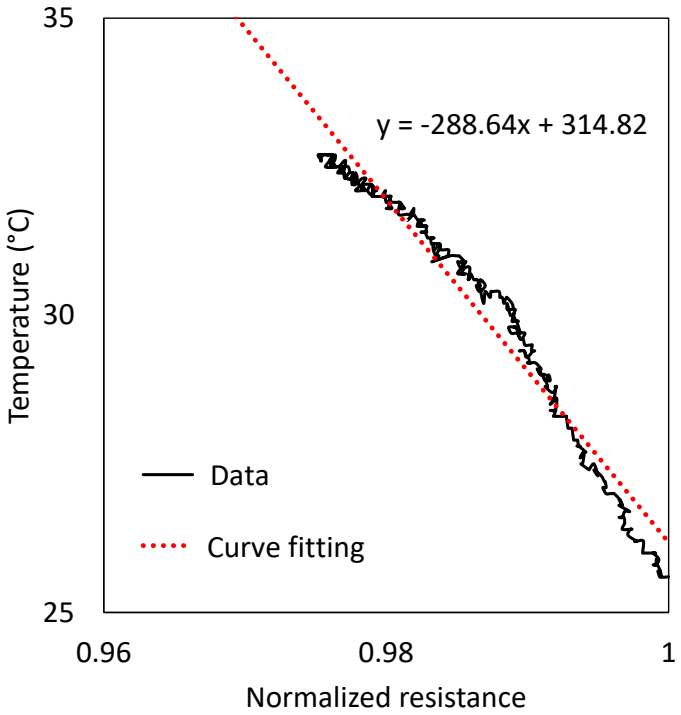

Figure 4.16 Temperature calibration curve of a CPC sensor.

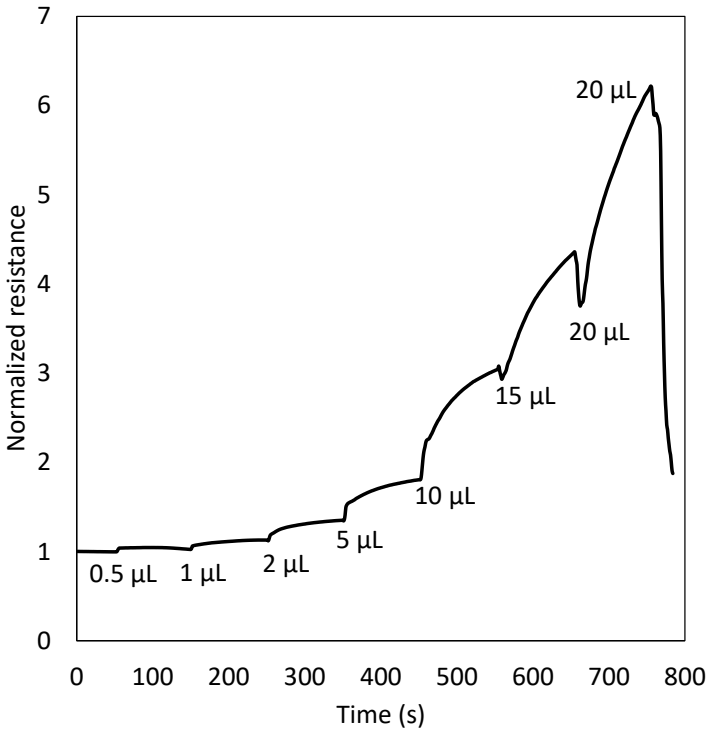

Figure 4.17 Detection of small quantities of water ~ 0.5 - 20 µL with a PAA-treated CPC sensor.

4.5 Discussion

PAA treatment of the CPC matrix enhanced the performance of a CPC RH sensor. At the critical RH values, the sensing mechanism was changed from electrostatic interaction on MWCNTs for $RH<RH_{cr}$ to disruption of electrical connections of MWCNTs between PAA and cellulose fibers swelling for $RH>RH_{cr}$. A PAA-coated CPC showed an increased response (by factor 3.3) compared to an untreated CPC. The PAA addition rendered RH_{cr} earlier due to induced hygroexpansion of PAA. In previous research, acid was applied to CNTs to create oxidization of CNTs to increase the interaction between water and CNT surface[124]. In our study, neither nitric acid nor sulfuric acid was suitable because of damage to the cellulose fibers. Instead, a buffer solution of pH4 was applied to create defects such as dangling bonds and vacancy on the CNT surface. Acid-treated CPC sensor showed sensitivity improvement at high humidity (RH > 75%) compared to untreated CPC. When exposed to water, both Nafion and PAA showed swelling [125, 126]. The swelling of Nafion and PAA resulted in further deformation of the CPC network to disrupt more CNT junctions, which further increased the resistance.

Comparing all treated and untreated CPC humidity sensors, the PAA-treated samples showed the best sensitivity. The humidity-induced swelling ratio of PAA was greater than Nafion resulting in greater sensitivity at high RH levels. Although Nafion coated on MWCNTs resulted in enhanced sensitivity by improving the proton exchange [102], the dominant sensing mechanism in this study was shown to be the swelling-induced disjunction of the CNT network. The swelling ratio of PAA

was also affected by pH change in aqueous solutions[122]. For RH sensing, water with pH7 was used for the maximum swelling ratio of PAA. The resistance change of PAA treated CPC was also investigated for a range of pH levels (Figure 4.18). In comparison to other CNT composite humidity sensor, the CPC sensor presented in this work showed better sensitivity and greater dynamic range, as listed in Table 4.1.

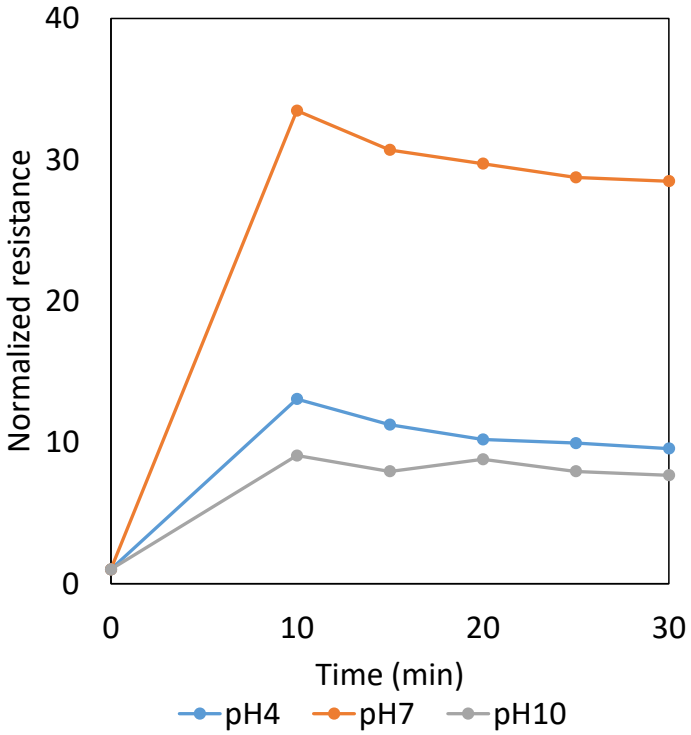

Figure 4.18 Normalized resistance of PAA-treated CPCs immersed in aqueous solutions at pH 4, 7, and 10.

Table 4.1 Comparison of sensitivities of carbon nanotube-paper composites for relative humidity (RH).

Sensing materials	Sensing mechanism	Sensitivity	Dynamic range for RH (%)
MWCNT-printer paper[118]	resistive	0.35, where sensitivity=$(\Delta I/I_0)/\Delta(\%RH)$, where ΔI is the current difference at different acquisition time. I_0 is the initial current	11-95
SWCNT-cellulose paper[109]	resistive	-0.90, where sensitivity=$(\Delta c/c_0)/\Delta(\%RH)$. Δc is the conductance difference at different acquisition time and c_0 is the initial conductance	10-75
MWCNT sheet[101]	resistive	0.75, where sensitivity=$(\Delta R/R_0)/\Delta(\%RH)$. ΔR is the resistance difference at different acquisition time. R_0 is the initial resistance	10-90
KC-MWCNT[106]	resistive	1.0, where sensitivity=$(\Delta R/R_0)/\Delta(\%RH)$. ΔR is the resistance difference at different acquisition time, and R_0 is the initial resistance	20-90
MWCNT-stainless steel[127]	capacitive	36, where sensitivity=$(\Delta C/C_0)/\Delta(\%RH)$. ΔC is the capacitance difference at different acquisition time. C_0 is the initial capacitance	50-85
chemically treated MWCNT[100]	resistive	1.3, where sensitivity=$(\Delta R/R_0)/\Delta(\%RH)$. ΔR is the resistance difference at different acquisition time. R_0 is the initial resistance	11-98
Polyimide-MWCNT[105]	resistive	0.47, where sensitivity=$(\Delta R/R_0)/\Delta(\%RH)$. ΔR is the resistance difference at different acquisition time. R_0 is the initial resistance.	10-95
Polyimide-MWCNT[108]	capacitive	0.22, where sensitivity=$(\Delta C/C_0)/\Delta(\%RH)$. ΔC is the capacitance difference at different acquisition time. C_0 is the initial capacitance.	30-90
PAA treated CPC sensor (This paper)	resistive	90, where sensitivity= $(\Delta R/R_0)/\Delta(\%RH)$. ΔR is the resistance difference at different acquisition time. R_0 is the initial resistance	10-95

Chapter 5. CNT-paper Composite Capacitive Eye Tracking Sensor

Eye tracking is essential in human computer interaction, cognitive monitoring, and biomedical applications. The widely used optical eye tracking method is limited in cost and wearing comfort. This study presents a low-cost light-weight capacitive eye tracking sensor fabricated with carbon nanotube-paper composite (CPC). The fracture-induced fabrication method is applied to CPC to produce a capacitive sensitivity. The eye movement is measured by the capacitance changes induced by the distance and permittivity change between eye ball, muscles and CPC sensors. Fabrication procedures and sensor design are optimized for best sensing performance. Finite element analysis is applied to understand the merits of the fracture induced micro-interdigitated structures of the electrodes. The sensitivity and resolutions of the CPC sensor are characterized for different movement modes of a conductive object. A numerical model is constructed to characterize the sensitivity of a simulated human eyeball. A CPC eye tracking sensor is installed on eye glasses to measure the wearer's eye ball movement. The CPC capacitive eye tracking sensor shows a high sensitivity and resolution in eye movement sensing. The small form factor and low cost make the sensor potentially ideal to current eye tracking devices.

5.1 Background

Eye tracking sensors are widely applied to wearable equipment for virtual and augmented reality (VR and AR)[128-132], disease diagnosis[133-136] and human computer interaction[137-139]. The growing number of studies in eye tracking sensors and devices has paved ways in various applications. Optical image processing is popular for

eye tracking. Optics based eye tracking systems include eyeglass-mounted cameras and desktop stations, both of which present challenges in the contexts of usability due to their size and data quality. For example, existing measures of eye movement require wearing specific monitoring hardware; hence, individuals who do not wear glasses are preferred as participants for the studies. Frequent manual calibration is required to obtain reliable data, limiting data acquisition periods. Bulky equipment significantly complicates inspection, limiting the application to cyber learning. Improvements in data processing and sensor calibration are challenging. For example, although eye blinks can be used as a digital marker, most eye-tracking systems filter out eye blinks as noise due to the difficulties in sensor calibration. The high cost of current eye-tracking systems is an additional burden to render eye monitoring accessible to patients. It has also been questioned if the assessment in laboratory settings represents the behavior in real life. The unnatural circumstances of a laboratory can significantly affect saccadic behavior, potentially leading to a false evaluation.

Various sensing methods have been attempted to develop alternatives of an optical eye tracking system. An ultrathin piezoelectric nanogenerator has been fabricated and attached on the surface of eyelid to monitor the local deformation[140]. The motion of eye ball was characterized by the output voltage/current. This self-powered ultrathin eye tracking sensor could potentially reduce the size of the devices. A magnetic eye tracking system using scleral coil has been developed based on the alternating magnetic fields on wearer's eyes. A scleral coil was inserted in wearer's eye. The voltages in the scleral coil was induced by the oscillating magnetic flux from generator coils. The magnitude of the induced voltages was determined by the angles of the scleral coils and the flux. The above

obtrusive eye tracking sensors improved the size of forms and the accuracy in eye tracking. To optimize the wearing comfort and reduce the fabrication cost, capacitive sensing in eye tracking was studied.

Capacitive sensing has been widely applied to various types of proximity sensing on monitoring wearers' activities [141, 142]. An unobtrusive sensor is more comfortable for wearable applications. The movement of human body influences the electric field of a sensor. The capacitance change of the sensor is calibrated for different human body movements. A car seat with a capacitive proximity sensor system has been developed to monitor the activity of the driver to recognize the inattentiveness. Gesture recognition has been realized by capacitive proximity sensor array [143]. The distance changes from the hand to the capacitive array induced the capacitance changes of the capacitive sensors. An apparatus with a capacitive sensor array to determine eye gaze detection was developed[144]. During the eye movement, the movement of an eyeball, muscles and eyelids can induce drastic change of their distance to a fixed point [145]. The combined distance changes can be recognized by the proximity sensor array that was installed near an eye.

The current challenges of applying capacitive proximity sensing technology to eye tracking are: (1) the fabrication cost and complexity of an array with numerous sensors in a miniature device is high. (2) sensor location is random without optimization based on the physiological structure of the eye and its movement. (3) bulky sensor design with low capacitive sensitivity and resolution limited the performance of the eye tracking sensor. Development of a new capacitive sensing material with higher sensitivity and a low cost fabrication procedure will facilitate the wearable application of a capacitive eye tracking

technology. Also, proper sensor design and placement should be applied based on the physiological structure and the movement of eyes.

In this chapter, we present an unobtrusive capacitive eye tracking sensor fabricated by carbon nanotube-paper composite (CPC). The sensitivity of the sensor is improved by fracture-induced nanoscale electrodes at the crack. Fringing fields and capacitance at the crack are enhanced by large surface areas of MWCNTs that are coated on cellulose fibers. The sensing mechanisms and characteristics of the micro electrodes are studied by finite element method (FEM) simulation. The parameters of the low-cost fabrication and fracture method are studied for optimized sensing performance. Planar and cantilever CPC eye tracking sensors are designed and characterized for different sensing scenario. The sensitivity and resolution of CPC eye tracking sensors are characterized by a scanning method. The sensing performance is characterized by using a simulated eye ball and by detecting the eyeball rotation of a wearer. As an unobtrusive sensor with light weight, a CPC eye tracking sensor can be easily installed on eyeglass frames or other head gears.

5.2 Fabrication process

Multiwalled carbon nanotubes (MWCNTs) with a 10 nm-diameter were purchased from Nanostructured & Amorphous Materials, Inc., (U.S.). Single-ply tissue paper was used as substrate (Kimwipes, U.S.). Polyurethane was purchased from Elmer's, Inc., (U.S.). Silver paste was purchased from MG Chemicals for electrical connection. All chemicals were used as received without any further treatment unless otherwise specified.

An aqueous solution of MWCNTs (5 mg/mL) was prepared by mixing MWCNTs in deionized water mixed with 1% sodium dodecyl sulfate (SDS). The mixture was sonicated for 20 minutes to disperse MWCNTs. The MWCNT solution was deposited onto porous paper by a pipetting method. The MWCNT solution was evenly distributed on the tissue paper by capillary action in the cellulose fibers. MWCNTs bounded to cellulose fibers during drying. After the MWCNT deposition, the CPC was dried in an oven at 60 °C for 3 minutes to evaporate the free water from the substrate. The MWCNT deposition was repeated to have an ideal sheet resistance of CPC, 110 to 200 kΩ/sq. In our previous study, the ideal resistance of the CPC should be: 1. higher than 110 kΩ/sq to generate electrical disconnections during the fracture procedure; 2. lower than 220 kΩ/sq to ensure an optimized sensitivity in capacitive sensing. To form electrodes for electrical connections, a silver paste was applied to both ends of the paper strip and cured at 70 °C on a hot plate. The fracture to CPC was applied and controlled with stretching stage shown in Figure 5.1. The resistance of CPC was measured simultaneously with strain in stretching. As the electrical conductivity of the CPC was terminated, the stretching was held to form the capacitance of a CPC prior to complete fracture. Polyurethane was applied to the fractured CPC, which was cured at 100 °C on hot plate for 20 min as a coating layer. CPC sensor

fabrication procedure is illustrated in Figure 5.2. By folding the sensor in the cracked region, a cantilever shaped CPC eye tracking sensor can be fabricated (Figure 5.3a). The sensor system is fabricated as illustrated in Figure 5.3b.

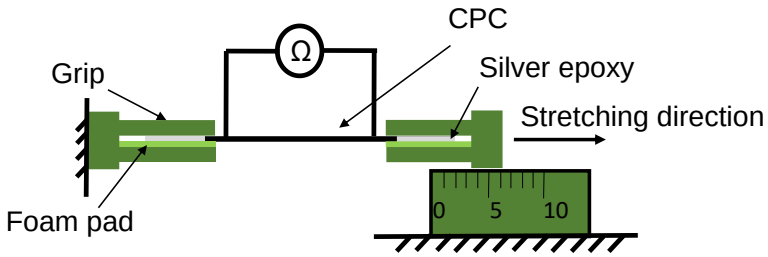

Figure 5.1 Stretching stage for CPC sensor fracture generation.

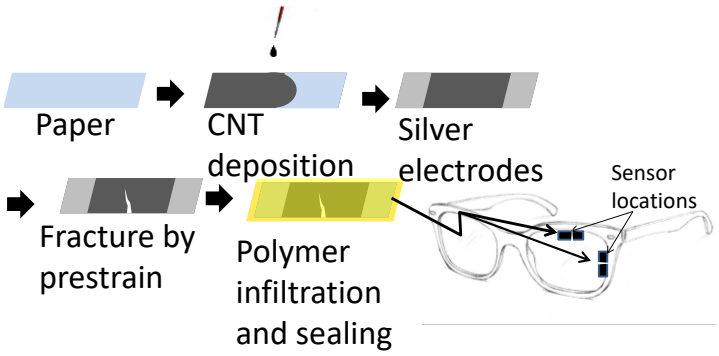

Figure 5.2 Fabrication steps of CPC eye tracking sensor

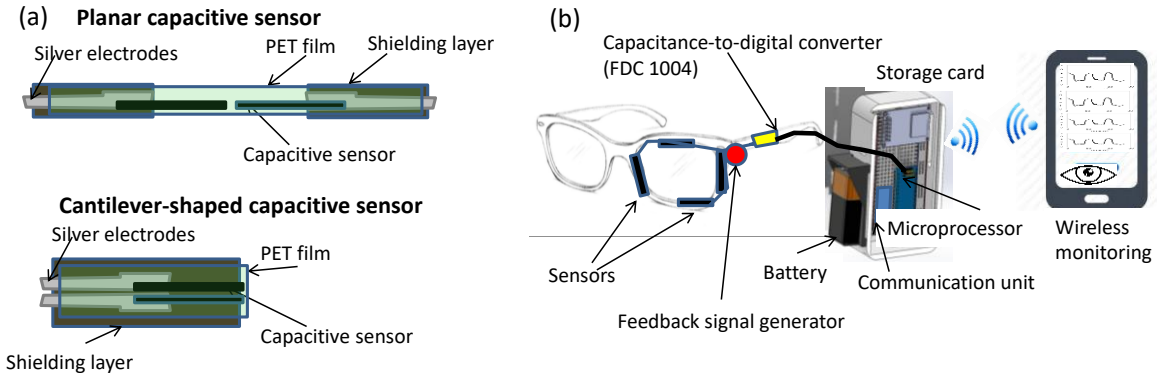

Figure 5.3 (a) Structure of planar and cantilever-shaped CPC sensors. (b) Integration of the sensors to eyeglasses sensing system.

The microscope images of fractured CPC were taken. The fracture conditions of the CPC specimen were compared and correlated with the capacitance difference. A batch of CPC sensors were fabricated with different fracture condition and initial capacitance value. The fracture condition was observed under microscope. The capacitance of each sensor was measured with capacitance meter (GLK Instruments, U.S.).

A CPC eye tracking sensor is shown in Figure 5.4a. A standard sensor fabrication procedure was established. 20 CPC eye tracking sensors out of 22 were working properly with expected sensing performance (Figure 5.4b). The yield was 91%.

(a)

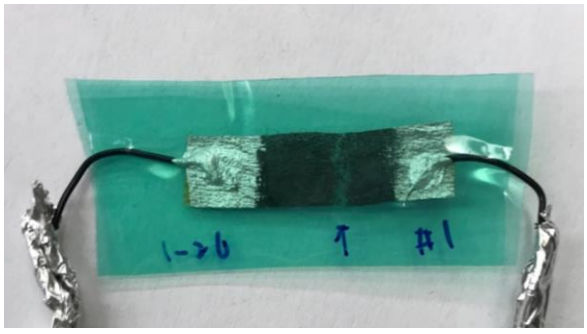

(b)

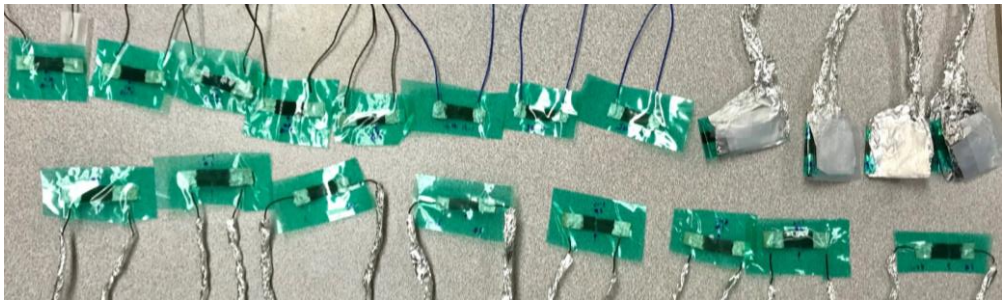

Figure 5.4 (a) Picture of CPC eye tracking sensor. (b) 20 fabricated CPC eye tracking sensors that can work properly. The folded sensor is a cantilever-shaped sensor.

5.3 FEA of fractured CPC electrodes

The capacitance and electric field of CPC sensors were studied by finite element analysis (FEA) models using simulation software COMSOL. The numerical models of the electrodes were constructed based on the fractured CPC matrix structure and the planar plate electrodes. The fractured CPC matrix creates numerous interdigitated electrodes with high aspect ratios. A smaller dimension at the tip of the electrodes will induce higher electric fields in comparison to planar plate electrodes. To study the enhancement of an electric field by the interdigitated electrodes, 3D models were used for the electrode modeling. The configurations of planar plate electrodes and five pairs of interdigitated electrodes are shown in Figure 5.5. The dimensions of the cross section of the planar electrodes were 5×50 μm^2. The length of the electrodes was 200 μm and the separation distance between the electrodes was 100 μm. The cross section of the planar electrodes were equivalent to the combined facing area of five pairs of interdigitated electrodes. Each of the five pairs of interdigitated electrodes had a cross section dimension of 5×10 μm^2. The length of the electrodes and the separation distance between the electrodes were also 200 and 100 μm, respectively. The electrode material was MWCNT, with dielectric constant of 10^3 and electrical conductivity of 10 S/m [146]. The dielectric material was air, with relative dielectric constant of 1 and electrical conductivity of 10^{-14} S/m [147]. The potentials on surface of both terminals were 0V as the initial condition. The potentials on surface of terminals were DC 2.4V and 0V as the boundary condition in the simulation, which was the measurement voltage applied by the capacitance-to-digital converter FDC1004 evaluation module (Texas Instrument, U.S.). Physics-controlled mesh sequence type was selected. 3D tetrahedral and triangular elements were used for capacitance

analysis. The electric fields and capacitance of planar plate electrodes and interdigitated electrodes were compared by the simulation results.

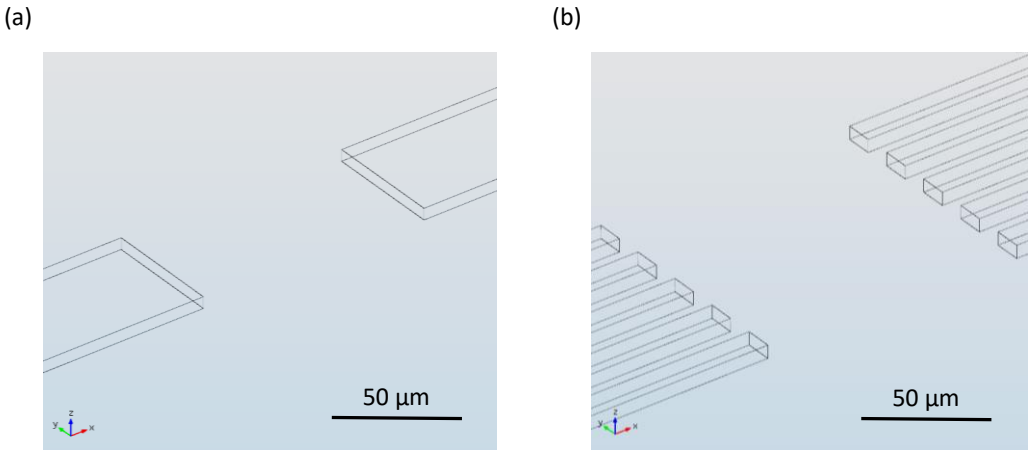

Figure 5.5 (a) planar plate electrodes. (b) interdigitated electrodes.

The effects of aspect ratio (*AR*) and separation aspect ratio (AR_s) to the capacitance were also studied with configurations shown in Figure 5.6, where $AR = \frac{L}{D}$, $AR_s = \frac{d}{D}$, D is the diameter of the parallel electrodes, L is the thickness of the electrode, and d is the separation distance of the electrodes. Axisymmetric models were used. To investigate the influence of *AR* to fringing capacitance, AR_s and L were controlled to be 10 and 1 mm, respectively. To investigate the effect of AR_s to fringing capacitance, *AR* and d were controlled to be 10 and 100 µm, respectively. The dielectric material and electrode material were the same as previous settings. The potentials on surface of both terminals were 0V as the initial condition. The potentials on surface of terminals were DC 2.4V and 0V as the boundary condition in the simulation. Physics-controlled mesh sequence type was selected, and a 2D triangular element was used for capacitance analysis. When D increased from 10 µm to 10 mm, the nominal capacitance of a parallel plate capacitor was computed and compared with the capacitance of modified capacitors with different *AR* and AR_s of

electrode configuration from FEA simulation results. The effects of relative dimensions of the electrode diameter, length and separation distance to the fringing effect were studied by FEA simulation.

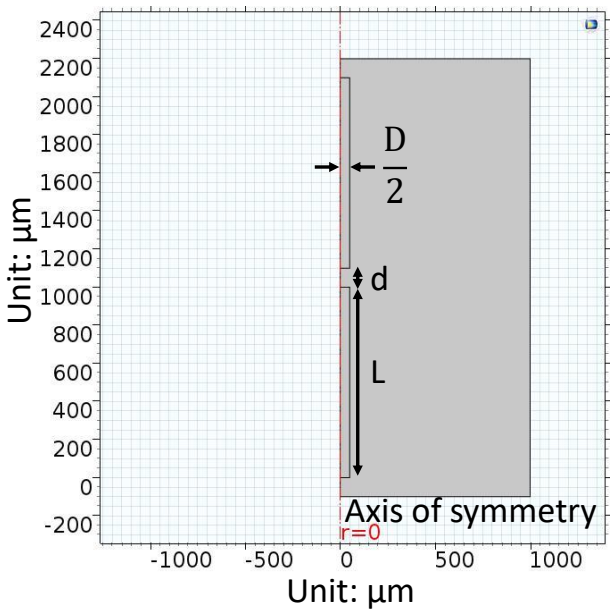

Figure 5.6 FEA axisymmetric model of capacitor electrodes.

The capacitive eye tracking of CPC is based on the change of a fringing capacitance during eye movement. The sensing mechanism of the CPC capacitive sensor is presented in Figure 5.7a. After the fracture of CPC, MWCNTs coated on cellulose fibers formed capacitive electrodes at the crack. Charges were accumulated at the tips of the MWCNTs, which will induce large electric fields. The fringing electric fields formed between electrodes. As an eyeball approached to MWCNT electrodes, the permittivity between the electrodes was increased, and the electric fields were enhanced. The capacitance was increased. According to our previous research, the fracture of CPC structure reorganized the CPC to form numerous nanoscale interdigitated electrodes[119]. The electric field distribution due to different forms of electrodes is shown in Figure 5.7b-c. The electric

fields between the electrodes with interdigitated structure had larger electric fields than those between planar plate electrodes because of a higher charge density at the "sharper" ends (higher *AR*) of interdigitated electrodes. The higher charge density induced a higher electric field. The sensing performance of CPC capacitive sensor was determined by the magnitude of the fringing field and the capacitance value.

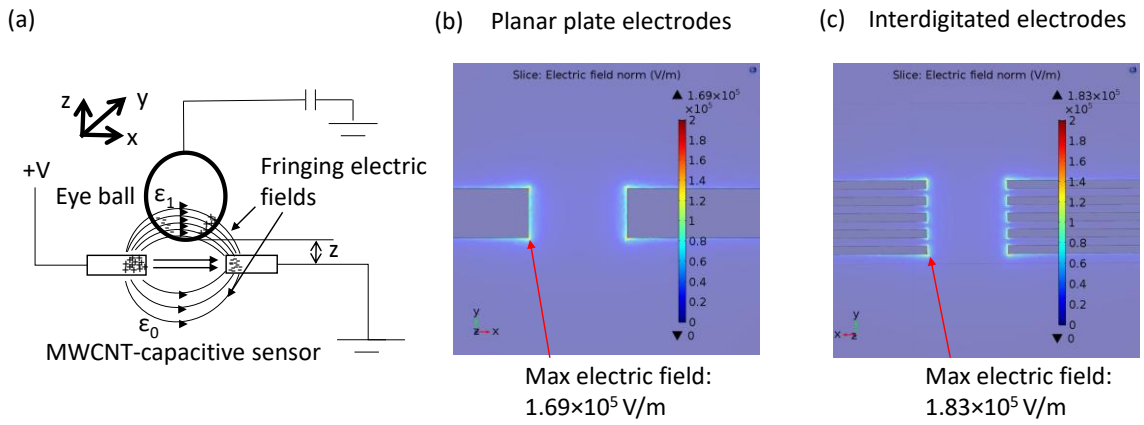

Figure 5.7 (a) Working principle of CPC capacitive sensing. (b) Electric field of planar plate electrodes. (c) Electric field of interdigitated electrodes.

The dimensions and the aspect ratios of the MWCNTs electrodes were critical parameters to the improvement of the sensor performance by enhancing the fringing capacitance. Selected FEA results of capacitance for different *AR* and AR_s are shown in Figure 5.8. Figure 5.8a-b shows the capacitance difference of models with same AR_s and different *AR*. Figure 5.8c-d shows the capacitance difference of models with same *AR* and different AR_s. For a parallel plate capacitor, the capacitance was dominated by the direct capacitance between the electrodes with negating the fringing capacitance. The nominal capacitance of parallel plate capacitor could be calculated using the following equation:

$$C_{parallel} = \frac{\varepsilon_0 \varepsilon_r A}{d} \tag{5.1}$$

where ε_0 is the permittivity of free space, ε_r is the relative permittivity of the dielectric medium between the electrodes, *A* is area of the plates, and *d* is the distance between the two plates. Equation (5.1) is applied to a parallel plate capacitor, for which the following conditions are satisfied: (1) AR <<1; (2) AR_s <<1. When both *AR* and AR_s are larger, fringing electric fields become more dominant than direct electric fields between the facing electrodes. The modified capacitance considering the fringing effect is described in equation (5.2):

$$C_{mod} = \frac{\alpha \varepsilon_0 \varepsilon_r A}{d} \quad (5.2)$$

where α is the fringing effect factor. The value of α was determined by *AR* and AR_s and was calculated by: $\alpha = \frac{C_{mod}}{C_{parallel}}$ (Figure 5.9). The capacitance of parallel plate capacitor and the modified capacitor with different D are shown in Figure 5.9a. The fringing effect factor at different *AR* is shown in Figure 5.9b. When AR_s was 10, a modified capacitor showed much larger capacitance than a parallel plate capacitor. When $AR >> 1$, α was consistent and equals to 138 as *D* increased. When D and L were on the same order ($0.1<AR<10$), α was reduced and became 30 at $AR=0.1$. A large α showed the significant enhancement of the capacitance from the fringing effect, but further increment of *AR* would cause the saturation of α, because the effective length for charge accumulation on the edge of the electrodes did not increase with the electrode length. When the electrode length was larger than the effective charge accumulation length, the contribution of longer electrodes to the fringing electric field was negligible. Large *AR* defined the shape difference of the electrodes from parallel plate capacitor electrodes, which determined that the fringing capacitance, instead of the direct capacitance of a parallel plate capacitor, was dominant to

the total capacitance of the capacitor. The capacitance of parallel plate capacitor and the modified capacitor with different D are shown in Figure 5.9c. The fringing effect factor at different AR_s is shown in Figure 5.9d. When AR was 10, α increased with AR_s. A modified capacitor had larger capacitance than a parallel plate capacitor when AR_s>0.01. α started to saturate at AR_s =100. When AR_s<0.1, the fringing capacitance was not obvious and became negligible when AR_s=0.01. In order to obtain relatively large fringing capacitance, AR_s should be large enough to maintain a relatively large separation distance between electrodes, but further increase of AR_s would cause the saturation of α. When the separation distance was too large, the charge accumulation on the edge of the electrodes was very small. The ratio of direct electric field and fringing electric field induced by the charge accumulation was stabilized after AR_s>10^3 (Figure 5.9d), therefore, further increment of separation distance would not increase α at this stage.

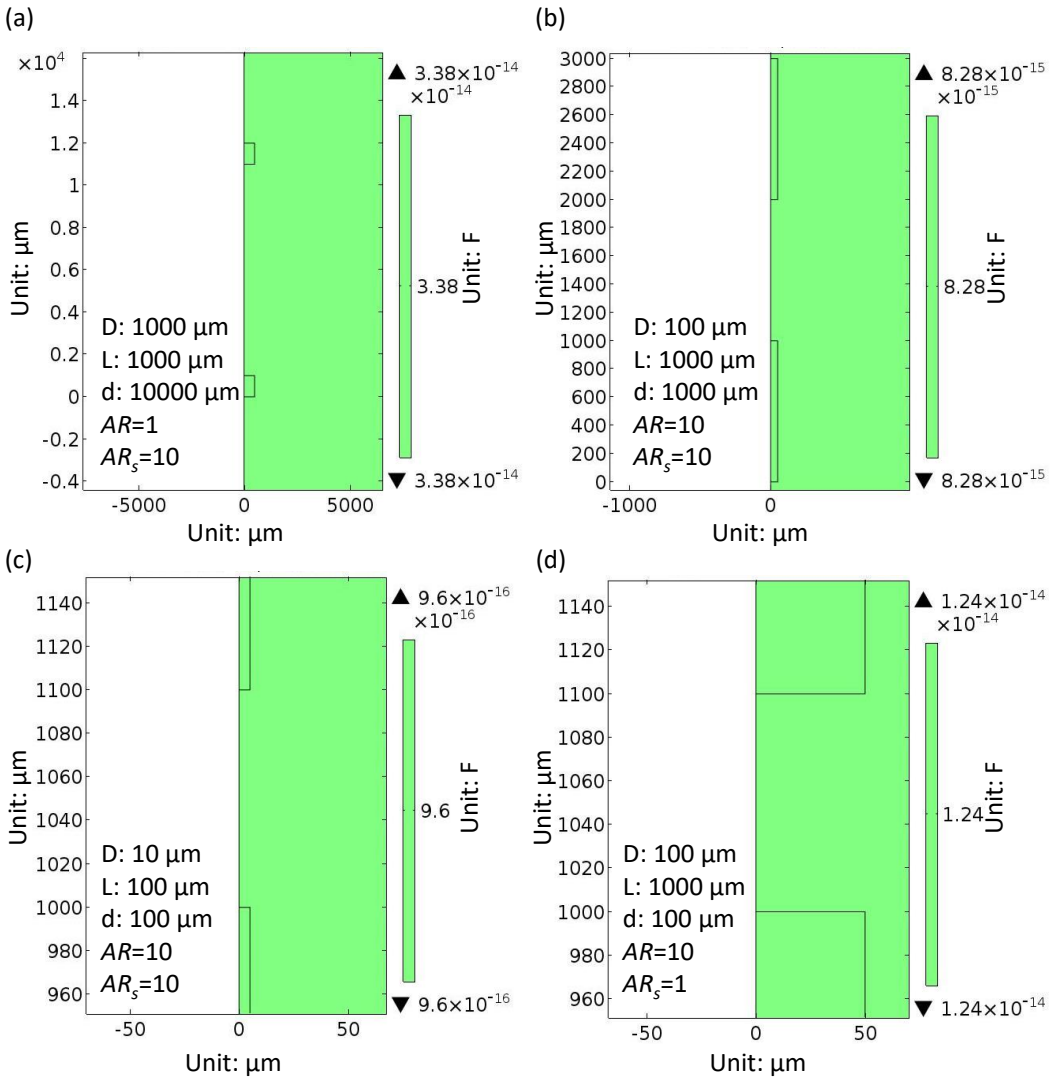

Figure 5.8 FEA results of capacitance for same ARs with different AR (a-b) and same AR with different ARs (c-d).

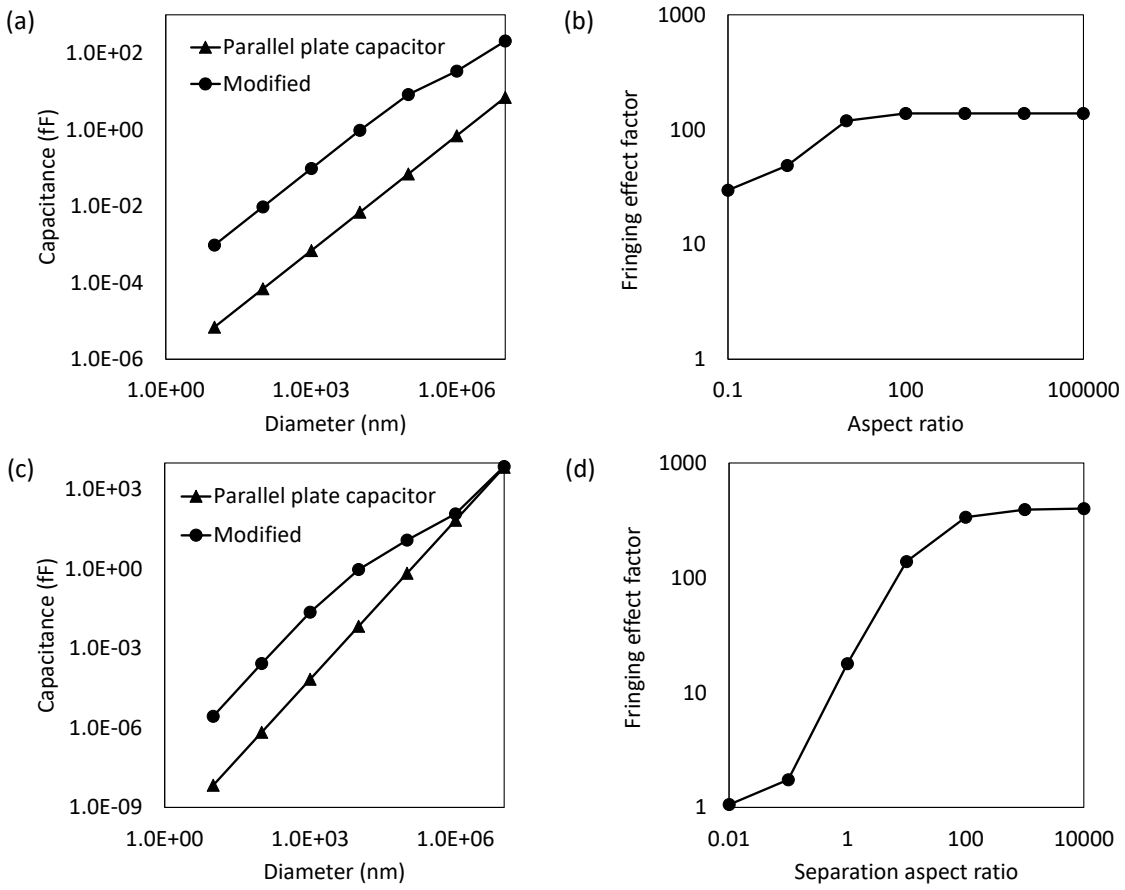

Figure 5.9 (a) Capacitance of parallel plate capacitor and modified capacitor at different electrode diameters with separation aspect ratio of 10. (b) Fringing effect factor at different aspect ratio with separation aspect ratio of 10. (c) Capacitance of parallel plate capacitor and modified capacitor at different electrode diameters with aspect ratio of 10. (d) Fringing effect factor at different separation aspect ratio with aspect ratio of 10.

Based on the numerical results, a fractured CPC is an ideal sensing material for a capacitive sensor with high fringing capacitance. In CPC capacitive sensor, the electrodes are oriented MWCNTs in parallel, which has an *AR* ranging from 30~250. The AR_s of the electrodes was determined by the fracture condition and was higher than 10^4. In a previous report, the electrodes shape was modified to increase the fringing capacitance [148], but complex fabrication procedure was needed.

The fractured condition and morphology of CPC were studied under a microscope (Figure 5.10). The capacitance value of fractured CPC was dominated by the fringing capacitance, and determined by CNT alignment and crack condition. The CNT alignment was controlled by the fractured condition of MWCNTs. The smaller cracks (Figure 5.10b) than distributed cracks will generate higher capacitance. The capacitance of the fractured CPC was as large as 276 fF, which was larger than the planar plate capacitor. This result agreed with the FEA results in Figure 5.7b-c and Figure 5.9a,c. Based on Figure 5.9a,c, the capacitance of a planar plate capacitor with dimension of fractured CPC shown in Figure 5.10 (cross section area= 4×10^{-7} m^2, d= 1mm) was estimated to be in the order of 10^1 fF, while the actual capacitance value was on the order of 10^2 fF. The actual fractured CPC electrodes had a much larger number of nanoscale electrodes in comparison to 5 pairs of electrodes in the simulation results of Figure 5.7. The enhancement ratio of the electric field was in the order of 10^1 instead of 10^0 in Figure 5.7.

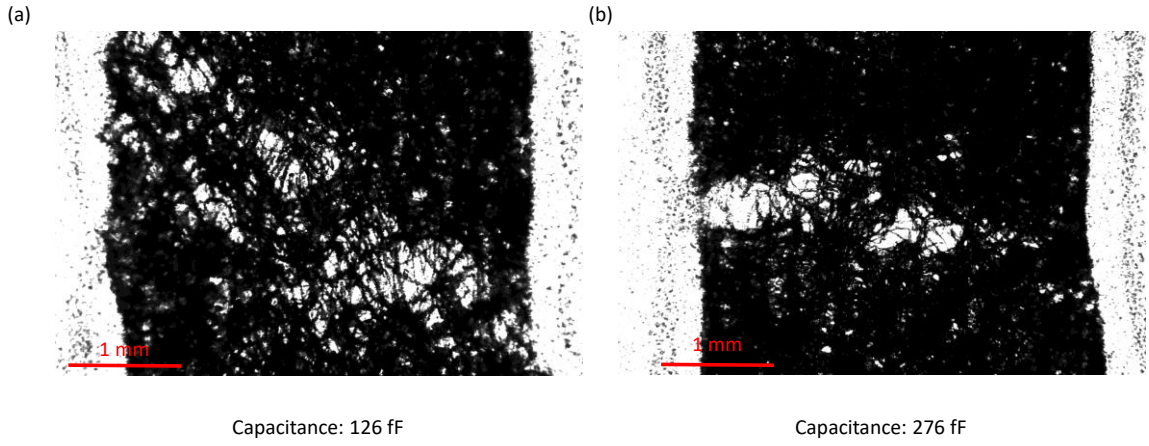

Figure 5.10 Microscope image of CPC with different fracture conditions. (a) Larger cracks. (b) Smaller cracks.

5.4 Capacitive sensing

The sensitivity and resolution of a CPC eye tracking sensor was characterized using spheres coated with aluminum foils that were controlled by a two-dimensional (2D) controller. The experiment setup is shown in Figure 5.11. The sensitivity of the CPC eye tracking sensor is:

$$S = \frac{\Delta C/C_0}{\Delta d} \text{ or } S = \frac{\Delta C/C_0}{\Delta \theta} \tag{5.3}$$

where $\Delta d = d_{i+1} - d_i$, $\Delta \theta = \theta_{i+1} - \theta_i$, $(\frac{\Delta C}{C_0}) = \frac{C_{i+1} - C_i}{C_0}$, where C_0 is the initial capacitance of the sensor, C_i and C_{i+1} are the capacitances at different acquisition times, i.e., samples i and i+1 (i: integers), $d_{i+1}$and d_i are the distance i and i+1 between the sensor and the sphere surface, $\theta_{i+1}$and θ_i are the rotational angle i and i+1 between the sensor and the sphere surface. The resolution of the sensor is:

$$R = \frac{\Delta d}{\frac{\Delta C}{0.5fF}} \text{ or } R = \frac{\Delta \theta}{\frac{\Delta C}{0.5fF}} \tag{5.4}$$

where 0.5 fF is the resolution of a capacitance-to-digital converter (FDC 1004).

The sensitivity was characterized by a perpendicular scanning test. As shown in Figure 5.11a, three diameters (10, 25 and 40mm) of spheres were fabricated by a 3D printer (Creality 3D Technology Co., LTD, China). The spheres wrapped with aluminum foil (Figure 5.12) were fixed on a 2D controller. The movement was controlled with G-codes. Using the setup, above three spheres were controlled such that the distance could be controlled between 0 and 50 mm. The CPC eye tracking sensors were connected to a capacitance-to-digital converter (FDC 1004) to obtain a digitized capacitance value, which

was saved in a laptop computer by a computer software (Texas Instrument, U.S.). The schematic of the capacitance-to-digital converter circuit is shown in Figure 5.13. The CPC eye tracking sensor was connected to the FDC 1004 evaluation module with a shielding layer to eliminate parasitic capacitance by environment.

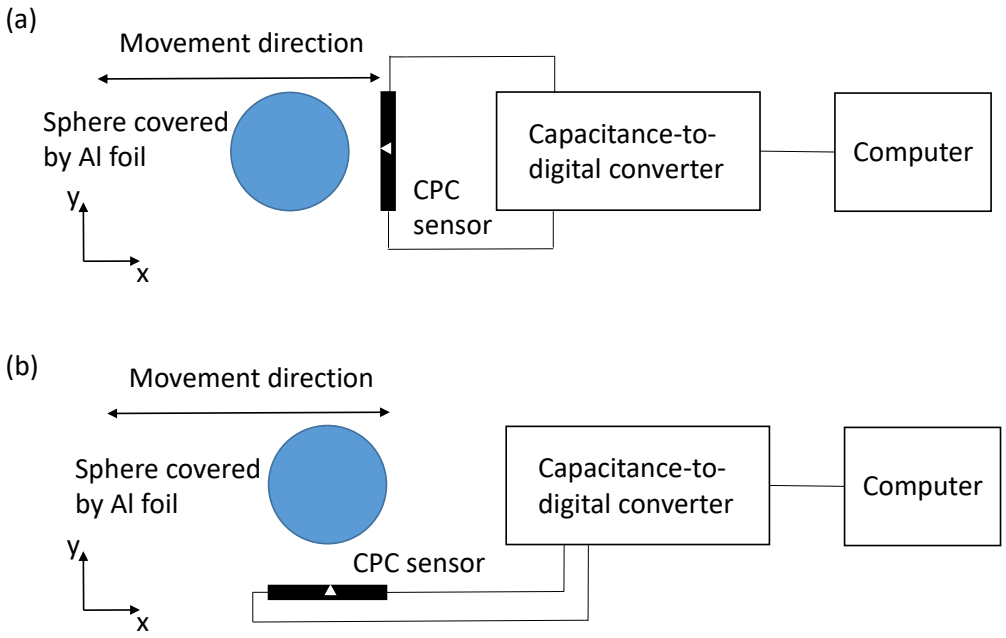

Figure 5.11 (a) Perpendicular scanning setup for CPC sensor calibration (b) Parallel mode experiment setup for CPC sensor calibration.

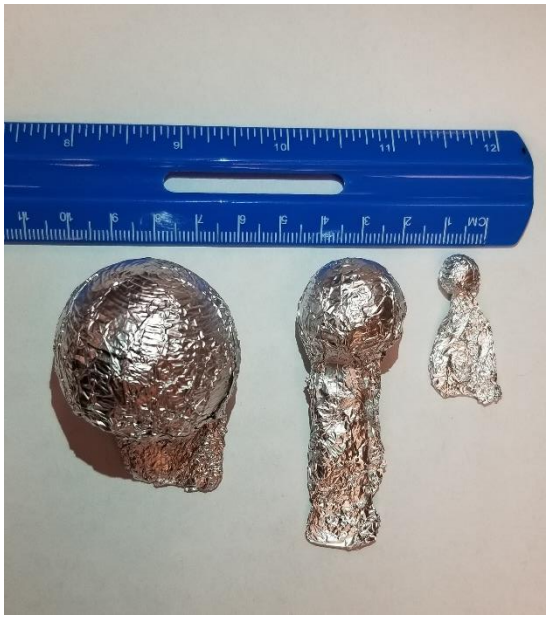

Figure 5.12 3D printed spheres (10, 25 and 40mm) covered with Al foil.

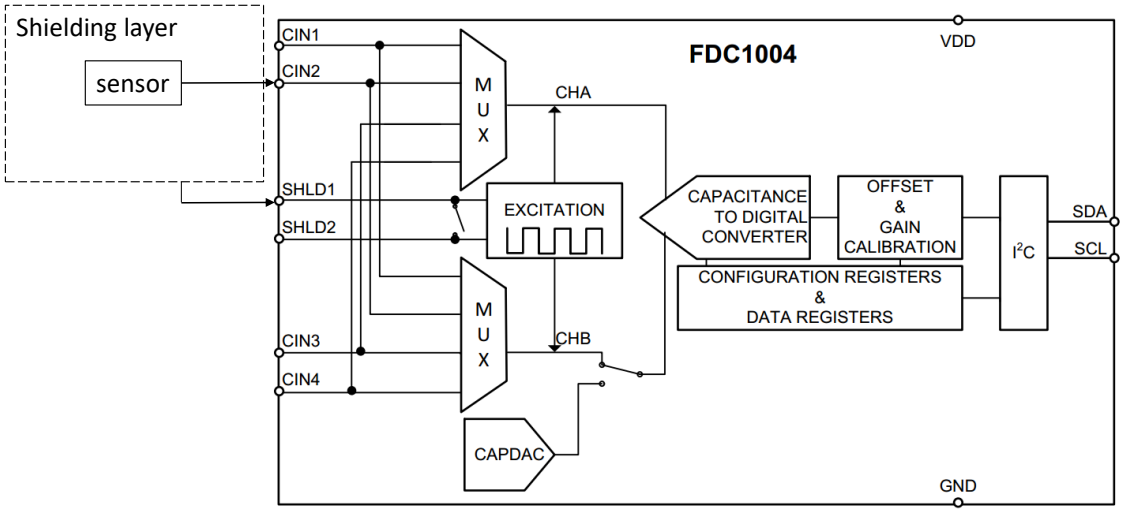

Figure 5.13 Schematic of a capacitance-to-digital converter chip (FDC 1004 in Texas Instrument, US).

The sensitivity of a parallel scanning mode is dependent on the perpendicular distance between the conductive object and the sensor. The sensitivity and resolution of a parallel scanning mode response of a CPC eye tracking sensor is shown in Figure 5.14. As the perpendicular distance became larger, the sensitivity for the CPC eye tracking sensor

became smaller. In eye movement tracking, the perpendicular distance of wearer's eye ball to the sensor was smaller than 10 mm. When the perpendicular distance was smaller than 10mm, the sensitivity was greater than 0.26%/mm. The resolution of CPC eye tracking sensor with different perpendicular distance is shown in Figure 5.14b. The larger perpendicular distances increased the minimum detectable distance change. When the perpendicular distance was smaller than 10mm, the resolution was smaller than 0.83 mm. An empirical correlation was obtained for the decrease of sensitivity and increase of resolution with perpendicular distance:

$$S = 0.0009D^2 - 0.0372D + 0.5679 \quad (5.5)$$

$$R = 0.0444D + 0.3587 \quad (5.6)$$

where D is the perpendicular distance between the sphere movement plane and sensor plane.

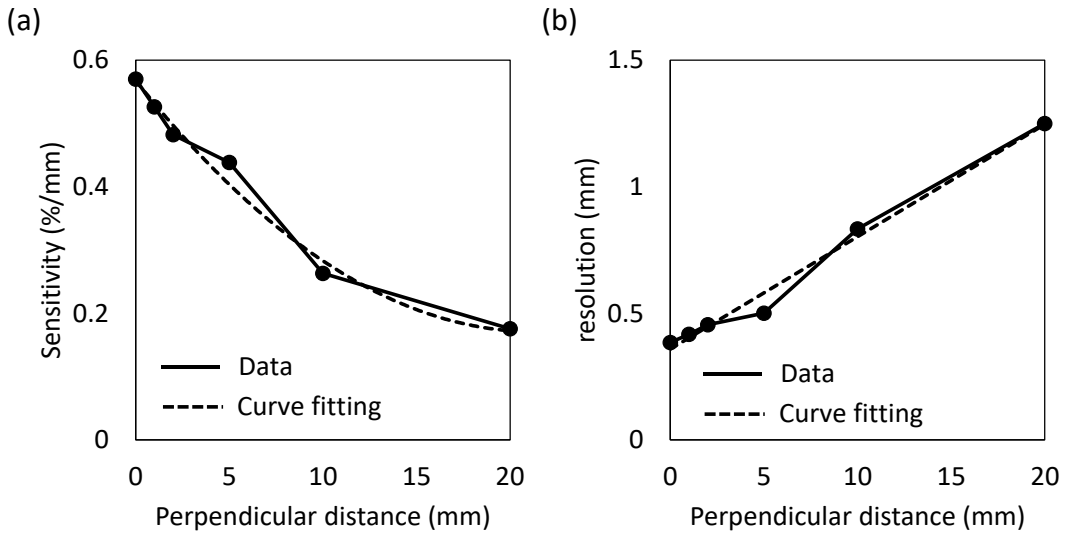

Figure 5.14 (a) Sensitivity of CPC sensor in parallel scanning mode with different perpendicular distance. (b) Resolutions of scanning mode with different perpendicular distance.

The perpendicular scanning mode response of both planar and cantilever CPC eye tracking sensors is shown in Figure 5.15. Figure 5.15a shows the capacitance change for a

planar sensor. The cantilever sensor (Figure 5.15b) had smaller effective sensing area involved in capacitive sensing. Therefore, its capacitance was reduced in comparison to planar sensors. Determined by the sensor shapes, the planar sensor was suitable for being attached on eyeglass surface. The cantilever sensor was suitable for installation on sides of the eyeglass frame to approach more closely to human skin.

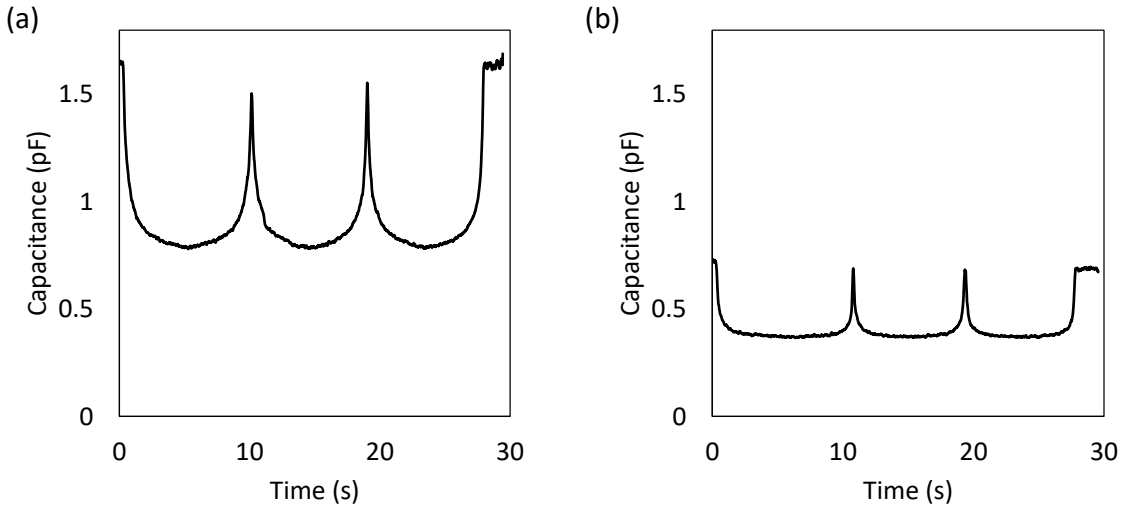

Figure 5.15 Response of CPC sensor in approaching mode for (a) planar (unfolded) sensor and (b) cantilever sensor.

The planar and cantilever sensors showed different sensing characteristic length. The characteristic length indicated the optimum sensing range for the sensor. The sensitivity of the cantilever and planar sensors is shown in Figure 5.16. The sensitivity of the planar sensor was lower than cantilever sensor when the sensing distance was smaller than 5 mm and was higher from 5 to 10 mm. The sensitivity for distance larger than 10 mm was small for both cantilever and planar sensors. The sensing area of the cantilever sensor was the cracked region on CPC and other part of the sensor (unfractured CPC and sensor electrodes) were covered with shielding layers. Fringing electric fields were more concentrated at the cracked region, therefore, the changes at distance smaller than 5 mm

could induce larger capacitance change on a cantilever sensor. However, the sharp tip of the cantilever sensor could not generate fringing field that reaches to a large distance. The sensitivity was reduced at distance larger than 5 mm. The planar sensor without shielding on the unfractured CPC had larger sensing area, which generated a fringing electric field that was sensitive to larger sensing distance. In summary, the cantilever sensor showed a higher sensitivity when the sensor was close to an object surface. The planar sensor showed a higher sensitivity from a larger distance to an object.

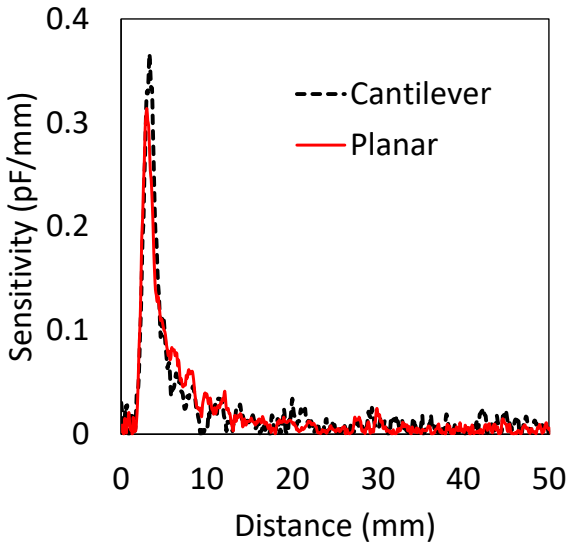

Figure 5.16 Sensitivity of planar and cantilever CPC sensors.

When the diameters of conductive spheres decreased as 40, 25 and 10 mm, the capacitance change of a planar sensor was decreased (Figure 5.17). When the perpendicular distance is smaller than 10 mm, the sensitivity and resolution of 40 mm sphere were 3.1% and 64.5 μm, respectively. A larger sphere induced the larger change of capacitance because a fringing electric field was interfered by more high-permittivity material at the

same distance. Note that 25 mm resembles the diameter of an eye ball. 40 mm represents the size of eyeball with eye lid and corresponding muscles.

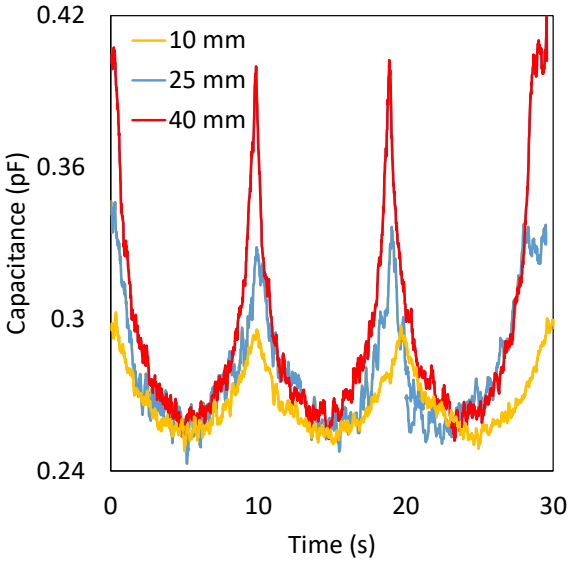

Figure 5.17 Response of CPC sensor in perpendicular scanning mode for sphere with diameter of 40mm, 25mm and 10mm.

5.5 Eye movement sensing with simulation stage

An eyeball movement simulation system was developed based on the physiological structure of a human eyeball (Figure 5.18a) for characterization of the sensing performance of CPC eye tracking sensors. The eye ball is connected by medial and lateral rectus in horizontal direction and superior and inferior rectus vertical muscles. These muscles pull the eyeball in horizontal and vertical directions for rotation. The aqueous humor in anterior chamber forms a bulge on the eyeball (Figure 5.18b) and the eyelid movements are also considered. An eyeball model was built by 3D printer to simulate the movement of an eyelid and the bulge on an eyeball. An eyeball movement stage was built to simulate the rotation of eyeball in horizontal and vertical directions based on the eyeball structure and its movement (Figure 5.19). The rotational angle is defined as 0° when eye is looking straight horizontally, positive for looking up and left, negative for looking down and right. Angular rotation in two directions with two shafts simulated eye ball rotation. The capacitance changes were recorded during angular rotation.

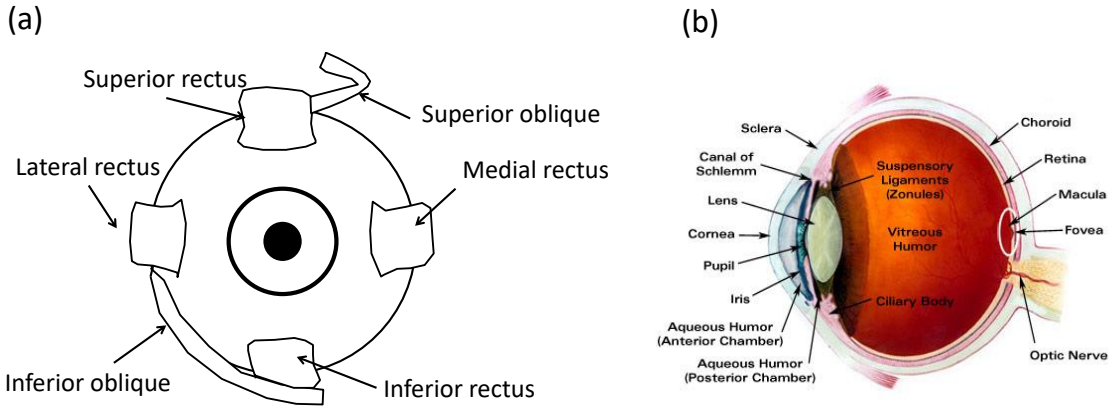

Figure 5.18 (a) Physiological structure of eyeball (front view) (b) Physiological structure of eyeball (side view).

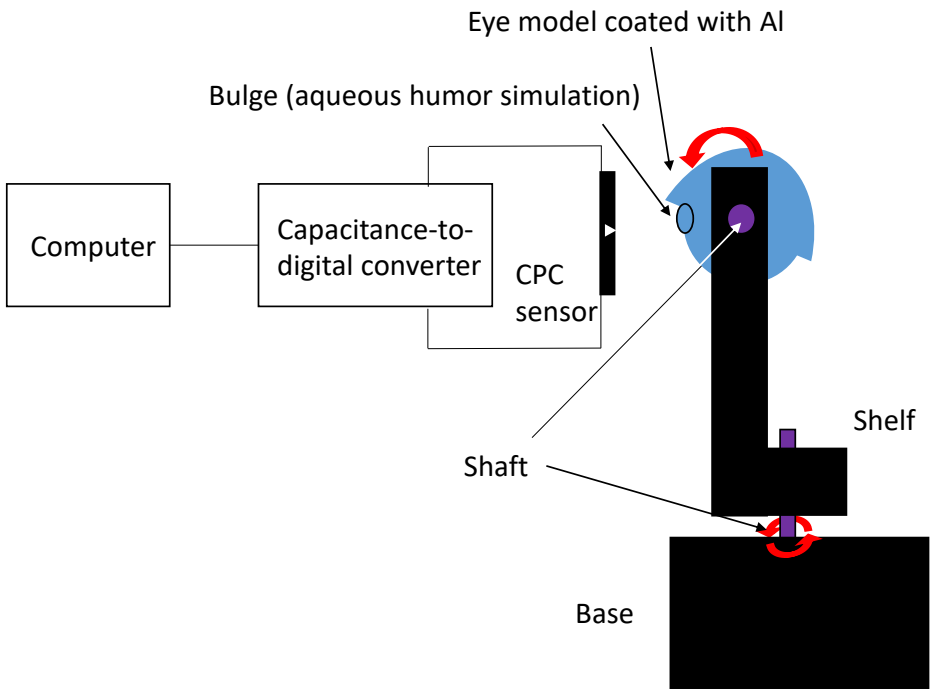

Figure 5.19 2-axis eyeball rotation simulation stage.

The capacitance change of a CPC eye tracking sensor was recorded when a simulated eye was rotated up and down (Figure 5.20). A simulated eye was fabricated by using a 3D printer mimicking an eye ball covered with an eye lid. According to the characterization, a CPC sensor showed a resolution of 0.12° for the rotation of an eye ball when the distance between the eyeball and the sensor was smaller than 10 mm.

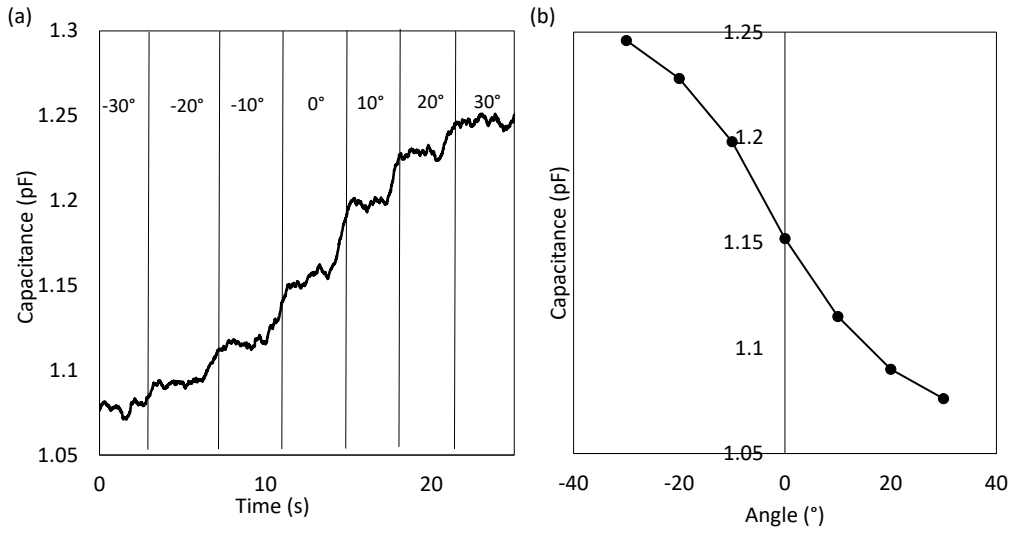

Figure 5.20 (a) Capacitance response to different angle of simulated eye ball vertical movement. (b) Correlation of sensitivity and eye movement angles.

5.6 Wearable eye tracking device

A CPC eye tracking sensor was installed on eyeglasses for wearer's eye movement detection. A CPC eye tracking sensor was installed at the upper frame of the eyeglasses. When eyeglasses were worn, the capacitance changes of the CPC eye tracking sensor were recorded as wearer was looking up and down.

When a CPC capacitive eye tracking sensor installed on a glass, the up and down motion of an eyeball could be detected. The response of the CPC eye tracking sensor for looking up and down direction is shown in Figure 5.21. The test was performed by deidentified volunteers. The capacitance change was induced by the rotation of the eyeball, the eyelid and muscles movement. The angle change between looking up and down was 40°, and the capacitance change was 70 fF. Based on equation (5.3-5.4), the sensitivity and resolution were 0.16%/° and 0.28°, respectively. Because of the complex shape change and the combined movement of eyeball, eyelid and muscles, the capacitance response of CPC eye tracking sensor was not linear to the eye movement angles. Further calibration should be required for more precise conclusion.

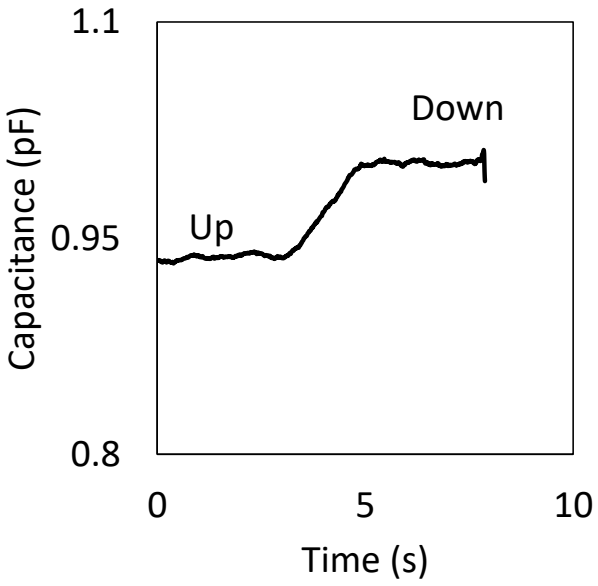

Figure 5.21 Capacitance change of CPC eye tracking sensor installed on glasses. Eyes moved from looking up to looking down.

Chapter 6. Conclusions

6.1 Summary of contributions

In summary, we presented a low cost, flexible, and highly sensitive sensor whose sensitivity was induced by controlled fracture on a MWCNTs-paper composite. By pre-straining, three different sensors were demonstrated as resistive strain sensor, resistive force sensor, and capacitive force and displacement sensors. The piezo-resistive and capacitive sensors could be fabricated by the reorganized crossing junctions of MWCNT-coated cellulose fibers. The calibration of each sensor showed reliability and repeatability. The sensors attached onto flexible surface such as human skin were sensitive enough to monitor heart beats, grabbing force, finger motion, and eye movement. The inexpensive and disposable sensors can be useful to monitor human behaviors with reliable performance.

A sensitive humidity CPC-based sensor was fabricated and tested. The swelling of the cellulose fibers at conditions above critical RH levels disrupted the CNT network resulting in a sharp change for a resistance. PAA treatment of the CPC matrix allowed to enhance the sensitivity of a CPC humidity sensor and extended the operating range to RH=30~95%. The sensor hysteresis from water retention in the CPC matrix was observed. The hysteresis was reduced after three RH cycles or after heat curing of the CPC matrix. The contact resistance at the CPC-silver interface exhibited greater hysteresis and lower sensitivity than the CPC matrix itself. An empirical relationship for the normalized resistance-humidity curve was obtained by calibration. The calibrated CPC sensor could be used to measure the rate of water evaporation using a simulated sweat setup. The CPC

sensor can be used for health monitoring, smart air conditioning, food process monitoring, and agricultural applications.

Using the fracture-induced fabrication method, two types of sensors including planar and cantilever shapes were fabricated with a yield of 91%. The sensing mechanism and sensing performance improvement was studied with a numerical method in the context of a fringing electric field. The sensor calibration system was constructed using a capacitance-to-digital converter that was interfaced to a laptop computer. Using a spherical shape conductor, the sensitivity and the resolution were characterized by varying the distance between the sensor and the sphere surface. In the characterization using a simulated eyeball, the up and down rotational motion of an eyeball could be measured with resolution of 0.12° at the distance of 10 mm.

6.2 Future work

The CPC material can be further applied to manufacture various sensors based on the high sensitivity. The advantages of the paper-based sensor and nanomaterial composites provide great potentials in the fabrication of sensors in various fields.

The thin film shaped CPC also offers a promising future for manufacturing a new generation of wearable sweat sensor to monitor the sweat level of the wearer for biomedical or sports fields. Based on CPC's sensitivity to pH change and chemicals in sweat, an integrated wearable sweat sensor can be developed for the measurement of multiple physiological information.

A wearable sensor that measures foot pressure will be developed. Fabrication challenges to strengthen the fragile paper structure will be addressed. By measuring the pressure on a foot, the sensing capability of the proposed wearable sensor will be demonstrated.

The eye tracking device with higher sensitivity and resolution can be developed with multiple CPC sensors installed at selected positions around eye ball. The portability and wearing comfort of the eye tracking device will be improved with more compact design of the capacitance measuring circuit and wireless communication module.

List of Reference

1. Cheng, Y., et al., *A stretchable and highly sensitive graphene-based fiber for sensing tensile strain, bending, and torsion.* Advanced materials, 2015. **27**(45): p. 7365-7371.
2. Patel, S., et al., *A review of wearable sensors and systems with application in rehabilitation.* Journal of neuroengineering and rehabilitation, 2012. **9**(1): p. 21.
3. Rodgers, M.M., V.M. Pai, and R.S. Conroy, *Recent Advances in Wearable Sensors for Health Monitoring.* IEEE Sensors Journal, 2015. **15**(6): p. 3119-3126.
4. Yousef, H., M. Boukallel, and K. Althoefer, *Tactile sensing for dexterous in-hand manipulation in robotics—A review.* Sensors and Actuators A: physical, 2011. **167**(2): p. 171-187.
5. Swan, M., *Sensor mania! the internet of things, wearable computing, objective metrics, and the quantified self 2.0.* Journal of Sensor and Actuator Networks, 2012. **1**(3): p. 217-253.
6. Heinz, E.A., et al. *Using wearable sensors for real-time recognition tasks in games of martial arts-an initial experiment*. in *Computational Intelligence and Games, 2006 IEEE Symposium on*. 2006. IEEE.
7. Phan, D., et al. *Smartwatch: Performance evaluation for long-term heart rate monitoring*. in *Bioelectronics and Bioinformatics (ISBB), 2015 International Symposium on*. 2015. IEEE.
8. Trung, T.Q., et al., *An All-Elastomeric Transparent and Stretchable Temperature Sensor for Body-Attachable Wearable Electronics.* Advanced Materials, 2016. **28**(3): p. 502-509.
9. Lee, H., et al., *Wearable/disposable sweat-based glucose monitoring device with multistage transdermal drug delivery module.* Science Advances, 2017. **3**(3): p. e1601314.
10. Edwards, J., *Wireless sensors relay medical insight to patients and caregivers [special reports]*. IEEE Signal Processing Magazine, 2012. **29**(3): p. 8-12.
11. Malhi, K., et al., *A zigbee-based wearable physiological parameters monitoring system.* IEEE sensors journal, 2012. **12**(3): p. 423-430.
12. Salvo, P., et al., *A wearable sensor for measuring sweat rate.* IEEE Sensors Journal, 2010. **10**(10): p. 1557-1558.
13. Strohrmann, C., et al., *Monitoring kinematic changes with fatigue in running using body-worn sensors.* IEEE transactions on information technology in biomedicine, 2012. **16**(5): p. 983-990.
14. Shaltis, P.A., A.T. Reisner, and H.H. Asada, *Cuffless blood pressure monitoring using hydrostatic pressure changes.* IEEE Transactions on Biomedical Engineering, 2008. **55**(6): p. 1775-1777.
15. Poh, M.-Z., et al., *Cardiovascular monitoring using earphones and a mobile device.* IEEE Pervasive Computing, 2012. **11**(4): p. 18-26.
16. Chen, B.-R., et al., *A web-based system for home monitoring of patients with Parkinson's disease using wearable sensors.* IEEE Transactions on Biomedical Engineering, 2011. **58**(3): p. 831-836.
17. Allet, L., et al., *Wearable systems for monitoring mobility-related activities in chronic disease: a systematic review.* Sensors, 2010. **10**(10): p. 9026-9052.
18. Beaglehole, R., et al., *Prevention of chronic diseases: a call to action.* The Lancet, 2008. **370**(9605): p. 2152-2157.
19. Katzmarzyk, P.T. and I. Janssen, *The economic costs associated with physical inactivity and obesity in Canada: an update.* Canadian journal of applied physiology, 2004. **29**(1): p. 90-115.
20. de Lima, A.L.S., et al., *Freezing of gait and fall detection in Parkinson's disease using wearable sensors: a systematic review.* Journal of Neurology, 2017: p. 1-13.

21. Pan, D., et al., *A mobile cloud-based parkinson's disease assessment system for home-based monitoring.* JMIR mHealth and uHealth, 2015. **3**(1).
22. Majaranta, P. and A. Bulling, *Eye tracking and eye-based human–computer interaction*, in *Advances in physiological computing*. 2014, Springer. p. 39-65.
23. Bulling, A., J.A. Ward, and H. Gellersen, *Multimodal recognition of reading activity in transit using body-worn sensors.* ACM Transactions on Applied Perception (TAP), 2012. **9**(1): p. 2.
24. Champaty, B., et al. *Development of EOG based human machine interface control system for motorized wheelchair*. in *Emerging Research Areas: Magnetics, Machines and Drives (AICERA/iCMMD), 2014 Annual International Conference on*. 2014. IEEE.
25. Ujjainiya, L., M.K. Chakravarthi, and A. Soni, *Development and implementation of gesture controlled automatic audio system.* International Journal of Computer Applications, 2014. **106**(13).
26. Asokan, A., A.J. Pothen, and R.K. Vijayaraj. *ARMatron—A wearable gesture recognition glove: For control of robotic devices in disaster management and human Rehabilitation*. in *Robotics and Automation for Humanitarian Applications (RAHA), 2016 International Conference on*. 2016. IEEE.
27. Assad, C., et al. *Live demonstration: BioSleeve, a wearable hands-free gesture control interface*. in *SENSORS, 2016 IEEE*. 2016. IEEE.
28. Assad, C., et al. *Live demonstration: BioSleeve, a wearable hands-free gesture control interface*. in *2016 IEEE SENSORS*. 2016. IEEE.
29. Yang, C.-C. and Y.-L. Hsu, *A review of accelerometry-based wearable motion detectors for physical activity monitoring.* Sensors, 2010. **10**(8): p. 7772-7788.
30. Nery, E.W. and L.T. Kubota, *Sensing approaches on paper-based devices: a review.* Analytical and bioanalytical chemistry, 2013. **405**(24): p. 7573-7595.
31. Zhao, J., et al., *Gas molecule adsorption in carbon nanotubes and nanotube bundles.* Nanotechnology, 2002. **13**(2): p. 195.
32. Geng, H.-Z., et al., *Effect of acid treatment on carbon nanotube-based flexible transparent conducting films.* Journal of the American Chemical Society, 2007. **129**(25): p. 7758-7759.
33. Chandran, P.L. and V.H. Barocas, *Affine versus non-affine fibril kinematics in collagen networks: theoretical studies of network behavior.* Journal of biomechanical engineering, 2006. **128**(2): p. 259-270.
34. Banaee, H., M.U. Ahmed, and A. Loutfi, *Data mining for wearable sensors in health monitoring systems: a review of recent trends and challenges.* Sensors, 2013. **13**(12): p. 17472-17500.
35. Hepworth, D., et al., *Affine versus non-affine deformation in soft biological tissues, measured by the reorientation and stretching of collagen fibres through the thickness of compressed porcine skin.* Journal of biomechanics, 2001. **34**(3): p. 341-346.
36. Fulk, G.D., et al., *Accuracy of 2 activity monitors in detecting steps in people with stroke and traumatic brain injury.* Physical therapy, 2014. **94**(2): p. 222-229.
37. Bandodkar, A.J. and J. Wang, *Non-invasive wearable electrochemical sensors: a review.* Trends Biotechnol, 2014. **32**(7): p. 363-71.
38. Bakker, J., M. Pechenizkiy, and N. Sidorova, *What's Your Current Stress Level? Detection of Stress Patterns from GSR Sensor Data.* 2011: p. 573-580.
39. Tseng, S.-C., et al., *Eco-friendly plasmonic sensors: using the photothermal effect to prepare metal nanoparticle-containing test papers for highly sensitive colorimetric detection.* Analytical chemistry, 2012. **84**(11): p. 5140-5145.
40. Barr, M.C., et al., *Direct monolithic integration of organic photovoltaic circuits on unmodified paper.* Advanced Materials, 2011. **23**(31): p. 3500-3505.
41. Zhao, W., et al., *based bioassays using gold nanoparticle colorimetric probes.* Analytical chemistry, 2008. **80**(22): p. 8431-8437.

42. Ge, X., et al., *Nanomaterial-enhanced paper-based biosensors.* TrAC Trends in Analytical Chemistry, 2014. **58**: p. 31-39.
43. Didonna, B.A. and T.C. Lubensky, *Nonaffine correlations in random elastic media.* Phys Rev E Stat Nonlin Soft Matter Phys, 2005. **72**(6 Pt 2): p. 066619.
44. Taniere, A., B. Oesterle, and J. Monnier, *On the behaviour of solid particles in a horizontal boundary layer with turbulence and saltation effects.* Experiments in Fluids, 1997. **23**(6): p. 463-471.
45. Tobjörk, D. and R. Österbacka, *Paper electronics.* Advanced Materials, 2011. **23**(17): p. 1935-1961.
46. Dichiara, A., et al., *Smart papers comprising carbon nanotubes and cellulose microfibers for multifunctional sensing applications.* Journal of Materials Chemistry A, 2017. **5**(38): p. 20161-20169.
47. Mahadeva, S.K., K. Walus, and B. Stoeber, *Paper as a Platform for Sensing Applications and Other Devices: A Review.* Acs Applied Materials & Interfaces, 2015. **7**(16): p. 8345-8362.
48. Liu, B.W., et al., *Paper-Based Electrochemical Biosensors: From Test Strips to Paper-Based Microfluidics.* Electroanalysis, 2014. **26**(6): p. 1214-1223.
49. Chen, H., et al., *Non-linear micromechanics of soft tissues.* Int J Non Linear Mech, 2013. **58**: p. 79-85.
50. Sicard, C. and J.D. Brennan, *Bioactive paper: biomolecule immobilization methods and applications in environmental monitoring.* MRS bulletin, 2013. **38**(4): p. 331-334.
51. Credou, J. and T. Berthelot, *Cellulose: from biocompatible to bioactive material.* Journal of Materials Chemistry B, 2014. **2**(30): p. 4767-4788.
52. Saha, B., S. Baek, and J. Lee, *Highly Sensitive Bendable and Foldable Paper Sensors Based on Reduced Graphene Oxide.* ACS applied materials & interfaces, 2017. **9**(5): p. 4658-4666.
53. Lin, C.-W., et al., *Pencil drawn strain gauges and chemiresistors on paper.* Scientific reports, 2014. **4**: p. 3812.
54. Li, C.G., et al., *One-touch-activated blood multidiagnostic system using a minimally invasive hollow microneedle integrated with a paper-based sensor.* Lab on a Chip, 2015. **15**(16): p. 3286-3292.
55. Yan, C., et al., *Highly stretchable piezoresistive graphene–nanocellulose nanopaper for strain sensors.* Advanced materials, 2014. **26**(13): p. 2022-2027.
56. Chen, G.-H., et al., *Detection of mercury (II) ions using colorimetric gold nanoparticles on paper-based analytical devices.* Analytical chemistry, 2014. **86**(14): p. 6843-6849.
57. Määttänen, A., et al., *A low-cost paper-based inkjet-printed platform for electrochemical analyses.* Sensors and Actuators B: Chemical, 2013. **177**: p. 153-162.
58. Morales-Narváez, E., et al., *Photoluminescent lateral-flow immunoassay revealed by graphene oxide: highly sensitive paper-based pathogen detection.* Analytical chemistry, 2015. **87**(16): p. 8573-8577.
59. Sun, G., et al., *Photoelectrochemical sensor for pentachlorophenol on microfluidic paper-based analytical device based on the molecular imprinting technique.* Biosensors and Bioelectronics, 2014. **56**: p. 97-103.
60. Abbas, A., et al., *Multifunctional analytical platform on a paper strip: separation, preconcentration, and subattomolar detection.* Analytical chemistry, 2013. **85**(8): p. 3977-3983.
61. Clarke, S.L. and G.P. McGlacken, *Methyl fluorosulfonyldifluoroacetate (MFSDA): an underutilised reagent for trifluoromethylation.* Chemistry–A European Journal, 2017. **23**(6): p. 1219-1230.
62. Liao, X.Q., et al., *Flexible and Highly Sensitive Strain Sensors Fabricated by Pencil Drawn for Wearable Monitor.* Advanced Functional Materials, 2015. **25**(16): p. 2395-2401.

63. Qian, H., et al., *Carbon nanotube-based hierarchical composites: a review.* Journal of Materials Chemistry, 2010. **20**(23): p. 4751-4762.
64. Kim, M., et al., *Processing, characterization, and modeling of carbon nanotube-reinforced multiscale composites.* Composites Science and Technology, 2009. **69**(3-4): p. 335-342.
65. Qian, H., et al., *Hierarchical composites reinforced with carbon nanotube grafted fibers: The potential assessed at the single fiber level.* Chemistry of Materials, 2008. **20**(5): p. 1862-1869.
66. Qian, H., et al., *Carbon nanotube grafted carbon fibres: A study of wetting and fibre fragmentation.* Composites Part a-Applied Science and Manufacturing, 2010. **41**(9): p. 1107-1114.
67. Bekyarova, E., et al., *Multiscale carbon nanotube-carbon fiber reinforcement for advanced epoxy composites.* Langmuir, 2007. **23**(7): p. 3970-3974.
68. He, X.D., et al., *Preparation of a carbon nanotube/carbon fiber multi-scale reinforcement by grafting multi-walled carbon nanotubes onto the fibers.* Carbon, 2007. **45**(13): p. 2559-2563.
69. Karapappas, P., et al., *MULTI-WALL CARBON NANOTUBES CHEMICALLY GRAFTED AND PHYSICALLY ADSORPTED ON REINFORCING CARBON FIBRES.* Advanced Composites Letters, 2008. **17**(3): p. 103-107.
70. Hu, L.B., et al., *Highly conductive paper for energy-storage devices.* Proceedings of the National Academy of Sciences of the United States of America, 2009. **106**(51): p. 21490-21494.
71. Pushparaj, V.L., et al., *Flexible energy storage devices based on nanocomposite paper.* Proceedings of the National Academy of Sciences of the United States of America, 2007. **104**(34): p. 13574-13577.
72. Fotouhi, G., et al., *A low cost, disposable cable-shaped Al–air battery for portable biosensors.* Journal of Micromechanics and Microengineering, 2016. **26**(5): p. 055011.
73. Han, J.W., et al., *A carbon nanotube based ammonia sensor on cellulose paper.* Rsc Advances, 2014. **4**(2): p. 549-553.
74. Thostenson, E.T., et al., *Electrical anisotropy in multiscale nanotube/fiber hybrid composites.* Applied Physics Letters, 2009. **95**(7).
75. Mirica, K.A., et al., *Rapid prototyping of carbon-based chemiresistive gas sensors on paper.* Proceedings of the National Academy of Sciences of the United States of America, 2013. **110**(35): p. E3265-E3270.
76. Ge, D.T., et al., *Foldable supercapacitors from triple networks of macroporous cellulose fibers, single-walled carbon nanotubes and polyaniline nanoribbons.* Nano Energy, 2015. **11**: p. 568-578.
77. Dossi, N., et al., *Doped pencil leads for drawing modified electrodes on paper-based electrochemical devices.* Journal of Electroanalytical Chemistry, 2014. **722**: p. 90-94.
78. Lin, C.W., et al., *Pencil Drawn Strain Gauges and Chemiresistors on Paper.* Scientific Reports, 2014. **4**.
79. Qi, H.S., et al., *Cellulose fibres with carbon nanotube networks for water sensing.* Journal of Materials Chemistry A, 2014. **2**(15): p. 5541-5547.
80. Yun, S. and J. Kim, *Covalently bonded multi-walled carbon nanotubes-cellulose electro-active paper actuator.* Sensors and Actuators a-Physical, 2009. **154**(1): p. 73-78.
81. Berglund, L.A. and T. Peijs, *Cellulose Biocomposites-From Bulk Moldings to Nanostructured Systems.* Mrs Bulletin, 2010. **35**(3): p. 201-207.
82. Huang, J.G. and Y.Q. Gu, *Self-assembly of various guest substrates in natural cellulose substances to functional nanostructured materials.* Current Opinion in Colloid & Interface Science, 2011. **16**(6): p. 470-481.
83. Barocas, V.H. and R.T. Tranquillo, *An anisotropic biphasic theory of tissue-equivalent mechanics: The interplay among cell traction, fibrillar network deformation, fibril*

alignment, and cell contact guidance. Journal of Biomechanical Engineering-Transactions of the Asme, 1997. **119**(2): p. 137-145.
84. Chandran, P.L. and V.H. Barocas, *Affine versus non-affine fibril kinematics in collagen networks: Theoretical studies of network behavior*. Journal of Biomechanical Engineering-Transactions of the Asme, 2006. **128**(2): p. 259-270.
85. Yun, S. and J. Kim, *Multi-walled carbon nanotubes–cellulose paper for a chemical vapor sensor*. Sensors and Actuators B: Chemical, 2010. **150**(1): p. 308-313.
86. Chopra, S., et al., *Selective gas detection using a carbon nanotube sensor.* Applied Physics Letters, 2003. **83**(11): p. 2280-2282.
87. Han, J.-W., et al., *A carbon nanotube based ammonia sensor on cellulose paper*. RSC Advances, 2014. **4**(2): p. 549-553.
88. Park, M., H. Kim, and J.P. Youngblood, *Strain-dependent electrical resistance of multi-walled carbon nanotube/polymer composite films.* Nanotechnology, 2008. **19**(5): p. 055705.
89. Feng, S., et al., *PERCOLATION ON TWO-DIMENSIONAL ELASTIC NETWORKS WITH ROTATIONALLY INVARIANT BOND-BENDING FORCES.* Physical Review B, 1984. **30**(9): p. 5386-5389.
90. Taya, M., W.J. Kim, and K. Ono, *Piezoresistivity of a short fiber/elastomer matrix composite*. Mechanics of Materials, 1998. **28**(1-4): p. 53-59.
91. You, I., et al., *Stretchable E-Skin Apexcardiogram Sensor.* Advanced Materials, 2016. **28**(30): p. 6359-+.
92. Chen, H.-W., et al., *The application of CNT/Nafion composite material to low humidity sensing measurement.* Sensors and Actuators B: Chemical, 2005. **104**(1): p. 80-84.
93. Chen, Z. and C. Lu, *Humidity sensors: a review of materials and mechanisms.* Sensor letters, 2005. **3**(4): p. 274-295.
94. Lee, C.-Y. and G.-B. Lee, *Humidity sensors: a review.* Sensor Letters, 2005. **3**(1-2): p. 1-15.
95. Woyessa, G., et al., *Temperature insensitive hysteresis free highly sensitive polymer optical fiber Bragg grating humidity sensor.* Optics express, 2016. **24**(2): p. 1206-1213.
96. Squillaci, M.A., et al., *Self-Assembly of an Amphiphilic π-Conjugated Dyad into Fibers: Ultrafast and Ultrasensitive Humidity Sensor.* Advanced Materials, 2015. **27**(20): p. 3170-3174.
97. Zhang, D., et al., *Ultrahigh performance humidity sensor based on layer-by-layer self-assembly of graphene oxide/polyelectrolyte nanocomposite film.* Sensors and Actuators B: Chemical, 2014. **203**: p. 263-270.
98. Cinke, M., et al., *Pore structure of raw and purified HiPco single-walled carbon nanotubes.* Chemical Physics Letters, 2002. **365**(1-2): p. 69-74.
99. Wang, Y. and J.T. Yeow, *A review of carbon nanotubes-based gas sensors.* Journal of Sensors, 2009. **2009**.
100. Cao, C., et al., *Humidity sensor based on multi-walled carbon nanotube thin films.* Journal of Nanomaterials, 2011. **2011**: p. 5.
101. Jung, D., M. Han, and G.S. Lee, *Humidity-sensing characteristics of multi-walled carbon nanotube sheet.* Materials Letters, 2014. **122**: p. 281-284.
102. Star, A., et al., *Sensing with Nafion coated carbon nanotube field-effect transistors.* Electroanalysis: An International Journal Devoted to Fundamental and Practical Aspects of Electroanalysis, 2004. **16**(1-2): p. 108-112.
103. Zhang, T., et al., *Recent progress in carbon nanotube-based gas sensors.* Nanotechnology, 2008. **19**(33): p. 332001.
104. Li, X., et al., *High-sensitive humidity sensor based on graphene oxide with evenly dispersed multiwalled carbon nanotubes.* Materials Chemistry and Physics, 2018. **207**: p. 135-140.

105. Yoo, K.-P., et al., *Novel resistive-type humidity sensor based on multiwall carbon nanotube/polyimide composite films.* Sensors and Actuators B: Chemical, 2010. **145**(1): p. 120-125.
106. Peng, X., et al., *A flexible humidity sensor based on KC–MWCNTs composites.* Applied Surface Science, 2016. **387**: p. 149-154.
107. Lee, J., et al., *Magnetically aligned iron oxide/gold nanoparticle-decorated carbon nanotube hybrid structure as a humidity sensor.* ACS applied materials & interfaces, 2015. **7**(28): p. 15506-15513.
108. Tang, Q.-Y., Y. Chan, and K. Zhang, *Fast response resistive humidity sensitivity of polyimide/multiwall carbon nanotube composite films.* Sensors and Actuators B: Chemical, 2011. **152**(1): p. 99-106.
109. Han, J.-W., et al., *Carbon nanotube based humidity sensor on cellulose paper.* The Journal of Physical Chemistry C, 2012. **116**(41): p. 22094-22097.
110. Rosace, G., et al., *Structural and morphological characterizations of MWCNTs hybrid coating onto cotton fabric as potential humidity and temperature wearable sensor.* Sensors and Actuators B: Chemical, 2017. **252**: p. 428-439.
111. Ummartyotin, S. and H. Manuspiya, *A critical review on cellulose: from fundamental to an approach on sensor technology.* Renewable and Sustainable Energy Reviews, 2015. **41**: p. 402-412.
112. Klemm, D., et al., *Cellulose: fascinating biopolymer and sustainable raw material.* Angewandte Chemie International Edition, 2005. **44**(22): p. 3358-3393.
113. Faruk, O., et al., *Biocomposites reinforced with natural fibers: 2000–2010.* Progress in polymer science, 2012. **37**(11): p. 1552-1596.
114. Wu, X., et al., *Cellulose nanowhisker modulated 3D hierarchical conductive structure of carbon black/natural rubber nanocomposites for liquid and strain sensing application.* Composites Science and Technology, 2016. **124**: p. 44-51.
115. Villmow, T., et al., *Liquid sensing: smart polymer/CNT composites.* Materials Today, 2011. **14**(7-8): p. 340-345.
116. Qi, H., E. Mäder, and J. Liu, *Unique water sensors based on carbon nanotube–cellulose composites.* Sensors and Actuators B: Chemical, 2013. **185**: p. 225-230.
117. Güder, F., et al., *Paper-based electrical respiration sensor.* Angewandte Chemie International Edition, 2016. **55**(19): p. 5727-5732.
118. Zhao, H., et al., *Drawn on Paper: A Reproducible Humidity Sensitive Device by Handwriting.* ACS applied materials & interfaces, 2017. **9**(33): p. 28002-28009.
119. Zhang, J., et al., *Fracture-Induced Mechanoelectrical Sensitivities of Paper-Based Nanocomposites.* Advanced Materials Technologies, 2018. **3**(3): p. 1700266.
120. He, J. and I.V. Novosselov, *Design and evaluation of an aerodynamic focusing micro-well aerosol collector.* Aerosol Science and Technology, 2017. **51**(9): p. 1016-1026.
121. He, J., et al., *Evaluation of micro-well collector for capture and analysis of aerosolized Bacillus subtilis spores.* PloS one, 2018. **13**(5): p. e0197783.
122. Elliott, J.E., et al., *Structure and swelling of poly (acrylic acid) hydrogels: effect of pH, ionic strength, and dilution on the crosslinked polymer structure.* Polymer, 2004. **45**(5): p. 1503-1510.
123. Hsu, C. and C. Wan, *An innovative process for PEMFC electrodes using the expansion of Nafion film.* Journal of Power Sources, 2003. **115**(2): p. 268-273.
124. Hirsch, A., *Functionalization of single-walled carbon nanotubes.* Angewandte Chemie International Edition, 2002. **41**(11): p. 1853-1859.
125. Elliott, J., et al., *The swelling behaviour of perfluorinated ionomer membranes in ethanol/water mixtures.* Polymer, 2001. **42**(5): p. 2251-2253.

126. Jabbari, E., J. Tavakoli, and A.S. Sarvestani, *Swelling characteristics of acrylic acid polyelectrolyte hydrogel in a dc electric field.* Smart Materials and Structures, 2007. **16**(5): p. 1614.
127. Yeow, J. and J. She, *Carbon nanotube-enhanced capillary condensation for a capacitive humidity sensor.* Nanotechnology, 2006. **17**(21): p. 5441.
128. Lutz, O.H.-M., et al., *Application of head-mounted devices with eye-tracking in virtual reality therapy.* Current Directions in Biomedical Engineering, 2017. **3**(1): p. 53-56.
129. Hickson, S., et al. *Eyemotion: Classifying facial expressions in VR using eye-tracking cameras*. in *2019 IEEE Winter Conference on Applications of Computer Vision (WACV)*. 2019. IEEE.
130. Pettersson, J., et al. *Cognitive ability evaluation using virtual reality and eye tracking*. in *2018 IEEE International Conference on Computational Intelligence and Virtual Environments for Measurement Systems and Applications (CIVEMSA)*. 2018. IEEE.
131. Geiselhart, F., M. Rietzler, and E. Rukzio. *EyeVR: low-cost VR eye-based interaction*. in *Proceedings of the 2016 ACM International Joint Conference on Pervasive and Ubiquitous Computing: Adjunct*. 2016. ACM.
132. Renner, P. and T. Pfeiffer. *Attention guiding techniques using peripheral vision and eye tracking for feedback in augmented-reality-based assistance systems*. in *2017 IEEE Symposium on 3D User Interfaces (3DUI)*. 2017. IEEE.
133. Teiwes, W. and H. Grecu, *Multidimensional eye tracking and position measurement system for diagnosis and treatment of the eye*. 2009, Google Patents.
134. Vargas-Cuentas, N.I., et al. *Diagnosis of autism using an eye tracking system*. in *2016 IEEE Global Humanitarian Technology Conference (GHTC)*. 2016. IEEE.
135. Bartram, S., et al. *Diagnostic post-concussion eye-tracking design*. in *2015 41st Annual Northeast Biomedical Engineering Conference (NEBEC)*. 2015. IEEE.
136. Chen, Z., et al. *Eye-tracking aided digital system for strabismus diagnosis*. in *2015 IEEE International Conference on Systems, Man, and Cybernetics*. 2015. IEEE.
137. Al-Rahayfeh, A. and M. Faezipour, *Eye tracking and head movement detection: A state-of-art survey.* IEEE journal of translational engineering in health and medicine, 2013. **1**: p. 2100212-2100212.
138. Zhang, W., et al., *Gender and gaze gesture recognition for human-computer interaction.* Computer Vision and Image Understanding, 2016. **149**: p. 32-50.
139. Biswas, P. and P. Langdon, *Multimodal intelligent eye-gaze tracking system.* International Journal of Human-Computer Interaction, 2015. **31**(4): p. 277-294.
140. Lee, S., et al., *Ultrathin nanogenerators as self-powered/active skin sensors for tracking eye ball motion.* Advanced Functional Materials, 2014. **24**(8): p. 1163-1168.
141. Braun, A., et al., *Capacitive proximity sensing in smart environments.* Journal of Ambient Intelligence and Smart Environments, 2015. **7**(4): p. 483-510.
142. Sadasivuni, K.K., et al., *Transparent and flexible cellulose nanocrystal/reduced graphene oxide film for proximity sensing.* Small, 2015. **11**(8): p. 994-1002.
143. Nelson, A., et al., *Adaptive and personalized gesture recognition using textile capacitive sensor arrays.* IEEE Transactions on Multi-Scale Computing Systems, 2015. **1**(2): p. 62-75.
144. Moller, C. and F.P. Ribeiro, *Capacitive sensors for determining eye gaze direction*. 2018, Google Patents.
145. Hansen, D.W. and Q. Ji, *In the eye of the beholder: A survey of models for eyes and gaze.* IEEE transactions on pattern analysis and machine intelligence, 2010. **32**(3): p. 478-500.
146. Sarvi, A. and U. Sundararaj, *Electrical permittivity and electrical conductivity of multiwall carbon nanotube-polyaniline (mwcnt-pani) core-shell nanofibers and mwcnt-pani/polystyrene composites.* Macromolecular Materials and Engineering, 2014. **299**(8): p. 1013-1020.

147. Seran, E., et al., *What we can learn from measurements of air electric conductivity in 222Rn-rich atmosphere.* Earth and Space Science, 2017. **4**(2): p. 91-106.
148. Chen, Z. and R.C. Luo, *Design and implementation of capacitive proximity sensor using microelectromechanical systems technology.* IEEE Transactions on Industrial Electronics, 1998. **45**(6): p. 886-894.